A Study of Energy Flow in the Hadronic Final State of Deep Inelastic Neutral Current Scattering Events at HERA

Jonathan Robert Forbes[1]

Department of Physics and Astronomy
The University of Glasgow
Glasgow, Scotland

Thesis submitted for the degree of Doctor of Philosophy

11th October 1993

[1]Supported by a Research Studentship from the Department of Education, Northern Ireland.

ProQuest LLC.
789 East Eisenhower Parkway
P.O. Box 1346
Ann Arbor, MI 48106 – 1346

Abstract

Details of the assembly, wiring and testing of two of the ZEUS transition radiation detectors, TRD1 and TRD2 are presented. Following the installation of the chambers into the ZEUS experiment, the experience gained by the author, problems encountered, suggested design modifications and current status are reviewed.

A study of the behaviour of the hadronic final state in deep inelastic neutral current scattering events at the HERA collider is presented. The study explores the new kinematic regime in Bjorken $10^{-4} < x < 10^{-2}$. For $Q^2 > 10$ GeV^2, various QCD Monte Carlo models are compared to uncorrected and corrected data gathered by the ZEUS Collaboration. The comparison reveals that QCD radiation is an important consideration when predicting final state event characteristics. Both the matrix element approach by itself and the Lund Parton Shower model using a variety of virtuality scales for gluon emission are shown not to reproduce the observed data. The colour dipole model coded in ARIADNE, parton showers matched to matrix elements as performed by LEPTO, and the HERWIG model are shown to give reasonable descriptions of the data.

Preface

The author participated in both hardware and software aspects of the ZEUS experiment investigating *ep* collision physics using the HERA accelerator ring at DESY, the German National Physics Laboratory.

At Glasgow, he worked as part of a small team building, wiring and testing two of the ZEUS transition radiation detectors (TRD) before accompanying them to DESY for installation into the ZEUS detector. While at DESY, he had responsibility for the initial determination of the time offsets t_0 in the Central Tracking Chamber (CTD) during the period of first *ep* collisions.

He participated in the Jets and Hadronic Final States working group where he used the knowledge gained from a study of global event shapes to perform the comparison of ZEUS data with Monte Carlo simulations presented in this thesis.

No part of the work referred to in this thesis has been submitted in support of an application for another degree or qualification of this or any other university or other institute of learning.

Contents

List of Figures

List of Tables

Chapter 1

Introduction

1.1 Overview

High energy physics is the study of the ultimate constituents of matter and the forces which act between them. Work on understanding the structure of matter was greatly advanced in 1911 when Rutherford published his paper [1] on the scattering of α- and β-particles from a fixed target. The results of the experiments could only be described by assuming that incident pointlike α-particles were being scattered by a $\frac{1}{r^2}$ Coulomb force due to a pointlike nucleus. When applied to an electron of energy E incident on a nucleus of charge $\mathcal{Z}e$, the differential cross-section for Rutherford scattering is given by :

$$\frac{d\sigma}{d\Omega} = \frac{\mathcal{Z}^2\alpha^2}{4E^2}\frac{1}{\sin^4\frac{\theta}{2}} \tag{1.1}$$

where α is the electromagnetic coupling constant and $\mathcal{Z}$ is the atom's atomic number.

Further investigation ultimately led to the discovery of the neutron by

Chadwick in 1932. Physicists were now able to describe the constituents of atoms in terms of electrons, protons, neutrons, an electromagnetic force (proposed by Maxwell in 1864) and an unknown 'strong' force which bound the protons and neutrons in a nucleus together. This strong force is now known to be a nuclear manifestation of gluons mediating quark-quark interactions. The current theory describing these interactions is called Quantum Chromodynamics (QCD).

In 1964, Gell-Mann and Zweig had noted that one can imagine the known baryons and mesons to be made up from three species of spin-$\frac{1}{2}$ quarks (q) and antiquarks ($\bar{q}$) if the quarks are allowed to carry non-integral charge. These species, or flavours, were called the u ('up'), the d ('down') and the s ('strange') quark. They postulated that the structure of baryons and mesons is loosely based on bound quark and quark-antiquark pairs :

- *Baryons* $q_1 q_2 q_3$
- *Mesons* $q_1 \bar{q}_2$

To avoid breaking the laws of Fermi-Dirac statistics for the case of the Δ^{++} (uuu), it was postulated by Greenberg that each quark or antiquark possesses one of three 'colours', say red, green or blue, as an extra quantum number. The quarks were seen to follow an $SU(3)_c$ symmetry (c=colour) with flavour symmetry-breaking arising from a mass difference between the s and the (u,d) quarks. Now, it was postulated by Kobayashi and Maskawa to explain the absence of antimatter that in addition to these three quarks, another three flavours (c 'charm', b 'bottom' and t 'top') theoretically complete the quark sector.

In November 1974, bound states of $c\bar{c}$ were discovered at SLAC and Brookhaven [2]. The discovery of the Υ, a bound $b\bar{b}$, state at Fermilab by Lederman et al. in 1977 [3], confirmed the existence of the b. No direct experimental evidence for the top quark has been observed but a mass limit of $m_{top} > 113$ GeV has been estimated by the CDF group at Fermilab [4].

The alignment of six quarks with an $SU(3)_c$ symmetry group alone did not explain all experimental observations. First, in order that quarks and antiquarks

Leptons			
Q/e = -1	e^-	μ^-	τ^-
Q/e = 0	ν_e	ν_μ	ν_τ
L_e	1	0	0
L_μ	0	1	0
L_τ	0	0	1
Antileptons			
Q/e = +1	e^+	μ^+	τ^+
Q/e = 0	$\bar{\nu_e}$	$\bar{\nu_\mu}$	$\bar{\nu_\tau}$
L_e	-1	0	0
L_μ	0	-1	0
L_τ	0	0	-1
Quarks			
Q/e = $+\frac{2}{3}$	u	c	t
Q/e = $-\frac{1}{3}$	d	s	b
Antiquarks			
Q/e = $-\frac{2}{3}$	$\bar{u}$	$\bar{c}$	$\bar{t}$
Q/e = $+\frac{1}{3}$	$\bar{d}$	$\bar{s}$	$\bar{b}$
Generation	First	Second	Third

Table 1.1: *The lepton and quark generations.*

can interact, a mediating vector boson is required. These come from QCD as eight gauge vector fields called *gluons*, each being colour charged but having no electrical charge. These eight mediators cover all the possible interactions between differently coloured quarks and antiquarks and yet allow the gluons to interact with each other, an important difference between QCD and QED. Experimental evidence for gluons came from the discovery of e^+e^- annihilation into three jets ($q\bar{q}g$) at DESY in 1979 [5].

In spite of many searches, there is no experimental evidence to suggest that quarks exist as free particles. It is postulated that this "confinement" of quarks within hadrons is a result of a linear potential, $V(r) \sim \lambda r$, between quarks. Thus, when a quark and antiquark separate their colour interaction stays constant, unlike the electromagnetic force between separating electric charges which decreases with distance. The gluons mediating the interaction between the quark and antiquark attract each other and are condensed into a colour flux

tube with a constant energy density per unit length. The colour lines of force are stretched until they have sufficient energy to create new quark-antiquark pairs. In this way, when quarks separate, hadrons are produced.

Our present knowledge of high energy physics is embodied in a framework called the Standard Model consisting of an electroweak theory based on spontaneously broken $SU(2)_L \times U(1)_Y$ to describe electromagnetic interactions and parity-violating weak interactions, and a QCD theory of strong interactions formatted as an $SU(3)_C$ symmetry.

1.2 The HERA Accelerator

HERA (the **H**adron-**E**lektron-Speicher**R**ing-**A**nlage) is the world's first electron-proton colliding beam accelerator. First *ep* collisions took place on 31st May 1992 [6], with an electron beam of energy 26.7 GeV colliding on a proton beam of energy 820 GeV. The centre of momentum energy at HERA (E_{cms} = 296 GeV) is at least one order of magnitude greater than have been studied in previous fixed target experiments such as NA9 (European Muon Collaboration) at CERN, the New Muon Collaboration also at CERN, and the E665 muon scattering experiment at Fermilab (E_{cms} = 32 GeV) [7]). HERA, shown in figure 1.1, consists of an underground, almost circular tunnel 6.3 km in circumference incorporating two separate magnet rings, one for electrons (or positrons) and one for protons (or deuterons). The rings are made to intersect at four points along the circumference : Halle West, where injection and cooling operations are based, Halle Süd where the ZEUS experiment is situated, Halle Ost which has been used for spin rotator tests and Halle Nord which houses the H1 experiment.

HERA itself is entirely reliant on a series of smaller accelerators, shown in figure 1.2, for its operation. In its present operating condition [8, 9], electrons are generated from an electron gun in the Electron Linac (LINAC II) machine and accelerated to 0.45 GeV. In this machine, the electrons are unbunched. Injection into the PIA accelerator then occurs where the particles are bunched

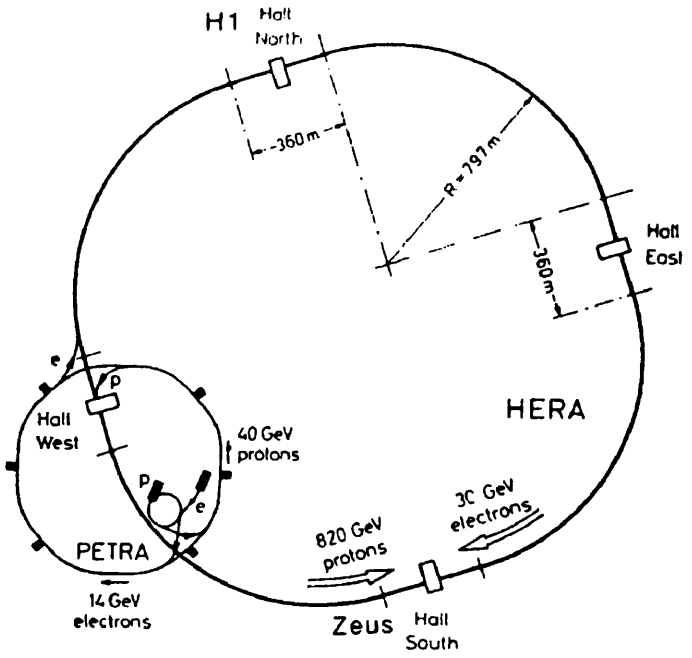

Figure 1.1: *The Hadron Electron Ring Accelerator (HERA) at DESY.*

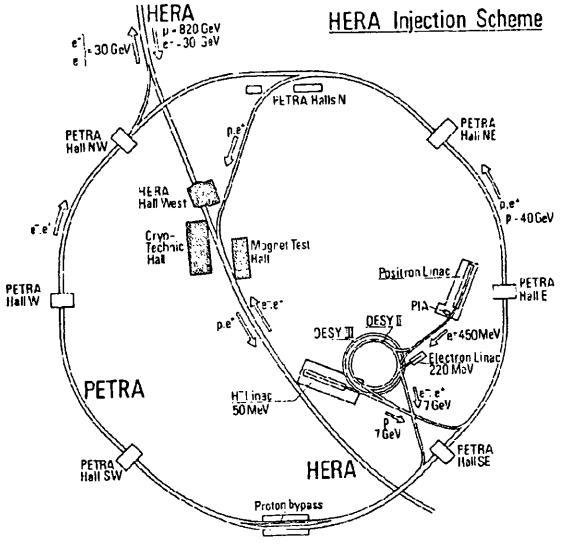

Figure 1.2: *The HERA injector scheme.*

but not accelerated. They are then passed into DESY II (7 GeV) followed by acceleration in the DORIS machine and subsequent transfer to PETRA. From PETRA, electrons enter HERA with an energy of 11.7 GeV and are accelerated to 26.7 GeV before collisions are made.

The proton beam is created within the Positron Linac (LINAC III), an H^- linear accelerator, from where unbunched 50 MeV protons are injected into the recently constructed DESY III ring and further accelerated to 7.5 GeV. Injection into the PETRA proton storage ring is next where a subsequent boost increases the beam energy to 40 GeV. Transfer to the HERA ring and acceleration to the design energy follows. During a physics run, HERA is designed to collide one electron bunch with one proton bunch every 96 ns.

It is important to note that the different energies of the proton and electron beams yield asymmetric final state distributions as in the laboratory frame, the proton momentum in the +z-direction (known as the forward direction) dominates over the corresponding electron momentum. Thus final state particles tend to move forward. ZEUS places a high premium on excellent detection of particles in the forward direction and so has placed three dedicated tracking detectors there with one in the rear. The net result in terms of physics analyses is to minimize the loss of information from particles which continue in the beampipe.

The advantage of constructing a colliding beam machine becomes clear when one considers the energy available for particle creation in the final state. At HERA, the total four-momentum squared available for the final state is equal to about 87000 GeV^2. To achieve the same final state energy in a fixed target experiment would require accelerating an electron to $\approx$ 46 TeV. However, colliding beams do have limitations when compared to fixed target experiments, chief amongst them being the rate at which particle collisions can occur. The interaction rate R can be determined from :

$$R = \sigma L \tag{1.2}$$

where σ is the interaction cross-section and L is the luminosity. In terms of the

more usual machine parameters, luminosity can be written in its most basic form as :

$$L = nf\frac{N_1 N_2}{A} \tag{1.3}$$

where n is the number of particle bunches in either beam, N_1 and N_2 are the number of particles in each bunch, f is the bunch revolution frequency and A is the cross-sectional area of overlap of the beams. There will be additional numeric factors of order unity introduced to account for gaussian beam profiles, for example. In colliding beam machines, beam-beam interactions severely limit the luminosity, so the design value for HERA is $\approx 10^{31}\text{cm}^{-2}\text{s}^{-1}$ compared to $\approx 10^{37}\text{cm}^{-2}\text{s}^{-1}$ from a beam of, say 10^{12} protons from a proton synchrotron incident on 1m long liquid-hydrogen target.

1.3 Kinematics at HERA

It is perhaps worth noting that although experimental methods for studying the constituents of matter have progressed incredibly far in terms of equipment, manpower, interaction rates and particle energies, the same basic technique used by Rutherford to study the nucleus, that of impacting a 'probe' particle onto a 'target' particle and studying the resultant final state, is utilized at HERA to analyse the structure of both the proton and the photon. The situation at HERA is more complicated because the target particle (proton) is now moving.

The mechanism for all HERA interactions is the essentially the same : at the simplest level, incoming electrons and incoming quarks or gluons constrained within the proton can exchange a vector meson. This mediator interacts with both the electron, causing it to change its energy and direction ('scatter'), and with the quark or gluon, which, if the mediator possesses enough energy, causes the proton to disintegrate into its component quarks and gluons ('cascading'). These components are then able to recombine subject to QCD-based rules ('hadronization') to produce the multiplicities of particles which may trigger the detector to enter its data acquisition mode. Each interaction can be described in

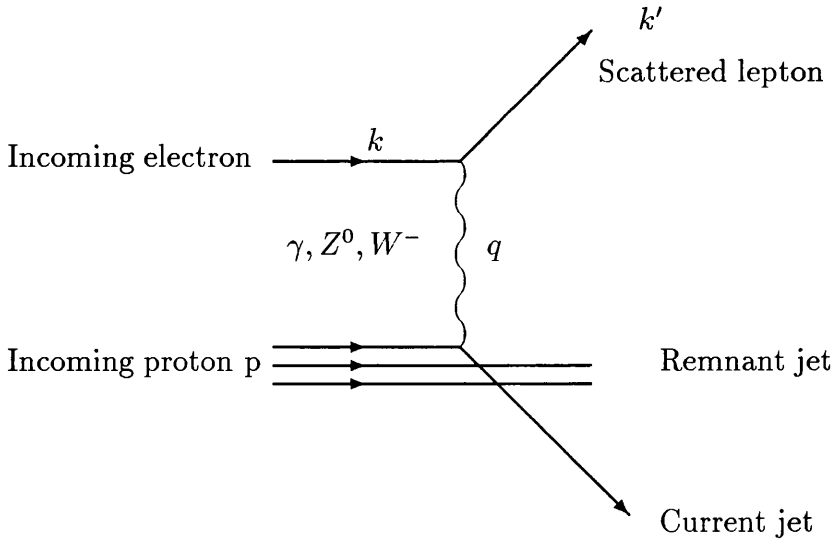

Figure 1.3: *Kinematics of electron-proton interactions.*

terms of a few experimentally measurable quantities which can be combined to yield the kinematic variables of the event.

The kinematics of a parton level ep interaction are defined and illustrated diagrammatically in figure 1.3. A convenient set of energy-momentum 4-vectors (E, p_x, p_y, p_z), can be defined as follows [10]:

$$\text{Incoming electron} \; : \; k = (E_e, 0, 0, -E_e) \tag{1.4}$$

$$\text{Outgoing lepton} \; : \; k' = (E_L, E_L \sin\theta_L, 0, E_L \cos\theta_L) \tag{1.5}$$

$$\text{Incoming proton} \; : \; p = (E_p, 0, 0, E_p) \tag{1.6}$$

$$\text{Exchanged boson} \; : \; q = (k - k')$$

$$= (E_e - E_L, -E_L \sin\theta_L, 0, -E_e - E_L \cos\theta_L) \tag{1.7}$$

Using these definitions, and ignoring electron and proton rest masses (a valid assumption in the HERA energy range), a number of useful quantities can be determined (see table 1.2).

It is more helpful to 'translate' these variables into quantities which depend on experimental observables such as scattered lepton energy and angle, E_L, θ_L and current jet energy and angle, E_j and θ_j. θ_L and θ_j are both measured from

Quantity	Components	Physical Meaning
s	$(p+k)^2$	Total center of momentum energy squared
q^2 $0 \leq Q^2 \leq s$	$(k-k')^2 \equiv -Q^2$	4-momentum transfer squared
W^2 $m_p^2 \leq W^2 \leq s$	$(q+p)^2$	Total mass (centre of momentum energy) squared of the outgoing hadronic system
x $0 \leq x \leq 1$	$Q^2/2p.q$	"Bjorken x" variable. Assume a quark has a fraction x' of the proton's 4-momentum, $p_i = x'p$. Then : $(p_i+q)^2 = p_i^2 + 2p_i.q + q^2$. Assuming that quark masses can be neglected then : $x' \approx Q^2/2p.q = x$
ν	$E_e^* - E_L^*$	Energy loss of the electron in the rest frame of the proton, such that $p.q = m_p(E_e^* - E_L^*)$
y $0 \leq y \leq 1$	$p.q/p.k$	"Inelasticity parameter".

Table 1.2: *Kinematic variables for ep scattering.*

the incoming proton direction such that a non-interacting electron would have $\theta_L = 180°$ (see figure 1.4). This is easily done using the above relations (see table 1.3).

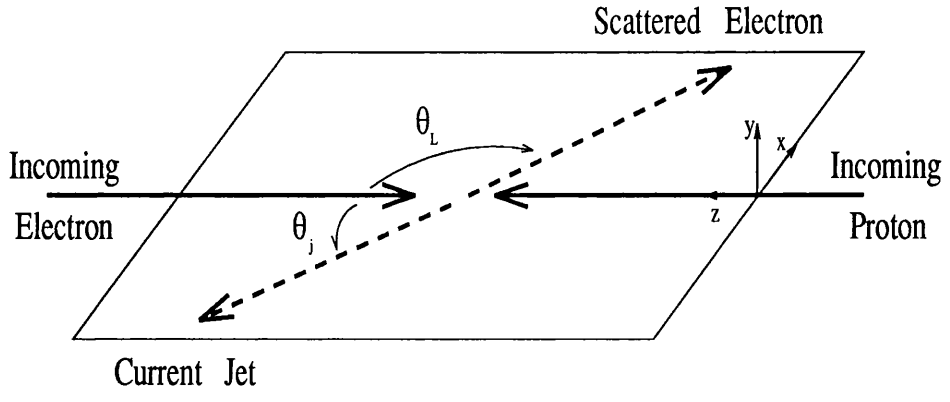

Figure 1.4: *Definition of polar angles.*

Note however, the dependence of these relations on measuring E_L precludes

Quantity	Formula
s	$4E_eE_p$
$q^2 = -Q^2$	$-4E_eE_L(\cos^2\frac{\theta_L}{2})$
W^2	$2E_p(2E_e - E_L(1-\cos\theta_L))$ $-2E_eE_L(1+\cos\theta_L)$
x	$E_L\cos^2(\frac{\theta_L}{2})/E_p(1-(E_L/E_e)\sin^2(\frac{\theta_L}{2}))$
y	$1-(E_L/E_e)\sin^2\frac{\theta_L}{2}$

Table 1.3: *Neutral current kinematics in terms of experimental lepton observables.*

their use in describing charged current interactions in which the outgoing lepton ($\bar{\nu_e}$ for electrons and ν_e for positrons) is not directly measurable. There also exist the following useful relations between the kinematic variables :

- $Q^2 = xys$
- $W^2 = Q^2(\frac{1-x}{x})$
- $Q^2(1-y) = p_t^2$ of scattered lepton

where p_t represents transverse momentum. As has been discussed earlier, the asymmetric energies of the colliding electron and proton beams cause the final state polar angular distribution of particles to be peaked in the forward direction with the result that much hadronic information disappears into the beampipe. This information is lost to the detector and so can distort measurement of the global properties of the hadronic final state. One approach, known as the Jacquet-Blondel method [11], has been developed specifically to reduce the effect of these losses. It uses only those observables due to the final hadronic state and so can also be used to reconstruct (x, y) in charged current events. This is done as follows :

Let P_{had}, a 4-momentum vector, equal the sum of the individual 4-momenta

of *all* outgoing hadrons (both current jet and beampipe particles).

$$P_{had} = \sum_{had} \begin{pmatrix} E_{had} \\ p_{x\ had} \\ p_{y\ had} \\ p_{z\ had} \end{pmatrix} \tag{1.8}$$

so the 4-momentum of the exchanged boson is :

$$q = P_{had} - p = \sum_{had} \begin{pmatrix} E_{had} \\ p_{x\ had} \\ p_{y\ had} \\ p_{z\ had} \end{pmatrix} - \begin{pmatrix} E_p \\ 0 \\ 0 \\ E_p \end{pmatrix} \tag{1.9}$$

Thus :

$$\begin{aligned} p.q &= E_p[(\sum_{had} E_{had}) - E_p] - \\ &\quad E_p[(\sum_{had} p_{z\ had}) - E_p] \end{aligned}$$

and so the y variable can be written as :

$$\begin{aligned} y &= \frac{p.q}{p.k} \\ &= \frac{p.q}{2E_pE_e} \\ &= \frac{1}{2E_e}[(\sum_{had} E_{had}) - (\sum_{had} p_{z\ had})] \\ y_{JB} &= \sum_{had} \frac{E_{had} - p_{z\ had}}{2E_e} \end{aligned} \tag{1.10}$$

The advantages of the Jacquet-Blondel method for calculating y are threefold :

- Forward beampipe hadrons have very little influence on the result because $E_{had} = [(p^2_{x\ had} + p^2_{y\ had}) + p^2_{z\ had}]^{\frac{1}{2}}$ and from equation (1.10), it can be seen that y_{JB} is only affected by the *transverse* momentum components of each hadron, $p_{x\ had}$ and $p_{y\ had}$. Since beampipe particles have limited transverse momenta, they contribute little.

- It is not necessary to distinguish between hadrons from the current jet and the proton jet.
- It assumes nothing about the internal structure of the proton.

In addition to the Jacquet-Blondel method, there exists the Double Angle [12] method which utilizes the scattered electron angle, θ_L and an angle which characterizes the hadronic final state particles, θ_j (also known as γ_h), found from considerations of the longitudinal and transverse momentum components, p_z, and p_x and p_y respectively, of the hadronic system particles. In general :

$$\cos\theta_j = \frac{(\sum p_x)^2 + (\sum p_y)^2 - (\sum(E-p_z))^2}{(\sum p_x)^2 + (\sum p_y)^2 + (\sum(E-p_z))^2} \tag{1.11}$$

To calculate y, Q^2 and x, one can use the relationships [12] :

$$y_{DA} = \frac{\sin\theta_L(1-\cos\theta_j)}{\sin\theta_j + \sin\theta_L - \sin(\theta_L+\theta_j)} \tag{1.12}$$

$$Q^2_{DA} = 4E_e^2 \frac{\sin\theta_L(1+\cos\theta_j)}{\sin\theta_j + \sin\theta_L - \sin(\theta_L+\theta_j)} \tag{1.13}$$

$$x_{DA} = \frac{E_e}{E_p}\frac{\sin\theta_j + \sin\theta_L + \sin(\theta_L+\theta_j)}{\sin\theta_j + \sin\theta_L - \sin(\theta_L+\theta_j)} \tag{1.14}$$

The lack of any energy term other than those of the incoming electron and proton energies in equations (1.12), (1.13) and (1.14) make this method less sensitive to any imperfections in calorimeter energy calibration and dead material effects. For this reason the analysis in chapter 5, which makes extensive use of the ZEUS calorimeters, uses the Double Angle method for x reconstruction.

With its total centre of mass energy currently reaching about 296 GeV, HERA opens up an entirely new range of Q^2 (up by a factor of about 200) and x, now reaching down to about 10^{-4} compared to the fixed target lower value of around 10^{-2}. This is illustrated in figure 1.5 which also shows the siting of the forward, barrel and rear calorimeters in the (x, Q^2) plane.

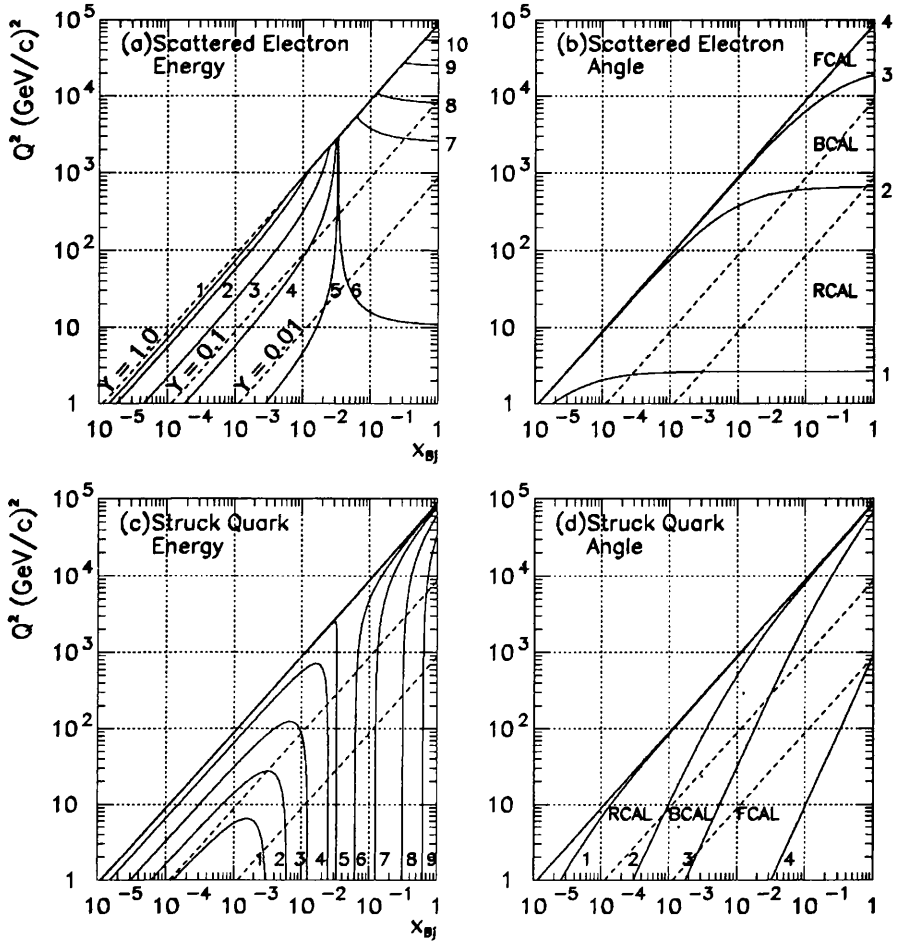

Figure 1.5: *Isolines of energies and angles for the scattered electron and struck quark in the x, Q^2 plane for an incoming electron of energy 26.7 GeV and an incoming proton of energy 820 GeV.*
(a) Scattered electron energy. *The lines correspond to the following energies: 1) 5 GeV, 2) 10 GeV, 3) 20 GeV, 4) 25 GeV, 5) 26.6 GeV, 6) 26.8 GeV, 7) 50 GeV, 8) 100 GeV, 9) 250 GeV, 10) 500 GeV.*
(b) Scattered electron angle. *The lines correspond to the following angles: 1) 176.5^0, rear beam pipe aperture, 2) 128.3^0, RCAL/BCAL boundary, 3) 38.4^0, BCAL/FCAL boundary, 4) 2.2^0, forward beam pipe aperture.*
(c) Struck quark energy. *The lines correspond to the following energies: 1) 2.5 GeV, 2) 5 GeV, 3) 10 GeV, 4) 20 GeV, 5) 26.6 GeV, 6) 50 GeV, 7) 100 GeV, 8) 250 GeV, 9) 500 GeV.*
(d) Struck quark angle. *The lines correspond to the same angles as for the electron.* (FCAL, BCAL, RCAL : Forward, Barrel, Rear Calorimeter).

1.4 Deep Inelastic Scattering

The deep inelastic regime can be thought of as that in which $-q^2$ and $q.p$ are both large but their ratio is not. One of the primary aims of any deep inelastic scattering (DIS) experiment is to measure parton density distributions, sometimes called structure functions . At HERA, these distributions are simply a reflection of the behaviour of the quarks and gluons within the proton when probed by an incident electron via an exchanged boson. Our present knowledge is generally based on phenomenological models tuned to available DIS data and extrapolated into unexplored regions of x and Q^2. For neutral current electromagnetic interactions, there are two distributions, F_1 and F_2, which reflect the electric and magnetic nature of the interaction.

Form Factors and Structure Functions

Investigating the structure of the proton involves comparing a known differential cross-section with one obtained from the required scattering process. For example, a measurement of the angular distribution of elastically scattered electrons from an electric field can be compared to a knowledge of the differential cross-section for the point-like interaction. The difference can be written in terms of a *form factor*, $F(q)$, such that :

$$\frac{d\sigma}{d\Omega} = \left(\frac{d\sigma}{d\Omega}\right)_{point} |F(q)|^2 \tag{1.15}$$

where q is the momentum transferred between the incident electron and the target, $q = (k - k')$. Note however that the form factor need not depend solely on q as will be seen later. To extend this to the study of the internal structure of the proton, a number of points must be considered :

- the proton's electric structure arising from its non-zero size.
- the proton's (and incident electron's) 'magnetic structure
- the proton recoils when struck by an incident electron and if the electron carries sufficient energy, the proton may disintegrate.

These complications can be attended to within the mathematics describing the interaction vertices because the electron-photon vertex is unaffected by the presence of any proton structure. Only the interaction of the exchanged photon with the quark and gluon constituents (collectively termed *partons*) of the proton is unknown. At HERA, the large available Q^2 increases the resolving power of the exchanged photon so enabling the proton structure to be determined with greater detail.

A large number of phenomenologically motivated parton density distributions, based on available low energy data, are available for study. Investigations at HERA will assist to verify their predictions.

The Parton Model and Bjorken Scaling

In 1967, J.D. Bjorken predicted that at very high energies, the Q^2 $(= -q^2)$ dependence of any proton structure function disappears, leaving it as a function of x alone [13], $F_1(x)$ and $F_2(x)$, such that :

$$\nu M W_2(\nu, q^2) \rightarrow F_2(x) = x \sum_i e_i^2 f_i(x) \tag{1.16}$$

$$M W_1(\nu, q^2) \rightarrow F_1(x) = \frac{1}{2x} x \sum_i e_i^2 f_i(x) \tag{1.17}$$

$$\tag{1.18}$$

where e_i is the charge on the parton, $f_i(x)$ is the parton momentum distribution, M is the proton mass, ν is the energy lost by the incident electron after the interaction and $W_{1,2}$ represent the components of the hadronic tensor parametrizing the proton current. Bjorken argued that "scaling" behaviour should be observed and his predictions were verified at SLAC a few years later [14]. Crucial to Bjorken's calculations was the hypothesis that the proton consists of three massless, point-like, non-interacting partons known as valence quarks. Thus at the simplest level, deep inelastic scattering can be described by the interaction of a virtual photon with a single, essentially free quark. This is called the naive quark-parton model (QPM). Comparing the two relations for $F_1(x)$ and $F_2(x)$

yields the Callan-Gross [15] relation :

$$F_2(x) = 2xF_1(x) \tag{1.19}$$

If the proton constituents had spin 0, the ratio of $\frac{2xF_1(x)}{F_2(x)}$ would be zero. As it is, data confirms that the ratio is close to 1, indicative of spin $\frac{1}{2}$ particles.

When one goes beyond the quark-parton model, F_1 and F_2 may no longer scale and they are written with a Q^2 dependence :

$$F_2 = 2xF_1 = \sum_f e_f^2 x[q_f(x,Q^2) + \bar{q}_f(x,Q^2)] \tag{1.20}$$

DIS at HERA

In general, a neutral current DIS event can be written schematically as :

$$l + q \rightarrow l + X$$

where l is a lepton, p is a proton and X represents the final state. The differential cross-section for the neutral current $e^{\pm}q \rightarrow e^{\pm}X$ process (considering single photon exchange only) is described by :

$$\frac{d^2\sigma_\gamma(ep)}{dxdQ^2} = \frac{2\pi\alpha^2}{xQ^4}\left(1 + (1-y^2)\right)F_2(x,Q^2) \tag{1.21}$$

where the Callan-Gross relation has been used to express F_1 in terms of F_2. The $1/Q^4$ term in the expression for the cross-section ensures that the dominant neutral current process will be that for which $Q^2 \rightarrow 0$. Such events are known as photoproduction events and involve the exchange of a quasi-real photon which can interact with a quark or gluon from the incoming proton in many different ways :

1. "Soft" interaction - the Vector Dominance Model (VDM) in which the exchanged photon fluctuates to a bound $q\bar{q}$ state such as a ρ, ω or ϕ. The process is termed "soft" because the Q^2 of the hard scattering process is low, hence the process is not calculable by perturbative methods.

2. Resolved photon interaction - a combination of a larger Q^2 from the hard scattering process and "anomalous" contribution obtained from treating the exchanged photon as an unbound $q\bar{q}$ state. The interaction is calculable because α_s is sufficiently low to warrant treatment by perturbative QCD.

3. Direct photon interaction - the photon interacts as a purely electromagnetic entity. To first order in α_s, these interactions are called QCD-Compton (QCD-C) and Boson-Gluon Fusion (BGF). They are shown diagrammatically in figure 1.6.

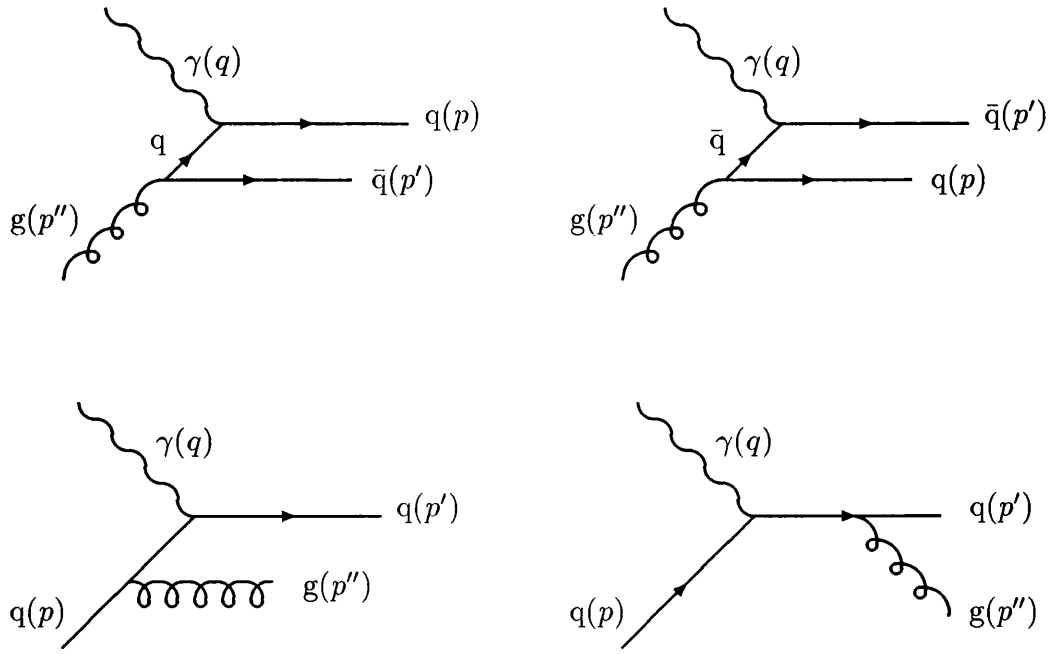

Figure 1.6: $O(\alpha_s)$ *QCD corrections to the basic ep interaction. Clockwise from top left : Photon-Gluon Fusion by* $g\gamma \rightarrow q\bar{q}$*, the crossed diagram, QCD-Compton by final state gluon radiation* $q\gamma \rightarrow qg$*, QCD-Compton by initial state gluon radiation* $q\gamma \rightarrow qg$*. The letters in parentheses beside each particle label signify momenta.*

A resolved photon interaction or VDM process must consider the possibility that the photon has a hadronic structure. Therefore, there is the possibility to

observe the photon remnant in the final state. Data from ZEUS have already been used to study photoproduction events [16] and it has been concluded that significant evidence exists to support the hypothesis of a resolved photon process.

At large Q^2, charged current events dominate over neutral current ones as the propagator is now a massive $W^{\pm}$ boson. Such high Q^2 events will not be considered in this study.

1.5 QCD Simulations

Monte Carlo simulations of physics processes are essential in modern high energy physics analysis [17]. A convenient description of a deep inelastic neutral current scattering event as modelled by Monte Carlo techniques is given in equation (1.22) [18].

$$\sigma_{ep\to lX}(x, Q^2) = D_p \otimes \hat{\sigma} \otimes C \otimes H \tag{1.22}$$

where :

- $\sigma_{ep\to lX}$ is the perturbative hadronic cross-section for the Monte Carlo event sample as a function of x and Q^2.
- D_p is the proton structure function.
- $\hat{\sigma}$ is the hard scattering process as a function of x and Q^2.
- C represents the QCD cascade and models higher order effects.
- H is the hadronization process.

C and H are known collectively as the fragmentation process. In addition, initial state QED radiation from the incoming electron may also be factorised at the appropriate stage.

The hard scatter may consist of the electroweak cross-section with first order QCD calculations which define the kinematics of the initial interaction. The next step, called the QCD cascade, attempts to model the subsequent emission

of softer gluons before and after the boson interaction vertex (called initial and final state QCD radiation respectively). In general, showering in the QCD cascade relies on perturbative QCD and the Altarelli-Parisi (AP) equations [19] to predict parton branching probabilities. The final stage, called hadronization, describes the recombination of emitted gluons and quarks to give colour singlet hadrons. It is an attempt to model the non-perturbative QCD part of the fragmentation process.

1.6 The Matrix Element Approach

The matrix element (ME) approach is an exact, order by order (in α_s) calculation. The lowest order $\gamma q \rightarrow q$ matrix element calculation, known as the Born term and representing the simple quark-parton model, has been available in Monte Carlo models for many years. The next highest order calculations, known as $O(\alpha_s)$ because they involve a single QCD coupling and illustrated diagrammatically in figure 1.6, describe gluon emission $\gamma q \rightarrow qg$ and boson-gluon fusion $\gamma g \rightarrow q\bar{q}$ corrections to the Born term [20].

The matrix elements, which neglect quark masses, are divergent in the limit of vanishing gluon energy or opening angle. These divergences can be partly cancelled by virtual corrections to the Born term graph and partly absorbed in the parton density functions. In Monte Carlo programs, a cutoff must be imposed to prevent these singularities blowing up. For example, in the Lund approach it is required that $m_{ij}^2 > y_{cut} W^2$ where m_{ij} is the minimum invariant mass of any pair of partons in the final state and y_{cut} (the alternative term "y_{min}" is gaining popularity) is a parameter with some theoretical input (the current default value in LEPTO 6.1 is $y_{cut} = 0.015$ below which next-to-leading order QCD calculations become important). The main problem with using a ME approach limited to first order in α_s clearly lies in the removal (by imposing a cutoff) of any soft gluon produced by an $O(\alpha_s)$ process.

1.7 The Lund Parton Shower Approach

The parton shower (PS) model developed by the Lund group [21] relies on the leading log approximation (LLA) to calculate the cross-section for modelling the production of arbitrarily many radiated partons in lepton-hadron interactions. Consider the complete DIS interaction from the hadron side. Before the interaction vertex, called the "initial state", the proton's quasi-real parton constituents are continually branching and recombining. One of these partons may initiate a cascade. The parton may branch to produce two daughters, each of which can initiate its own spacelike or timelike shower. If one of these showering partons has a suitable virtuality, it can be struck by the exchanged virtual boson before recombination takes place and the remaining partons attributed to an initial state shower. The initial state shower is therefore characterized by increasing Q^2, decreasing energies and increasing average opening angles with time.

Now, once the incoming spacelike quark has been struck by the exchanged photon, it enters the "final state" phase, becoming timelike, or at least on mass-shell. If timelike, the quark will start to shower into daughters with decreasing masses. Opening angles between daughters, and their energies also decrease as the shower progresses.

1.7.1 Virtuality Scales

The "virtuality scale" is a term used to describe the phase space available for gluon emission from the quark lines before and after the exchanged photon vertex. In the Lund parton shower approach, any gluon emission from the initial state must necessarily be restricted by a Q^2 virtuality scale since the initial state shower is terminated after a collision with an exchange boson carrying momentum transfer squared Q^2. Since Q^2 sets the scale for the resolution of the proton's constituents, it should govern the parton shower evolution. In the final state shower, a number of scales can be motivated. Those investigated include :

1. Q^2 : for the reasons discussed in the above paragraph. However, this would imply that in the limit $Q^2 \to 0$ (photoproduction), no first order QCD corrections would be present while in fact the process $\gamma + g \to q + \bar{q}$ is still allowed but with a scale customarily related to the transverse mass ($m_\perp = \sqrt{(m^2 + p_t^2)}$) of the produced quarks.

2. W^2 : Although in first order matrix elements, the fundamental parameter is Q^2, Q^2 and W^2 are of similar magnitudes at high x values and widely different at low x values because :

$$W^2 = Q^2 \frac{1-x}{x} \tag{1.23}$$

This x-dependence makes the basic transverse momentum properties of the partons depend on W^2 (the average p_t^2 of jets is found to be asymptotically proportional to W^2 [22]) for not too small x. Thus, it is not unreasonable to say that the W^2 scale could represent an alternative to the Q^2 one provided the x values investigated are reasonably large.

3. $Q^2(1-x)\max(1, \ln\frac{1}{x})$: Apart from Q^2 and W^2 choices, a scale which attempts to model the $\langle p_t^2 \rangle$ behaviour of parton emission as a function of x is included such that the available phase space is given by $Q^2(1-x)\max(1, \ln\frac{1}{x})$. This is an attempt to get round the limitations of the W^2 scale at low values of x and reflects the behaviour of the matrix element calculation. This scale is referred to hereafter as the $Q^2(1-x)$ scale.

1.8 Matrix Elements + Parton Showers

The leading log approximation inherent in the AP evolution equations means that the parton shower approach is good at modelling the soft gluons (those which are collinear with the direction of the parent quark) but not so good at modelling hard, wide-angle partons where the ME model is more successful. Within the LEPTO [23] framework, it is possible to adopt both the matrix element and the

parton shower models in one Monte Carlo generator by matching available phase spaces for each of the two processes to ensure continuity and four-momentum conservation. This matching is known as the ME+PS approach. The process starts with the hard scattering process and is followed by the addition of softer gluon radiation courtesy of the parton shower model. Two different approaches are adopted depending upon whether the hard scatter is a zeroth order or first order QCD process.

1. If the hard scatter is the zeroth order QCD process, the matrix elements give no radiation harder than a cutoff $y_{cut}W^2$. The following parton showers are restricted by the same cutoff and use it as a maximum virtuality scale for the initial and final state radiation.

2. If the hard scatter is a first order QCD Compton or boson-gluon fusion process, then the two final state partons (qg or $q\bar{q}$) define the hardest emission and only softer parton showers can be added. The final state shower then employs a maximum virtuality scale given by the invariant mass squared m_{ij}^2 of the two outgoing partons.

1.9 The Colour Dipole Model

The basic premise of the Colour Dipole Model (CDM) [24] coded in the ARIADNE [25] is that like electromagnetic dipole radiation, which involves the emission of photons from two electric charges linked by electromagnetic lines of force, so partonic cascade formation can be thought of as the emission of a gluon g_1 from two "colour" charges c_1 and c_2 linked by colour lines of force as illustrated diagrammatically in figure 1.7. Subsequent emission of a softer gluon g_2 is treated as coming from one of the two independent dipoles formed between c_1 and g_1, and c_2 and g_1. It is not possible to tell which of these dipoles emitted the gluon as the equations which describe the emission treat the dipole as one complete entity. The method is generalized to cover emission of a third still softer

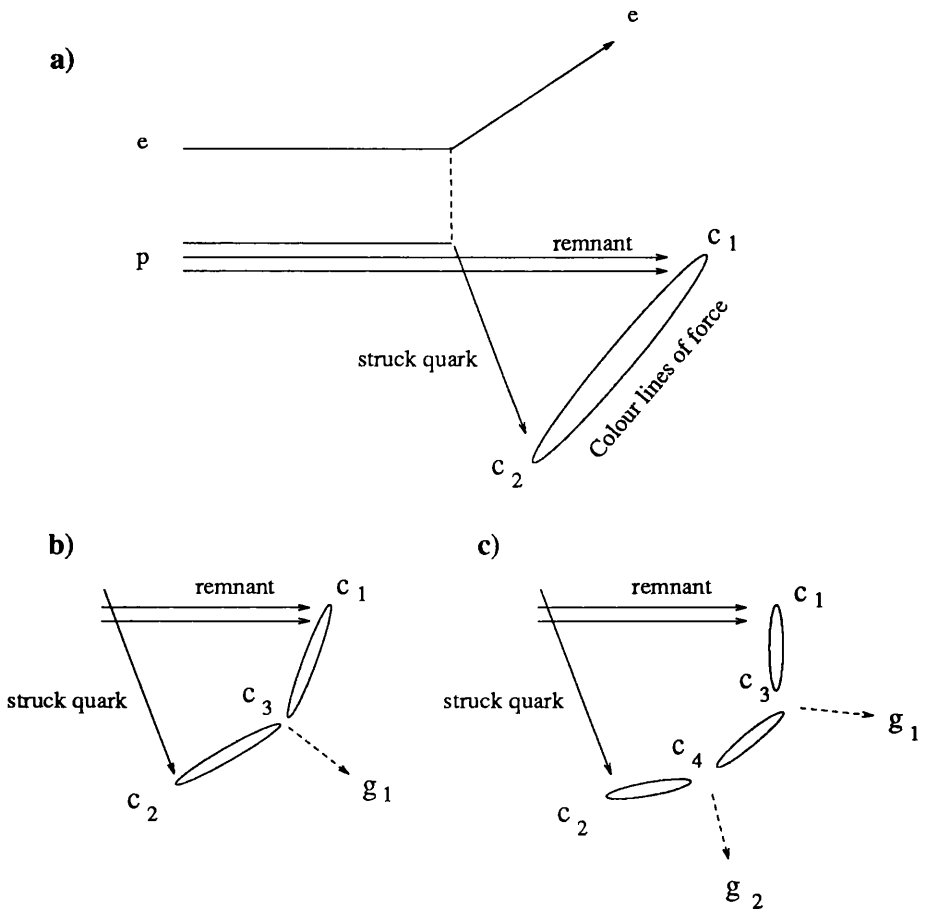

Figure 1.7: *Partonic cascading in the colour dipole model.*
Figure (a) shows the initial colour lines of force between the two colour charges c_1 *and* c_2*. As the cascade progresses, gluons are radiated as shown in figures (b) and (c). Emission continues until the* p_t *of emitted gluons falls below a cutoff.*

gluon from one of the three independent dipoles, and so on and so forth. Emission is stopped by imposing a p_t cutoff, where p_t is the transverse momentum of the emitted gluon with respect to its parent dipole axis.

In this manner, a chain of dipoles is produced such that one gluon links two dipoles and one dipole links two partons. The model corresponds closely to the Lund String approach, where gluons act as transverse excitations (kinks) on a string-like field.

The cross-sections controlling the gluon emission probabilities [26] for a variety of parton-gluon configurations (eg. $qg \rightarrow qgg$ etc.) are divergent in the case of $p_t^2 \rightarrow 0$. A Sudakov form factor [24] removes the divergence forcing the first emission to have the largest p_t. In this way, an ordering is achieved which is not seen in the standard Lund PS approach.

In DIS *ep* collisions, gluon emission occurs from a dipole which initially links the struck quark (pointlike source) and the diquark remnant (extended source) [27]. Following the electromagnetic case, gluons emanate from the extended "antenna" such that the radiation of wavelengths smaller than the extension of the dipole is suppressed. Given a certain transverse size, effectively only a fraction of the antenna proportional to $\lambda(\propto 1/p_t)$ is actually participating in the emission. This is implemented in the colour dipole model so that only a fraction :

$$a(p_T) = \left(\frac{\mu}{p_t}\right)^{\alpha} \tag{1.24}$$

of the proton remnant takes part in the emission, where μ describes the inverse size of the proton remnant and α the dimensionality of the emitter. In the case of the 1-d string modelled in the CDM, $\alpha \approx 1$.

The net effect of treating one end of the dipole as an extended source is that the kinematic range of available phase space for gluon emission becomes restricted to $W^{\frac{4}{3}}$ compared to the standard pointlike-pointlike dipole case. This is illustrated in figure 1.8 which shows the available phase space in terms of a $y - \ln(p_T)$ plane.

The presence of the extended source in DIS studies will help to illuminate

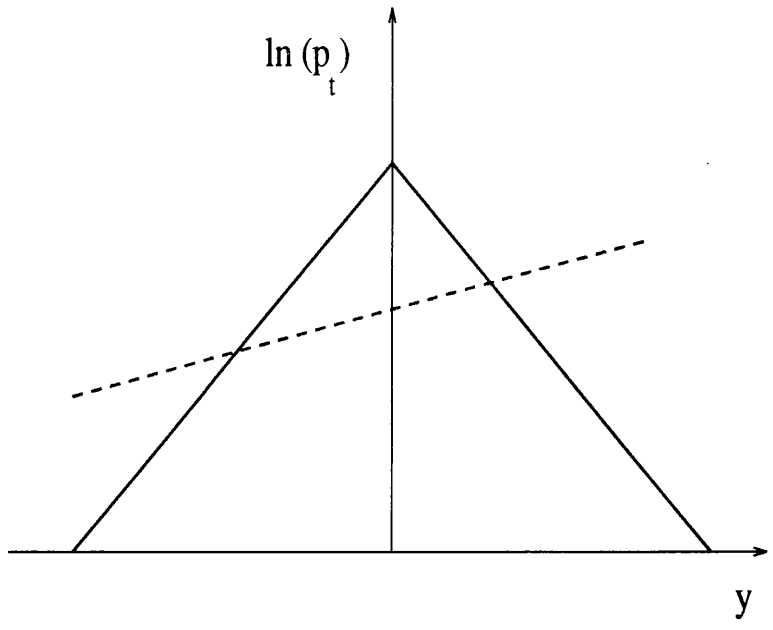

Figure 1.8: *The allowed phase space for gluon emission from an extended source in the Colour Dipole approach to DIS.*
The solid lines represent the case where both dipole emitters are point-like (eg. $q\bar{q}$). The dashed line represents the modification when one end of the dipole is an extended source as in the $q - qq$ final state of ep collisions.

differences in the PS and CDM approaches. This is not the case from e^+e^- studies, where both models give a good description of the data.

1.10 The HERWIG Parton Shower Model

HERWIG [28] is a Monte Carlo event generator for simulating hadron emission reactions with interfering gluons. It uses a parton shower approach for initial and final state gluon QCD radiation including colour coherence effects and azimuthal correlations both within and between jets. HERWIG and Lund use similar methods to model initial state and final state parton showers. In addition, HERWIG employs a sophisticated treatment of azimuthal angular distributions [29, 30]. It differs from the Lund parton shower approach in several ways, some of which are

listed below :

- The characteristic scale of the shower is given by $2E^2(1-\cos\psi)$ where E is the energy of the parton and ψ its angle with respect to its colour connected partner.

- Showering takes place inside a cone of angular size set by the incoming and outgoing struck quark. In the Lund approach, no angular constraints are directly set (but the Q^2 values of the partons on the skeleton leading up from the initiator parton to the hard scatter are strictly ordered, so a form of coherence is present). HERWIG however, takes this further by relating emission angles of subsequent branchings.

- Compared to the Lund approach, HERWIG employs a much higher radiation cutoff (called Q_0^2) in its treatment of initial state and final state showers.

HERWIG does *not* use the Lund string model (coded in JETSET) to hadronize partons, preferring to rely on the cluster model developed by Marchesini and Webber [29, 31] and employing, if desired, a phenomenological "soft underlying event" (SUE) treatment as described in the following section.

1.11 Hadronization

As yet, perturbative QCD studies have not provided any information on the confinement mechanism which, below a certain timelike cutoff, converts emitted partons into hadrons. Perturbative QCD predicts that in hard processes confinement of partons is local in colour and independent of the hard scale Q [32, 33], a "preconfinement" attributable to the use of a Sudakov form factor which inhibits the separation of colour charges forming a singlet state. The preconfinement property is used in a cluster model employed by HERWIG to model the hadronization stage of fragmentation. Partons formed by the

perturbative showering process are split (non-perturbatively) into light (u and d) quark-antiquark or diquark-antidiquark pairs. Colour lines then exist from each quark to an antiquark or diquark with which it can form a colour singlet cluster. The clusters so formed are then fragmented into hadrons, subject to a series of rules. For example, a cluster which is too light to decay into two hadrons is taken as the lightest single hadron of its flavour and its mass is appropriately shifted by momentum exchange with a nearby cluster in the jet. Heavier clusters are first allowed to decay into two lighter clusters or are fragmented using an iterative fission model until the masses of their daughters fall below some threshold.

HERWIG can treat spectator quarks (those remaining after the interaction of a constituent quark with the exchanged virtual photon) by forming beam clusters in one of two ways. By including the soft underlying event, the colour connection between the spectators and initial state parton showers is cut by the forced emission of a soft $q\bar{q}$ pair. The soft hadronic remnant is then represented by a soft collision between the beam cluster and the cluster formed from this emitted $q\bar{q}$ pair. This model is based on a phenomenological description of minimum bias events from the UA5 experiment and produces many soft clusters. The alternative (no SUE) results in the remnant being split into just two clusters.

The Lund group interprets the transition from perturbative to non-perturbative regions in a different fashion. When a quark is knocked out of a proton by a collision with an exchanged photon, the rapid relative motion between the former and the remnant diquark means that a strong colour field will be formed between them. The attractive force between these colour lines (due to gluon exchange) is assumed to confine the field into a narrow flux tube called a string. This string has constant energy density per unit length and gives rise to a long distance linear potential. The string can fission anywhere along its length and the process is assumed to continue until the string fragments are about 1 fm in magnitude, whereupon hadrons are formed. A detailed model based on these ideas of massless relativistic strings has been formulated by the Lund group [34] and coded in the JETSET program [35]. The emission of a hard gluon is handled by introducing a

kink in the string. The fragmentation function $f(z)$ used in the JETSET model is of the form :

$$f(z) \propto z^{-1}(1-z)^{a} \exp\left(-\frac{bm_{\perp}^{2}}{z}\right) \tag{1.25}$$

where z represents the fraction of $E + p_z$ taken by a hadron, out of the available $E+p_z$ and $m_{\perp}^2$ is the mass squared of the hadron's transverse mass. $f(z)$ is called the "Lund symmetric fragmentation function". a and b are two parameters which can be adjusted to help "tune" the Monte Carlo response to available data.

1.12 Radiative Corrections

In several regions, measured x and Q^2 values can be affected by higher order effects such as radiation from quark lines, interference between leptonic and quarkonic radiation, and loop corrections that contribute to the self-energy of the exchanged boson. The dominant process, however, is the radiation of real and virtual photons from the lepton line [36].

The complete first order radiative corrections from the electron and quark line are simulated in the program HERACLES [37]. The program is accurate over all phase space except at very small y and large x where the corrections are large and negative.

1.13 Summary

Before HERA started its physics programme, the Monte Carlo models described earlier gave reasonable agreement with data [38] from lower energy experiments. In the following chapters, the author will undertake an investigation of how well each simulation predicts *ep* collision data in new regions of Bjorken x. A summary of the significant features included in each model and the program versions used in Monte Carlo generation is given in table 1.4.

Data Set	Hard Scatter Gen	QCD Cascade	Hadron Gen	QED Gen	Comment
ME	L61	L61	J73	Yes	Matrix element model.
PS(Q^2)	L61	L61	J73	Yes	Parton shower with Q^2 virtuality scale.
PS(W^2)	L61	L61	J73	Yes	Parton shower with W^2 virtuality scale.
PS ($Q^2(1-x)$)	L61	L61	J73	Yes	Parton shower with $Q^2(1-x)\max(1, \ln\frac{1}{x})$ virtuality scale.
ME+PS	L61	L61	J73	No	Parton shower matched to matrix element model.
CDM	L61	A31	J73	Yes	Colour dipole model.
CDM+BGF	L61	A41	J73	No	Colour dipole model with boson-gluon fusion.
HRW+SUE	H56	H56	H56	No	Parton shower model with multi-cluster remnant fragmentation.
HRW+ NO SUE	H56	H56	H56	No	Parton shower model with bi-cluster remnant fragmentation.

Table 1.4: *A summary of the analysed Monte Carlo data sets and their constituent generators.*
Abbreviations : L61 is LEPTO 6.1; J73 is JETSET 7.3; A41 is ARIADNE 4.1, A31 is ARIADNE 3.1 and H56 is HERWIG 5.6.

Chapter 2

The ZEUS Detector

2.1 Introduction

ZEUS is a large general purpose experiment designed to study particle interactions at HERA. The depth of investigation required from a modern particle physics analysis programme is best realized by designing ZEUS as an interacting system of specialized sub-detectors. These sub-detectors, currently numbering sixteen, are listed in table 2.1. It should be noted that ZEUS employs a right handed coordinate system as shown in figure 1.4, where x axis points towards the centre of the HERA machine.

In order to facilitate particle momenta measurements, a superconducting solenoid is constructed between the CTD and the calorimeter. In the simplest case of a uniform magnetic field, a particle's component of momentum parallel to an applied magnetic field obeys the relation :

$$p_t = qB\rho \tag{2.1}$$

where B is the magnetic field flux density, ρ is the radius of curvature of the particle's trajectory when projected onto the plane perpendicular to the applied magnetic field and q is the particle's charge. Naturally, the finite length of the solenoid and its proximity to iron in the backing calorimeter affects the magnetic field's uniformity and this must be accounted for in reconstruction.

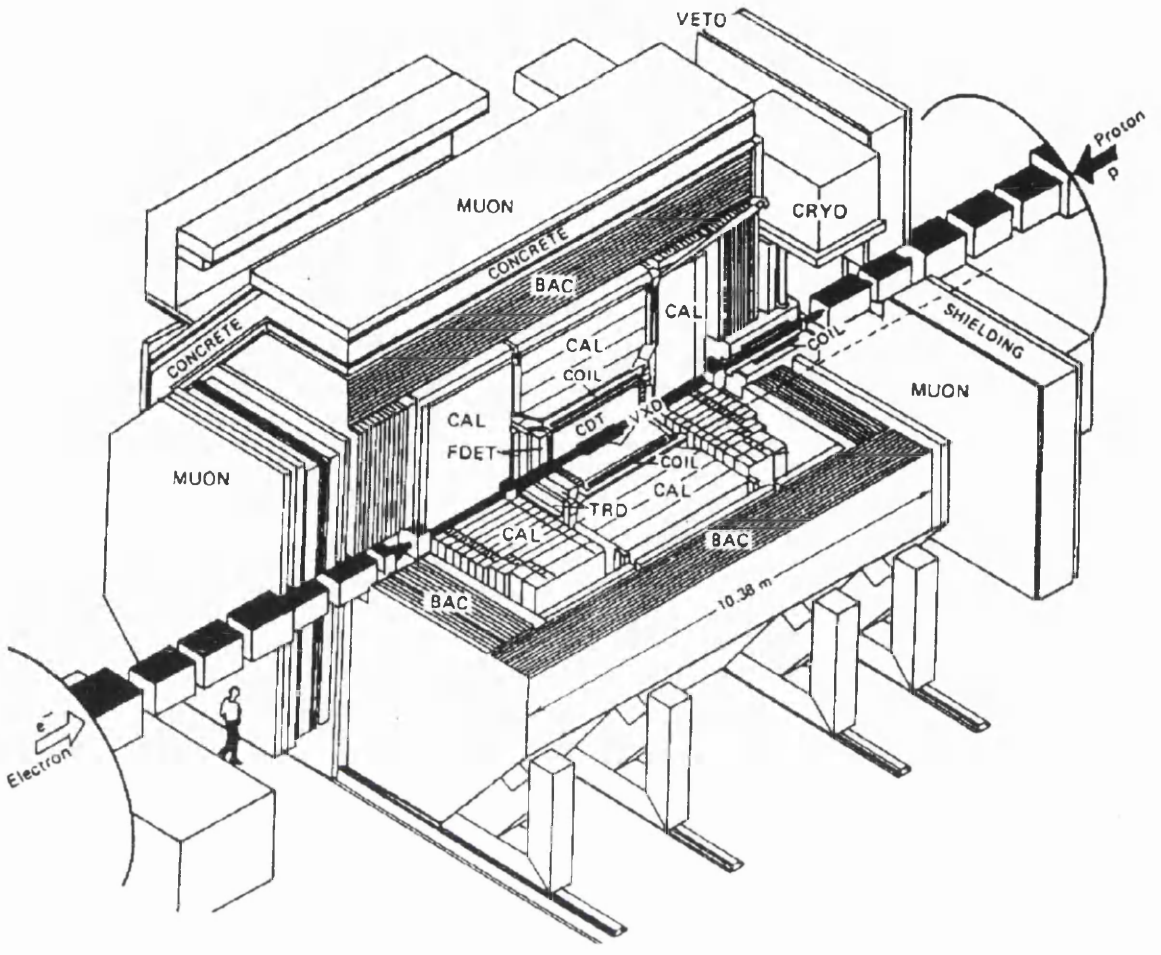

Figure 2.1: *The ZEUS detector.*

The effect of the magnetic field on the passage of colliding beam particles is understandably critical and for this reason, ZEUS was designed to incorporate a small compensating magnet, also of the superconducting solenoid variety, constructed around the beampipe upstream of the interaction point where the protons enter the detector. This compensator magnet is required to provide a field of about 5 T as opposed to the thin solenoid field of about 1.5 T. In addition, an iron yoke is used to provide a return path for the magnetic field lines created by the thin solenoid. The magnetic field in this yoke is utilized to provide additional momenta measurements for high energy muons (heavy, minimum ionizing leptons)

Requirement	Sub-detectors
Tracking	Vertex detector VXD, Central Tracking Detector CTD Forward and rear trackers FTD, RTD
Calorimetry	Forward, barrel and rear calorimeters FCAL, BCAL, RCAL Backing Calorimeter BAC
Muon Detectors	Forward, barrel and rear muon chambers FMUON, BMUON, RMUON
Electron Tagging	Hadron Electron Separator HES Transition Radiation Detector TRD
Luminosity Monitoring	Luminosity Monitor LUMI
Background Monitoring	Background Particle Detector C5 Veto Wall VETO
Target Remnant Detection	Leading Proton Spectrometer LPS

Table 2.1: *The component detectors making up ZEUS.*

and is the basis for the muon detection system in ZEUS.

2.2 Tracking

The purpose of the inner tracking detectors, shown in figure 2.2, is to provide accurate measurements of the positions and momenta of charged particles before they enter the calorimeter. During reconstruction, this information is used to attempt particle tracking and identification. There are four main requirements for the tracking system at ZEUS :-

- Good momentum resolution for high-p_t tracks.
- Electron identification and tagging.
- Accurate tracking as near to the interaction point as possible for vertex determination.
- Input to the event trigger.

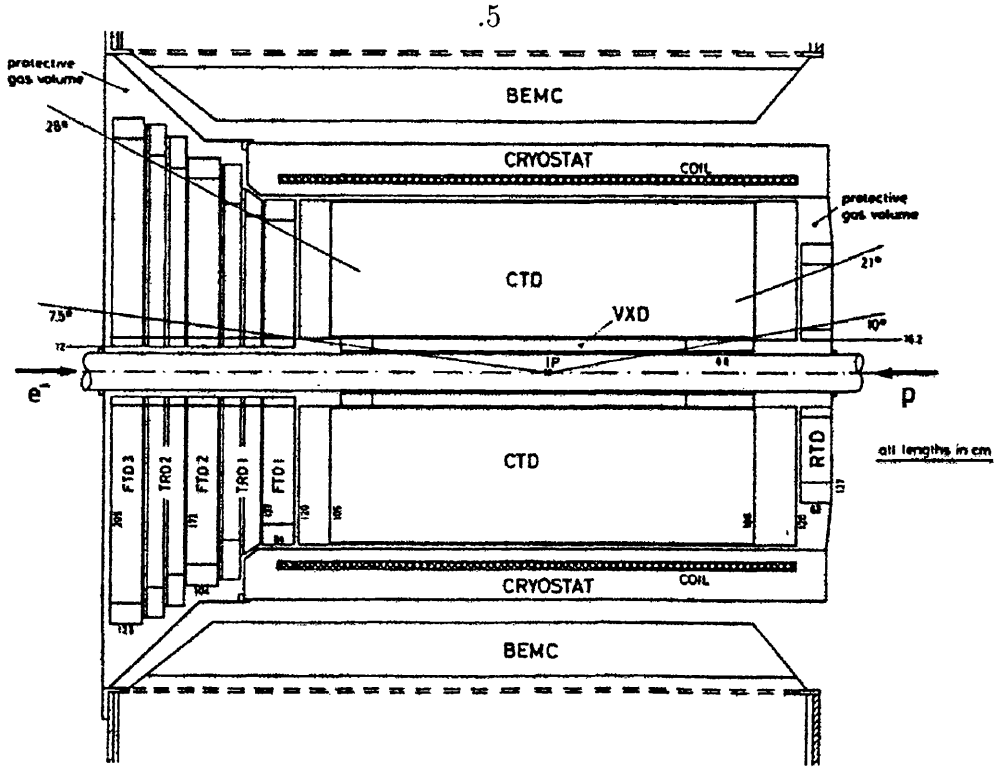

Figure 2.2: *The ZEUS tracking detectors.*

The VXD, situated around the beampipe slightly forward of the interaction point, is a high precision drift chamber using dimethyl ether as the chamber gas. Its purpose is the detection of short-lived particles and improvement of momentum and angular resolution measurements for charged tracks.

The CTD [39] is a cylindrical wire chamber consisting of nine superlayers each with eight sense wire layers grouped into individual drift cells. There are 4608 sense wires and 19584 field wires in total. In five alternate superlayers, sense wires are strung parallel to the beam axis while in the other four, each sense wire is displaced from the beam axis by a small stereo angle of about 5° which aids three-dimensional track reconstruction. Readout is achieved with Z-by-timing (on superlayers 1, 3, 5 only) and FADC systems. Z-by-timing is used to locate the z coordinate of a charged particle by using the difference in arrival times at a wire-end of a pulse created by the particle as it crosses the chamber. It does not

yield pulse-height information and so cannot be used for dE/dx measurements. The FADC system however returns both timing and pulse-height information and has a time resolution of 2.4 ns to the Z system's 48 ns. The chamber gas is an argon/CO_2/ethane 90:8:2 mixture bubbled through ethanol for good gain, drift and noise properties. The CTD is designed to track charged particles in the polar angular region from 15° to 164°. The Summer and Autumn 1992 data used in this analysis were collected with single track resolutions σ_z and $\sigma_{r\phi}$ obtained from Z-by-timing readout only, of 4.0 cm and 1 mm respectively.

Together, the Forward Tracking Detector (FTD) and Transition Radiation Detector (TRD) make up the Zeus Forward Tracker (FDET) which covers the region $7.5° < \theta < 28°$. Designed to improve tracking efficiencies in the high multiplicity forward region, the FTD employs three sets of three planar drift chambers spaced 21 cm apart and oriented at $0^o, +60^o$ and -60^o with respect to the horizontal axis (see figure 2.3). This implies that each FTD chamber can measure three track element projections (u, v, w) and as well as housing the TRD modules, the gap between chambers provides a useful lever arm for track matching. Tracking in the forward chambers is complicated because in this region of the detector, the magnetic field due to the thin solenoid is very inhomogeneous. This requires very accurate mapping of the field and sophisticated software for calculating the space and drift-time relations. The RTD deals with that region in the rear direction not adequately covered by the CTD, namely $159° < \theta < 170°$. Neither RTD, FTD or TRD were used in the Autumn 1992 data taking period.

2.3 Calorimetry

The requirements of a calorimeter are that it be hermetic, provide excellent energy and angular resolutions and offer good hadron/electron discrimination over a large range of energies. To meet these requirements, the ZEUS Collaboration specified a depleted uranium-scintillator calorimeter, shown diagrammatically in figure 2.6.

In a calorimeter, a particle's total energy is degraded in a block of matter

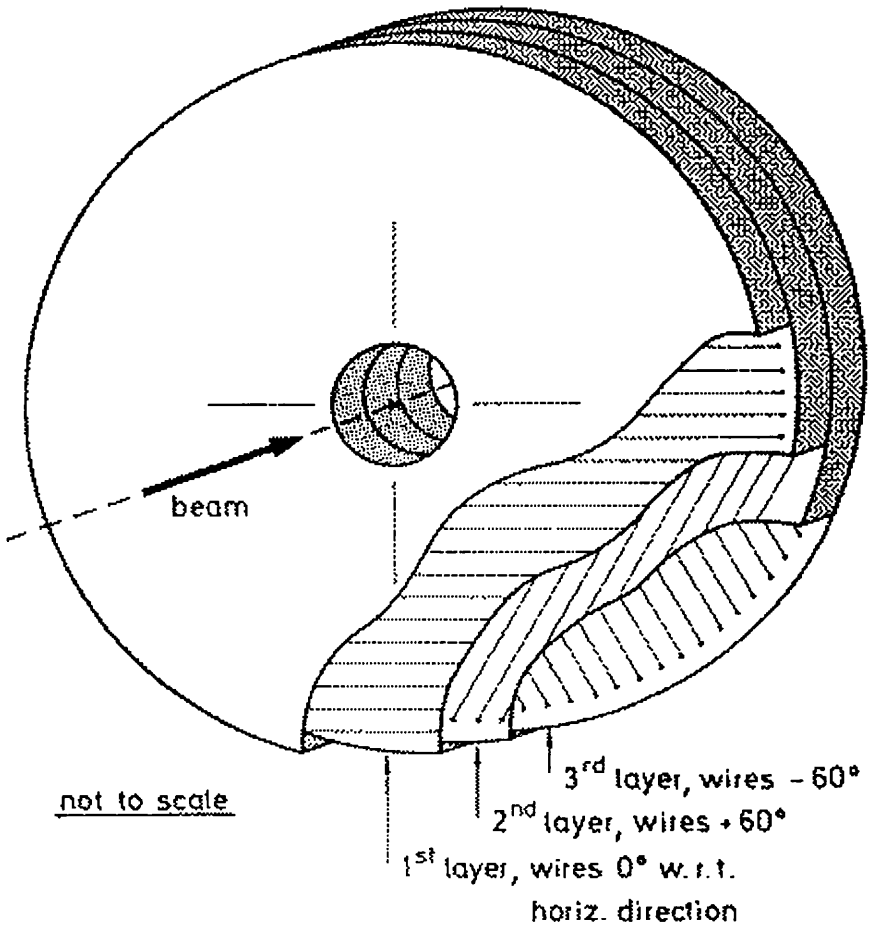

Figure 2.3: *Orientation of the planar drift chambers in one FTD chamber.*

by atomic ionization and excitation. In electromagnetic calorimeters, energy is transported in an electron-photon cascade and transferred to "visible" energy ie. virtually all the incoming energy is recovered by the calorimeter. In a hadronic calorimeter, where energy transport is by a pion-nucleon cascade, only part of the incoming hadronic energy is seen as ionization and excitation because the binding energy in a nucleus is not negligible with respect to particle energies, and some of the produced particles (such as muons, neutrons and neutrinos) can escape the fiducial volume of the calorimeter. The amount of this "invisible" energy fluctuates and can cause large discrepancies in energy measurement. It

is this latter feature which requires treatment by a self-compensating uranium calorimeter because in uranium, part of the invisible energy is compensated for by the detectable products of induced fission - neutrons, prompt photons and decay photons from fission products (see figure 2.4).

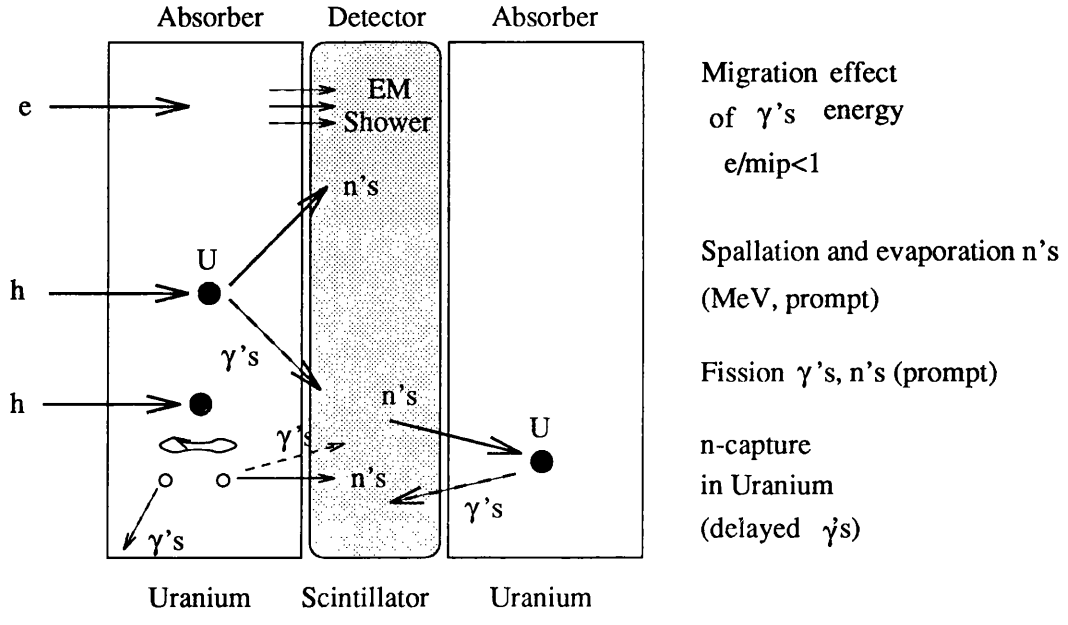

Figure 2.4: *Schematic of the important physics effects involved in self-compensating calorimeters.*

The calorimeter is of the 'sampling' variety meaning it consists of alternate layers of heavy absorber material and lighter signal-producing material. A homogeneous calorimeter, in which the absorbing material also acts as the signal-producer, gives a better electromagnetic energy response for a given volume but does not have enough stopping power to properly measure hadronic shower evolution. The basic sampling unit in the ZEUS calorimeter consists of a 3.3 mm depleted uranium plate (98.4%^{238}U, 1.4%Nb and $\leq$ 0.2%^{235}U) wrapped in 0.2 mm (EMC) or 0.4 mm (HAC) thick stainless steel, and a 2.6 mm thick scintillator plate wrapped in paper, the ratios determined from the data shown in figure 2.5. These ratios, called e/h, represent the signal response for an electron-induced shower compared to a hadron-induced one and are a good measure of the amount

of invisible energy in a hadronic cascade (provided, of course, that all the energy in an electromagnetic shower can be recovered). If e/h is greater than unity then it implies that the hadronic response is smaller than the electron one, whereas if it is smaller than unity, the reverse is true. The steel sheath reduces the

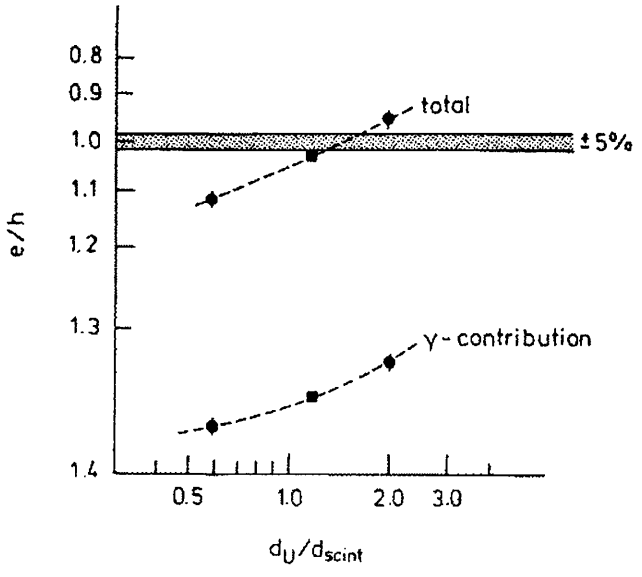

Figure 2.5: *The electron to hadron discrimination ratio e/h as a function of the ratio of uranium to scintillator depths.*

radiation background to a manageable level but allows it to be used to monitor and calibrate the component. Any light produced by the passage of a particle through the scintillator is read out via wavelength shifters to photomultiplier tubes where the light signal is converted into an electrical pulse and processed by the front end electronics. The calorimeter is positioned so as to surround the inner trackers and their thin superconducting solenoid and for convenience of construction and readout is divided into three parts :

- FCAL (Forward Calorimeter) covering the region $2.2^o < \theta < 39.9^o$.
- BCAL (Barrel Calorimeter) covering the region $36.7^o < \theta < 129.2^o$.
- RCAL (Backward Calorimeter) covering the region $128.1^o < \theta < 176.5^o$.

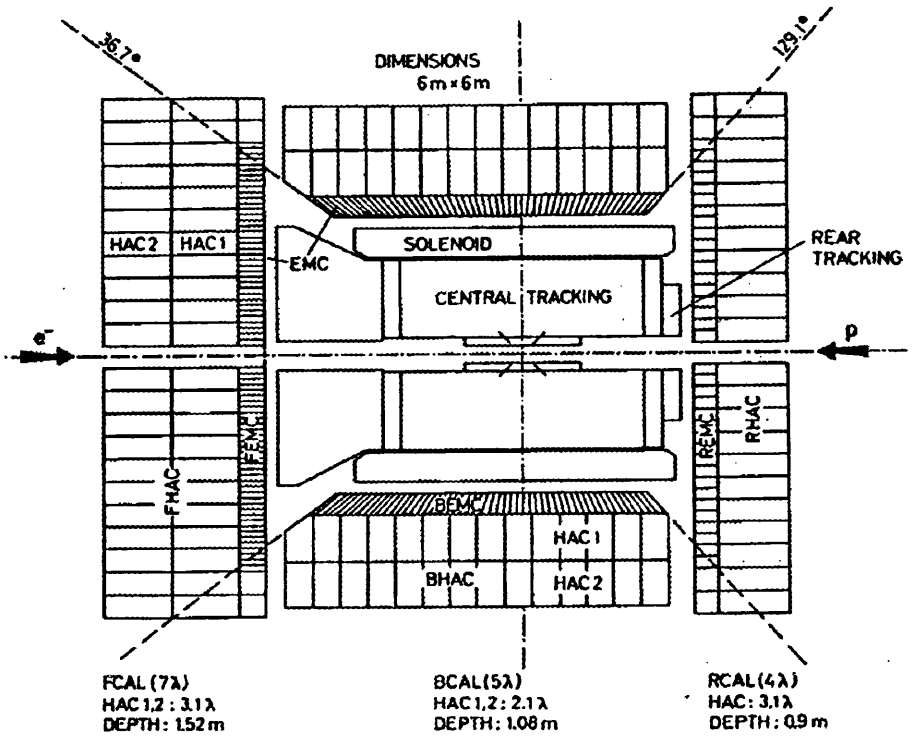

Figure 2.6: *The ZEUS Uranium-Scintillator Calorimeter. Each rectangular subdivision is called a cell. In the FCAL and BCAL, 4 EMC and 2 HAC cells comprise a tower. In the RCAL, a tower is 2 EMC cells and 1 HAC cell.*

Each of the calorimeter units is subdivided into 2 parts. The inner sleeve consists of the electromagnetic calorimeter (EMC) with a depth of about 25 radiation lengths (X_o) or 1 interaction length (λ) for hadrons. The outer sleeve is the hadron calorimeter (HAC) which varies in depth from 6λ in the very forward direction to about 3λ in the rear direction and is subdivided further into HAC1 (inner) and HAC2 (outer) regions in the FCAL and BCAL. Each calorimeter consists of a large number of individually readout 'cells' - a sampling unit linked via wavelength shifter bars to a pair of photomultiplier tubes and thence the readout electronics. Each cell produces an energy and time measurement for every interaction. Calibration of the PMTs allows 1 ns accuracy in tube activation

times and background radiation studies have shown the energy calibration to be steady at the 0.2% level. Combinations of HAC and EMC cells are grouped into 'towers' to aid reconstruction (see figure 2.6).

Test beam measurements give the energy resolution for hadrons to be $\frac{\sigma(E)}{E} = \frac{0.35}{\sqrt{E}} \oplus 0.02$ and for electrons $\frac{\sigma(E)}{E} = \frac{0.18}{\sqrt{E}} \oplus 0.01$ where E is in GeV and $\oplus$ means addition in quadrature. A hermicity of 99.7% of 4π is also achieved, the loss being due to the beampipe holes. The loss is 'asymmetric' as the FCAL is deeper in the z-direction than the RCAL.

Hadron identification and measurement is improved by surrounding the inner fine-grain sampling calorimeter with a backing calorimeter (BAC), consisting of 8 to 11 7.3 cm thick iron plates interleaved with Ar : CO_2-filled aluminium proportional tubes. This calorimeter records information from particles which are formed in, or have punched through, the uranium calorimeter. A hadron energy resolution of $\frac{\sigma_E}{E} \approx \frac{120\%}{\sqrt{E}}$ has been achieved in a test beam setup at CERN [42]. The BAC also serves as a muon trigger device, especially useful in the bottom yoke of ZEUS where no muon chambers are present. By providing three measured points on the trajectory of a muon penetrating the bottom yoke, muon momenta can be estimated.

2.4 Muon Detectors

Muon detection in ZEUS is split into three regions as per the inner calorimeter; a forward, barrel and rear detector (FMUON, BMUON and RMUON respectively). The principle component of each is the Limited Streamer Tube which is supplemented in the FMUON by drift chambers and time-of-flight counters. Additional momentum measurements are achieved in FMUON by use of a toroidally magnetized iron region.

2.5 Separation of Electrons from Hadrons

In order to recognize electrons within hadron jets, for example, to identify the products of charm and bottom semileptonic decay, ZEUS has installed strips of silicon diodes (called "skis") on the electromagnetic sections of the forward, barrel and rear calorimeter. Any minimum ionizing particle traversing the silicon diode then creates electron-hole pairs causing a detectable current. Taken in conjunction with all the other diode responses, it is possible to distinguish the electron shower profile (narrow) from the hadron shower (broader) with reasonable accuracy.

2.6 Luminosity Monitor

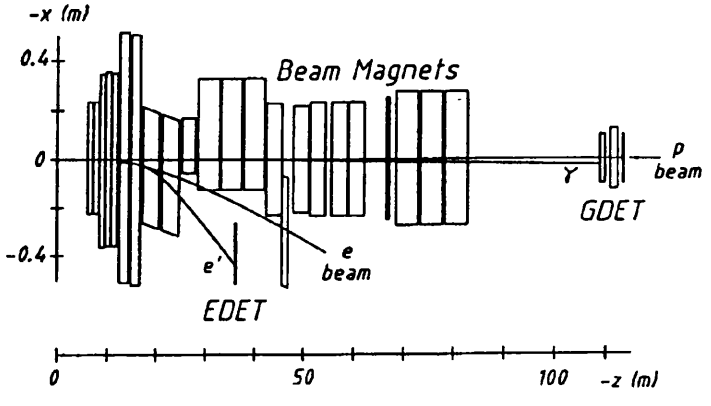

Figure 2.7: *Top view of the ZEUS Luminosity Detector.*

The ZEUS luminosity detector is illustrated in figure 2.7. It shows the placement of the two LUMI branches, both equipped with lead-scintillator electromagnetic calorimeters. Small angle photons ($\theta_\gamma \leq 0.5$ mrad) produced in the electron-proton collision leave the proton beampipe 92.5 m upstream of the interaction point. The photon calorimeter (GDET) is placed 107 m from the centre of the detector in order to detect these photons, protected from the

large flux of synchrotron radiation photons by a carbon filter. Since this filter will certainly cause some photons to pair-produce, an air-filled Čerenkov fills the space between the filter and the calorimeter.

If the scattered electron has an angle $\theta'_e \leq 6$ mrad and an energy $0.2E < E' < 0.9E$, it will be deflected away from the electron beam direction by beam magnets to strike the electron calorimeter (EDET), 34.7 m upstream of the interaction point. ZEUS uses the pilot electron bunch (an electron bunch with no corresponding proton bunch to collide with) to calculate the background to this process from electron-gas particle interactions. If the pilot bunch has a current I_{pilot} and a bremsstrahlung rate R_{pilot} due to these residual gas interactions, and the total measured rate and current are R_{tot} and I_{tot} respectively, then the rate for electron-proton bremsstrahlung (R_{ep}) is given by :

$$R_{ep} = R_{tot} - R_{pilot}\frac{I_{tot}}{I_{pilot}} \tag{2.2}$$

coincidence
Typical rates of 50-100 Hz were obtained in the July 1992 period of data-taking. Using the rate, it is possible to determine the luminosity L if one calculates the cross-section σ_{theor} for the process $ep \rightarrow e\gamma p$ using the Bethe-Heitler formula [43]. The luminosity is then given by (see equation 1.2) :

$$L = \frac{R_{ep}}{\sigma_{theor}} \tag{2.3}$$

As an example, restricting the final state electron energies to the interval 14-19 GeV and the corresponding photon energies to 12-17 GeV then the bremsstrahlung cross-section integrated over the photon energies amounts to about 15 mb. With a rate of between 50-100 Hz, this gives luminosities of the order of $10^{29}\text{cm}^{-2}\text{s}^{-1}$ for the Summer 1992 run.

2.7 Background Monitor

ZEUS employs a set of two scintillation counters (C5) separated by a sheet of lead in the RCAL region of the detector. These serve to monitor the timing and

longitudinal spread of both beams and to detect background events in the region upstream of the interaction point.

The Veto Wall detector (VETO), placed about 7 m upstream from the interaction point, serves mainly to protect the central detectors from particles present in the beam halo of the proton bunches. It consists of an iron wall sandwiched between two scintillator hodoscopes. Beam halo particles are readily absorbed by the iron and the scintillators can provide input to the trigger system.

2.8 The Leading Proton Spectrometer

The asymmetric nature of the beam energies at HERA will tend to boost produced particles into the very forward (small θ) region of ZEUS. The loss of particles down the beampipe is inevitable with colliding beam-type accelerators. ZEUS seeks to minimize the loss of information from each interaction by placing a Leading Proton Spectrometer (LPS) in the very forward region of the detector. Its purpose will be to identify events which contain a 'leading' proton in the target remnant. Such particles are expected to be generated in diffractive processes. Detection of the leading proton will therefore permit more accurate determination of the final state energy in neutral current events and another kinematical constraint on the mass of the undetected anti-neutrino in charged current events.

2.9 The Trigger and Data Acquisition System

A trigger system takes input from a detector's data acquisition system in order to decide whether an event is sufficiently interesting to warrant storage. These characteristics are precoded in programmable trigger elements and this versatility allows any manner of trigger to be set. In addition to the main physics triggers, there are triggers designed for systems and component testing, monitoring and calibration. These can be run in parallel with the main physics triggers. The primary reason for having a trigger is to cut down on the amount of data flowing

from the detector in order that reconstruction and storage can be optimized. To facilitate this, the ZEUS trigger is a three-stage design; first, second and third level (FLT, SLT and TLT respectively). The exceptionally low bunch crossing time designed into the HERA machine (96 ns corresponding to 10 MHz rate) requires the use of *pipelining* to allow time for the FLT to make a decision. In this scheme, the data from each event is digitally stored in one of 52 'bins', each of which is analysed in turn by the FLT, thus providing 52×92 ns ≈ 5 μs for the FLT to calculate its reject/accept flag. The aim of the FLT is to reduce the event rate from 10 MHz (the collision rate) to 1 kHz, the SLT reduces this to 100 Hz and makes the component data available for analysis. At the third level, the whole event can be studied. Application of general criteria for the event can reduce the rate still further to only a few Hz.

The data acquisition (DAQ) stage of a detector concerns itself with collecting the information from all sub-detectors and trigger systems used in the experiment. Among the data acquisition requirements are :

- Readout and recording of data
- Monitoring hardware and software performance
- Control of dataflow

The task of the ZEUS DAQ [44] system is complicated by the high beam-gas background rates (around 100 KHz) observed at HERA as well as the predominant physics process of quasi-real photoproduction which contributes a high rate compared to other 'standard' neutral current event rates. The ZEUS DAQ also needs to cope with $\approx$ 250000 electronic readout channels and a compressed data size of about 120 Kbytes per event. Supervision of the experiment uses a central VAX cluster and about twenty equipment computers to perform such tasks as run control and data quality monitoring. To ease the collection of data, each component has its own individual readout and trigger system right up to the Event Builder which combines and formats the dataflows from each before passing

them to the third level trigger for further analysis [45]. Data, which are stored in tabular ADAMO [46] format, are then shipped across an optical link to the DESY IBM system for storage. Reconstruction and data selection are performed next and the data is then made available for analysis.

2.10 Reconstruction

Various software packages, listed in table 2.2, are available for reconstruction and physics analyses.

Package	Purpose
ZDIS	Interface to available Monte Carlo programs such as Lepto 6.1, Ariadne 4.1, etc.
MOZART	GEANT [48]-based program for full detector simulation
ZGANA	ZEUS trigger Monte Carlo
ZEPHYR	Event reconstruction program
GAZE [49]/LAZE	3-D/2-D Event displays
EAZE	Analysis shell

Table 2.2: *The ZEUS offline analysis packages.*

The ZDIS package serves to convert Monte Carlo generator data from LEPTO, ARIADNE etc. into a standard ZEUS dataflow format. MOZART uses the simple four-vector dataflow provided by the ZDIS package to track and digitize particles through the detector. Hits are added where necessary (for example, to simulate noise or multiple scattering) so extra information is added to the dataflow. It has been shown that the simulation of hadronic showers in GEANT does not describe the ZEUS test data measurements very well [47]. To compensate for this, and with the added bonus of greater speed, the showering routines were adapted to include shower terminators which cutoff the GEANT tracking and showering routines when a particle's energy falls below a certain value. They then distribute its energy in a form which mimics the ZEUS test beam results. ZGANA, the ZEUS trigger simulation, is vital in assisting trigger design, estimating actual

trigger performance and calculating trigger acceptances. ZEPHYR takes as its input either the output of MOZART (and optionally ZGANA) or raw detector data and reconstructs it. This process is divided into three phases :

- Phase One : each detector component module acts on its own detector-specific data to produce local objects. These may be tracks, vertices, clusters of calorimeter cells etc. depending on the detector.
- Phase Two : these independent objects are linked and matched to each other. The information gained can be used to re-evaluate phase one information.
- Phase Three : global reconstruction is attempted. Tracks are matched to clusters in the calorimeter and an interaction vertex is determined.

2.10.1 Track Reconstruction

For the Autumn 1992 run, phase 1 track reconstruction uses CTD and VXD data only. Information from FDET, RTD and muon chambers will be incorporated at a later stage. Standard techniques of seed finding, pattern recognition and track fitting were employed to find tracks. A minimum of four hits in a single superlayer in the CTD is required before track reconstruction was attempted but there is the option of using the VXD as an extra superlayer in the CTD. Phase 2 reconstruction matches tracks over detector boundaries, refitting where appropriate.

An important facet in the effectiveness of track reconstruction is the determination of the time offset, t_0 (t-zero). This represents the time difference between the start of the *ep* interaction and the production of the corresponding pulse in the front end electronics. The intermediate stage involves signal processing, shaping and transmission, all of which introduce noise and time delays. The path travelled by a signal from one 'hit' wire may differ significantly from that travelled by a signal from an adjacent wire. By the time the signals have reached

the front end electronics, they will look different both in shape and time. The idea of a t_0 determination is to try to compensate for the differences in signal propagation time. Without an accurate determination of t_0 for a wire or cell, track reconstruction becomes impossible as the hits attributed to adjacent wires may be far separated in time purely due to travelling through different readout arrangements. Given constant and stable operating conditions, t_0's should be constant for each wire in the chamber.

The author has developed software to allow easy initial calibration of the ZEUS central tracking detector. Originally designed to meet the specifications laid down by the provision of $r\phi$ FADC readout electronics (the same FADC readout cards as the TRD), when this readout system was delayed the author rewrote the code to use the recently installed Z readout system. However, the Z readout system only offers a nominal resolution of 48 ns compared to the 2.4 ns offered by the $r\phi$ system.

The Leading Edge Finder

The principle behind the leading edge finder LEF is recognition of the difference in the bin content when analysing a drift time histogram as in figure 2.8. The software attempts to spot the beginning of the leading edge of the distribution by comparing the contents of two adjacent bins working across from lowest Z timebin to highest to work out the largest jump in the distribution. This is then called the marker bin. When a bin satisfies this criterion, the four bins to the left are summed together. If this sum is less than the sum of the four bins on the right of the marker, the marker is accepted as a candidate for the leading edge. An "end of pulse" marker is also found by a similar method. Thus, the start and end of a pulse are determined and the average height C of the pulse can be calculated. An estimate of "noise" N is obtained from adding up and averaging all the bins to the left of the candidate bin. These values are passed to a fitting function :

$$f(C,t,a,N) = C \times [1.0 + \tanh((t/a) - \tau)] + N \qquad (2.4)$$

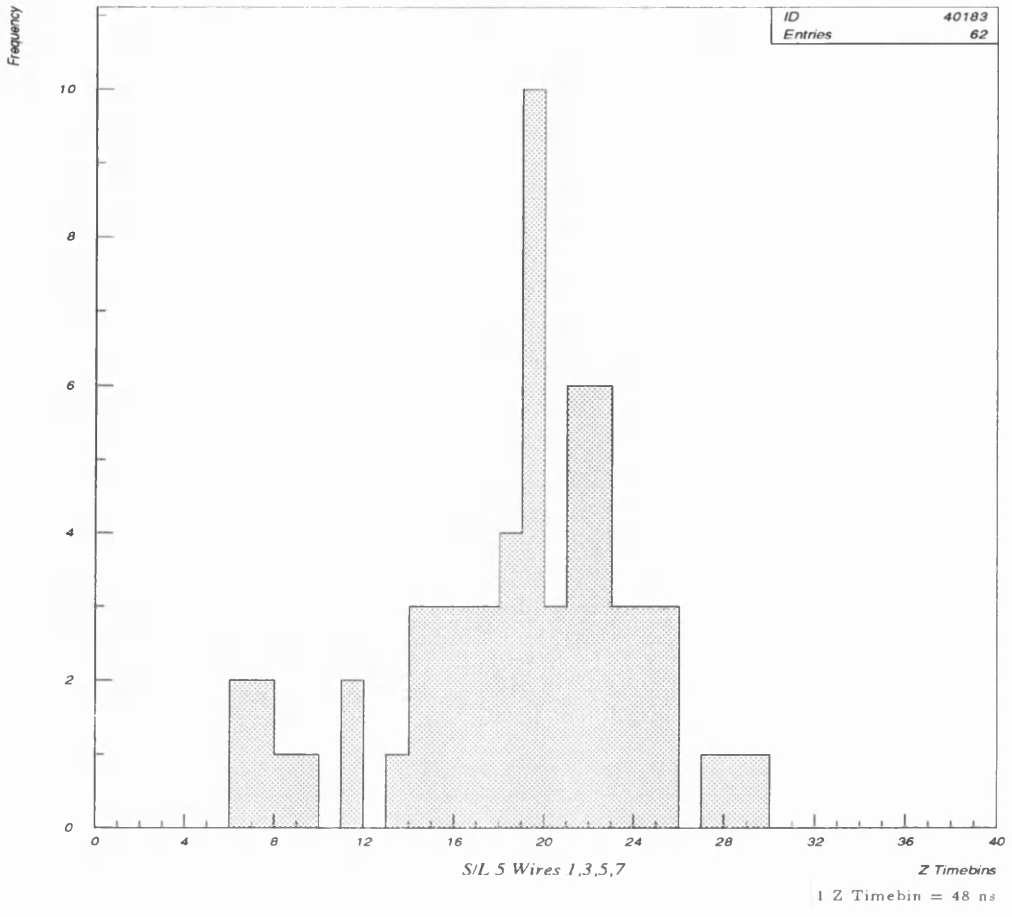

Figure 2.8: *A typical Z readout drift time distribution. Each Z timebin represents a time interval of 48ns.*

a is a 'width' parameter, t is a time and τ is a time offset. a and τ have starting values which are hardwired into the code and are then incremented or decremented as required. This is repeated for all the candidates. The "tanh" function, with different values of N and C for each candidate, is then fitted to the data distributions over the range of the pulse using the CERN package MINUIT which attempts to minimize the χ^2 of the function to the data. When MINUIT has achieved this, the candidate with the best fit to the data is selected (using χ^2 per degree of freedom $\sim$ unity) and the resultant time offset, τ, is redefined as the t_0 for that distribution.

The method has the advantage of speed and reasonable accuracy, but as described below, can suffer from biases in distributions with low statistics where the fitting process is particularly susceptible to ragged pulse plateaus.

As can be seen in figure 2.9, the spread on the comparison of t_0s for data runs separated by 11 days is as much as (16.8 $\pm$ 1.6) ns whereas the expected σ for gaussian errors would be $\frac{48ns}{\sqrt{12}} = 13.9$ ns. The discrepancy is small and thought to be attributable to 'trigger jitter' i.e. timing variations within the first level trigger system but low statistics in event distributions also have a significant effect. The timing differences between superlayers also show up when one studies the mean Δt_0 - it switches from being a negative quantity in superlayer one to being positive in superlayer three and back to negative in superlayer five, although the relative lack of statistics between superlayers one, three and five will contribute.

The author has developed the code to function as a 'black box' to facilitate ease of use by non-experts. To this end, a number of options are available. For example, the user can choose calibration mode - calibrate by wire, cell, superlayer, readout crate or readout card. After execution, four files are created :- one containing the printed output of estimated parameters together with a 'best fit' estimate, one containing a graphical output of distributions for use with the CERN PAW package, one with diagnostic fitting information and lastly, an updated calibration file which can be used directly for track reconstruction. The printed output (below) and the graphical output (figure 2.10) illustrate the end result of the fitting.

```
This file contains fitted edges to data from
              /F1EFOR.R3236.RZ
    and has sent its output to the file
      /F1EFOR.DEV.R3236.ZCARDS.FIT.RZ


 This is card    1
 LEF obtains   1 possible leading edges.
 Each is analyzed below...
```

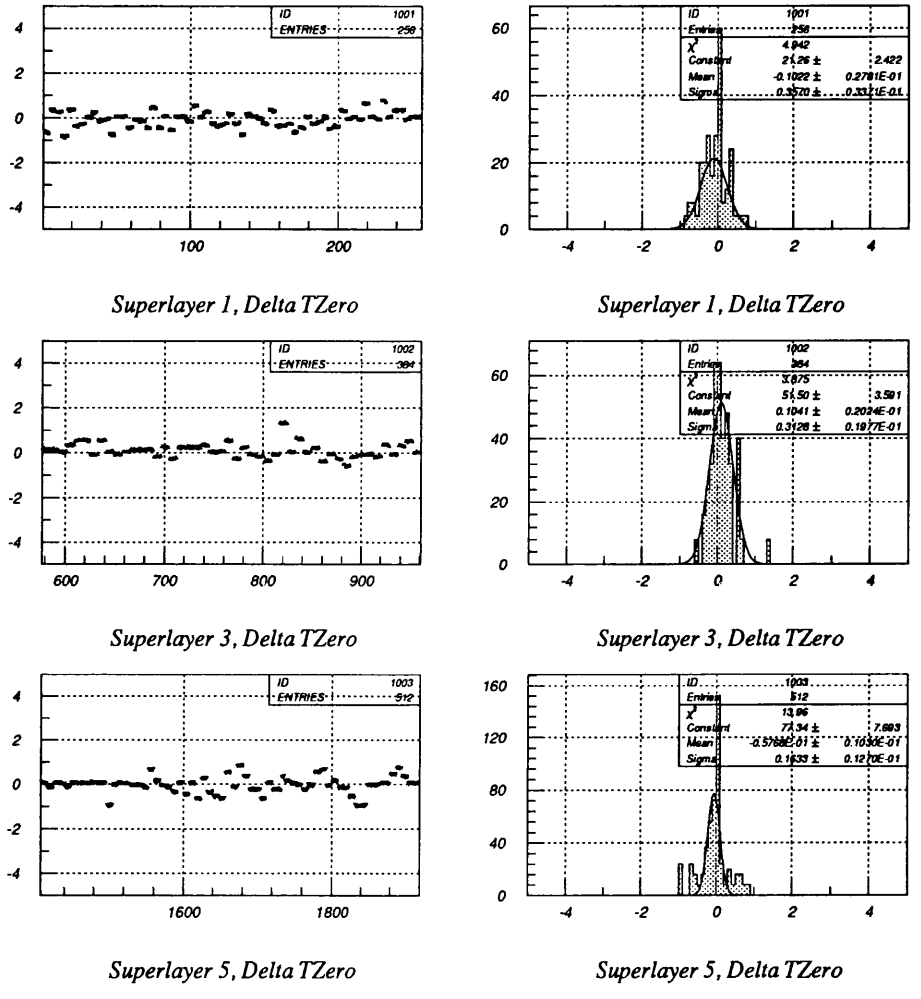

Figure 2.9: *Comparison of t_0 for two separate data runs obtained on 23rd June and 4th July 1992.*

The left hand plots show wire number on the x axis and Δt_0 in Z timebins on the y axis. The right hand plots show a Gaussian fit to the Δt_0 in Z timebins, which are now on the x axis. table 2.2.

Cand	Time	Min?	Const	Width	Noise	T0	T0Err	Fit	F-P%
1	13.0	Yes	9.67	0.05	1.33	13.86	1.06	0.80	0.17

On this Chi2 analysis, LEF selects candidate 1
with a t0 of 13.86 Z Timebins.

This is card 73
LEF obtains 2 possible leading edges.
Each is analyzed below...

Cand	Time	Min?	Const	Width	Noise	T0	T0Err	Fit	F-P%
1	5.0	No	-	-	-	-	-	-	
2	13.0	Yes	2.36	0.00	1.44	13.95	1.39	0.30	23.48

On this Chi2 analysis, LEF selects candidate 2
with a t0 of 13.95 Z Timebins.

This is card 177
LEF obtains 2 possible leading edges.
Each is analyzed below...

Cand	Time	Min?	Const	Width	Noise	T0	T0Err	Fit	F-P%
1	10.0	No	-	-	-	-	-	-	
2	13.0	Yes	1.80	0.01	1.67	13.58	1.08	0.77	0.47

On this Chi2 analysis, LEF selects candidate 2
with a t0 of 13.58 Z Timebins.

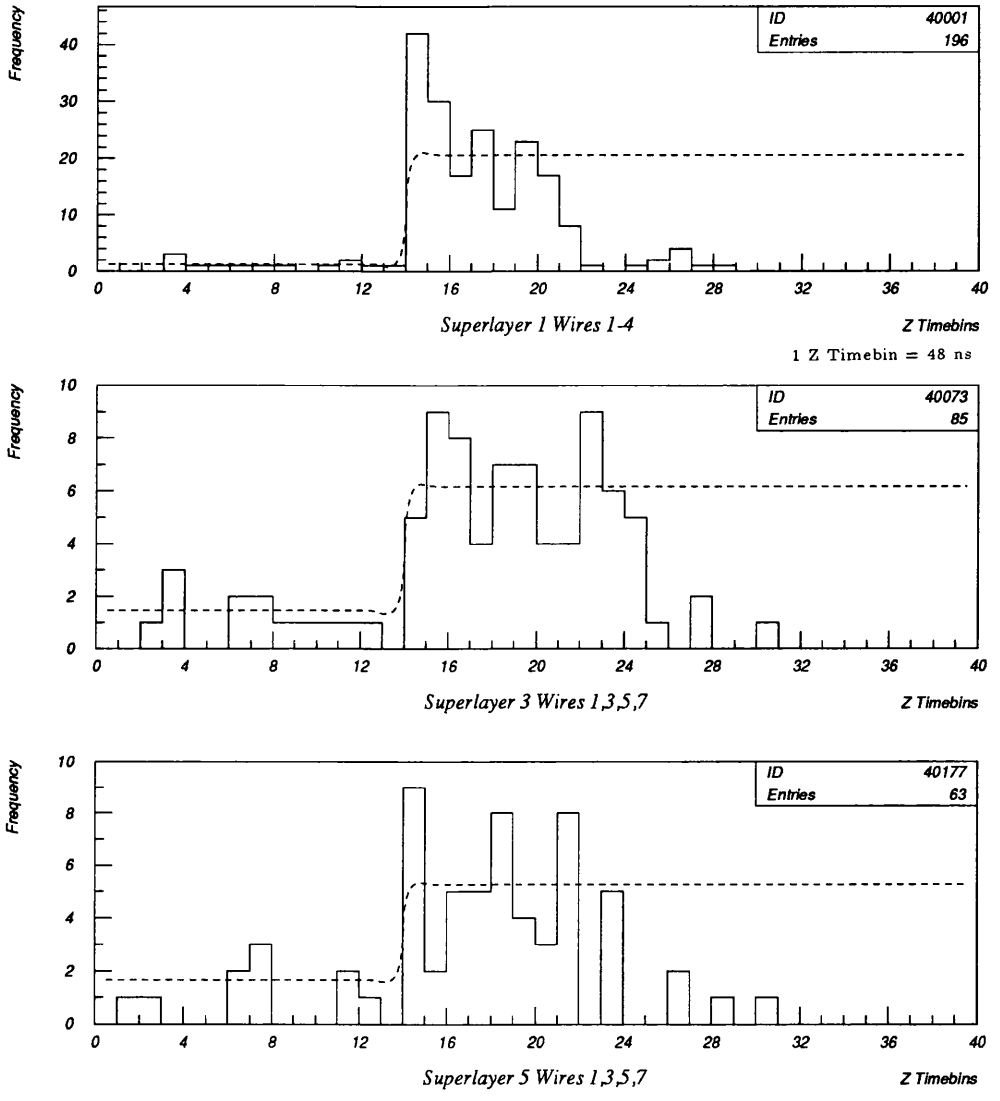

Figure 2.10: *An example of the leading edge fit to three different Z-card drift time distributions (Run 03236).*

The distribution of t_0s for the whole of run 3236 looks is illustrated in figure 2.11. Of the 175 histograms the program was required to fit in this run, it failed in only six cases. Four of the cases were attributable to incorrectly functioning Z-cards (thus the drift time histograms were severly disrupted) and two were genuine software errors where the code failed to differentiate between two individual leading edges.

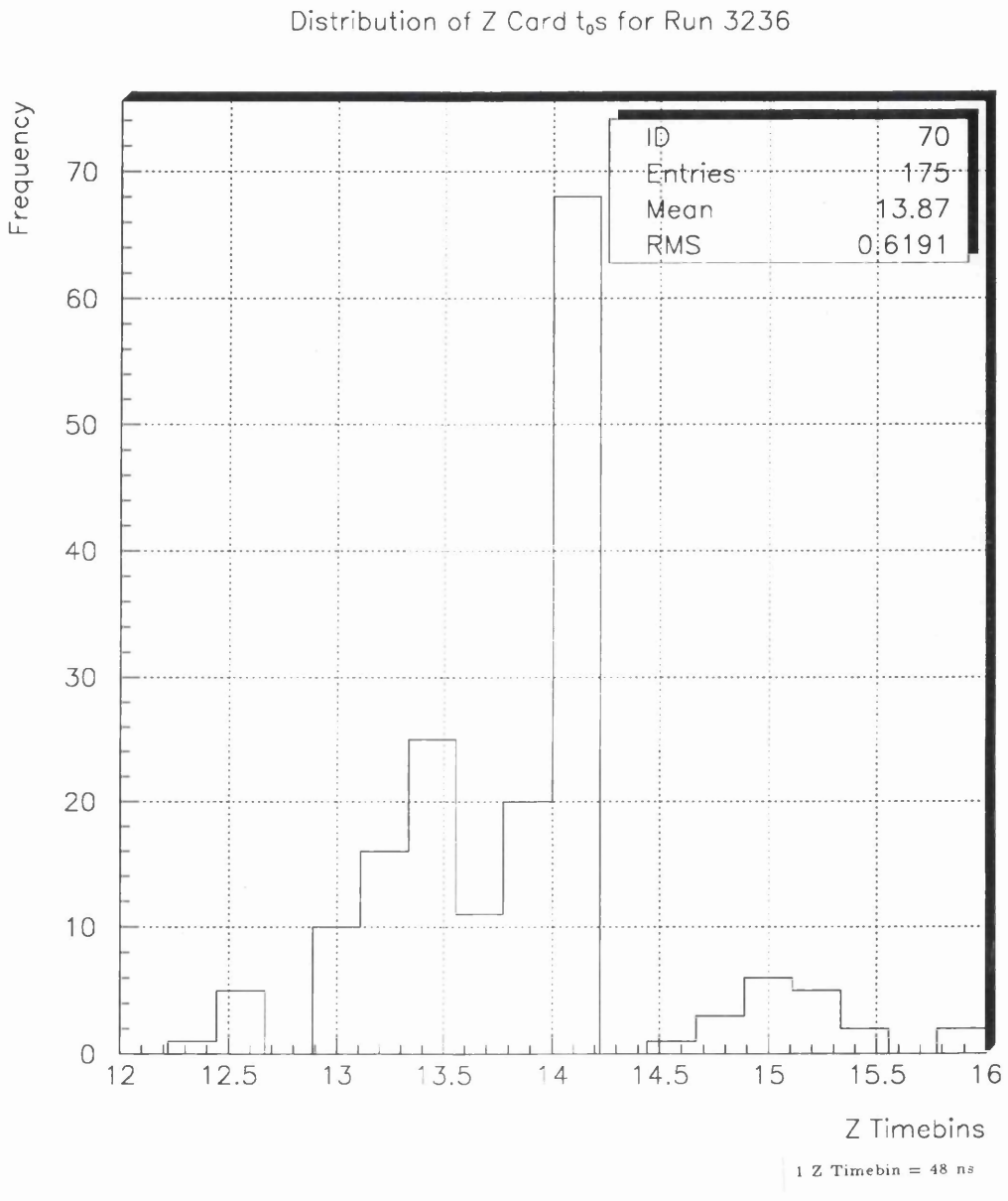

Figure 2.11: *The distribution of t_0s for all instrumented Z-cards in run 03236.*

2.10.2 Calorimeter Reconstruction

As the analysis presented in chapter 5 relies primarily on calorimeter data, it worth looking briefly at how reconstruction takes place in this component.

When the triggers accept an event, all 11836 channels connected to the photomultiplier tubes are read, each producing a time and an energy, and passed to offline mass storage. The code takes this raw digitized information and using calorimeter geometry and calibration data reconstructs the actual event. Phase one reconstruction performs several basic tasks :

- (re)calibration of energies in cells.
- local clustering of cells into condensates
- global clustering into jet-like clusters
- identification of clusters and condensates
- improved reconstruction of identified clusters and condensates
- calculation of calorimeter specific quantities such as energy sums

Calibration is essential for setting cell energy scales, measuring linearity and uniformity of response and monitoring stability with time. Several techniques involving charge injection, laser calibration and uranium noise are available for this task. There are two main sources of background for calorimeter signals - namely, electronic noise and uranium noise (UNO). Electronic noise arises from PMT gains, front end electronics and cable quality while the depleted uranium in the calorimeter also contributes significantly. When tests were carried out involving measuring each calorimeter cell response for an 'empty' crossing consisting of a circulating proton beam only, the average measured noise level for each type of cell was recorded and is shown in table 2.3.

Data used and created by the calorimeter software have a tabular ADAMO format. One such table, called "Caltru", contains the energy measured in

Cell Type	Average measured noise level
FEMC, REMC	18 MeV
BEMC	15 MeV
FHAC	26 MeV
RHAC	25 MeV
BHAC1	28 MeV
BHAC2	32 MeV

Table 2.3: *Cell type and average recorded noise levels.*

individual cells but only if the energy exceeds certain threshold values. The reasons for this are twofold :

- Cells which have no signal but only noise are suppressed.
- The cell table is reduced in size so manipulation and speed of access is improved.

The disadvantages are also twofold :

- If the calibration constants used in the energy calculation are wrong, a cell then has a threshold which deviates from zero. Summing over all cells, this can introduce a bias.
- Applying a cut on cell energies means information about a shower is lost. This has a serious effect on hadronic showers which are broad and extend deep into the calorimeter. The tail of the shower contains many cells which individually have low energies but collectively can add up to a considerable energy.

Investigations into the dependence of accurate reconstruction on cell energy cuts are explored in detail in [50]. Briefly, for typical real DIS events, no applied cell energy cut results in about 6000 cells being included in the reconstruction process. Applying a cut of 0 MeV (to get rid of negative energy cells - an artifact of the calibration process) leaves 3000 cells, while increasing this to 100 MeV on HAC cells and 50 MeV on EMC cells leaves only about 100. The total energy

recorded by summing the cells falls from about 68 GeV to just over 60 GeV as calorimeter noise is removed. This is consistent with a uranium noise signal of about 1 MeV per cell.

The conclusion is that must be drawn is that the standard set of cell energy cuts, shown in table 2.4, are used to reduce the influence of noise in the recorded signal. Eventually, reconstruction must involve corrections to cluster energies to account for the loss of energy due to these cuts.

Cell Type	Energy cut
EMC (Individual EMC PMT)	60 (30) MeV
HAC (Individual HAC PMT)	110 (45) MeV

Table 2.4: *The default cell energy cuts used in this analysis.*

Chapter 3

Transition Radiation and its Detection

3.1 Introduction

The author participated in the construction of two of the four ZEUS transition radiation detectors. This chapter describes the principles behind transition radiation and the experience gained during the assembly, testing and installation of the ZEUS chambers.

3.2 What is Transition Radiation?

Transition radiation (TR) was first predicted by Ginzburg and Frank [51] in 1946 but its possible application for particle identification was not realised until 1975 following suggestions by Artru et al. [52]. This insight arose from the work of Garibyan [53] who showed that the total energy (and number of TR photons) is proportional to the Lorentz factor γ $(= \frac{E}{m})$ of the particle.

TR is emitted when charged particles cross an interface between two media with different dielectric constants. Consider a charged particle moving uniformly and in a straight line in a medium. Electromagnetic radiation will occur under two conditions :

1. $v > v_{ph} = \frac{c}{n(\omega)}$ where v is the particle's velocity, v_{ph} is the phase velocity of light in the medium, c is the velocity of light and n is the refractive index of the medium through which the particle is moving. Čerenkov radiation is the result.

2. The parameter $v/v_{ph} = v \cdot n/c$ changes.

Looking at case 2), it is clear that three options are open for consideration :

- If the absolute magnitude of $\vec{v}$ changes, *bremsstrahlung* results.
- If the direction of $\vec{v}$ changes, *synchrotron radiation* results.
- If n changes, *transition radiation* results.

By forcing a charged particle to cross many boundaries, larger transition radiation intensities can be obtained. A practical method of achieving this is to use many layers of foil each separated by a gas volume, somehow optimized for maximum TR photon production. An alternative method uses a layered fibrous "fleece" immersed in a gas. Such a fleece, consisting of polypropylene fibres of an optimized thickness (described later), is used in the ZEUS TRDs.

This layering of radiators, either foils or fibres, means that TR photons can be produced at each interface. In the optical region ($\epsilon(\omega) > 1$), TR and CR are closely related and are of no special technical interest. In the X-ray ($\epsilon(\omega) < 1$), TR is barely detectable below $\gamma \sim 100$ but increases linearly with γ until limited by the Formation Zone effect (destructive interference due to front/back interfaces). TR thus begins to show its usefulness in particle identification [54].

If we consider the creation of TR photons of frequency ω from a medium with plasma frequency ω_p (see figure 3.1) :

$$\omega_p^2 = \frac{Ne^2}{\epsilon_0 m} \tag{3.1}$$

where N is the number of electrons per unit volume, e is the electronic charge and m the electron mass then, for γ and ω/ω_p are large, the differential flux of

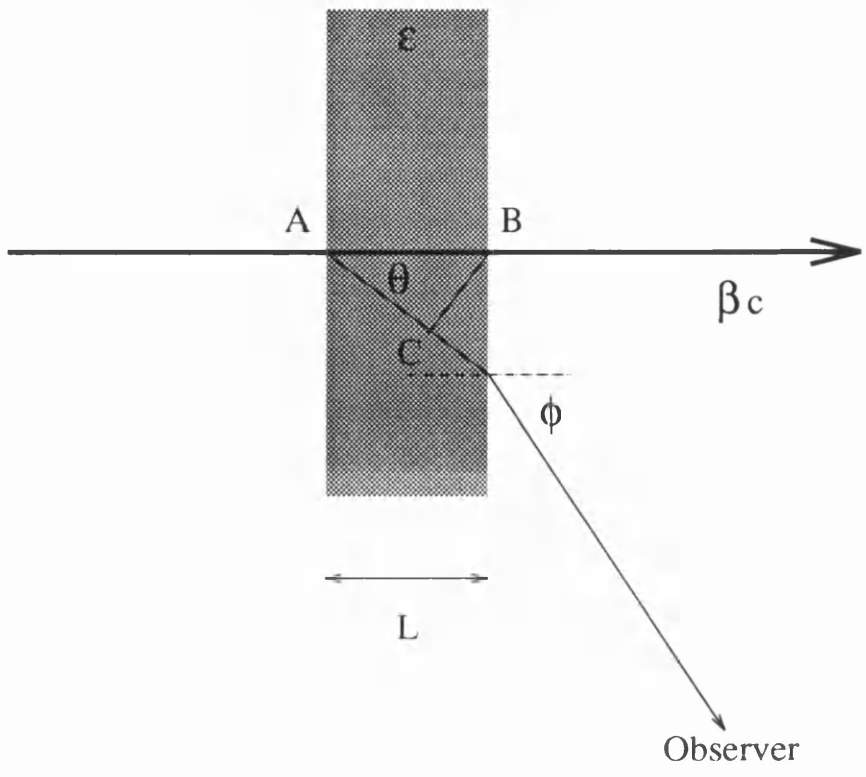

Figure 3.1: *Transition radiation from a single dielectric slab.*

X-ray transition radiation photons from the medium can be written as [55] :

$$\frac{\mathrm{d}^2\nu}{\mathrm{d}\omega\mathrm{d}\Omega} = 4\frac{\mathcal{Z}^2\alpha}{\pi^2\omega}\phi^2\sin^2\left[\frac{\omega L}{4c}\left(\frac{\omega_p^2}{\omega^2}+\phi^2+\frac{1}{\gamma^2}\right)\right]\left[\frac{1}{\frac{\omega_p^2}{\omega^2}+\phi^2+\frac{1}{\gamma^2}}-\frac{1}{\phi^2+\frac{1}{\gamma^2}}\right]^2 \quad (3.2)$$

where L is the thickness of the radiating medium (directly related to the thickness of the fleece or fibres which make it up), $\mathcal{Z}$ is the atomic number of the medium, α is the fine structure constant and c is the speed of light. ϕ is the angle at which the TR photons leave the medium.

Note that the presence of the $\sin^2[\ldots]$ term indicating that the radiation is concentrated into a cone of order $1/\gamma$.

For the ZEUS TRDs with their random interference spacing (they use a fibrous fleece), the interference term can be replaced for low values of γ by its average value ($\frac{1}{2}$) since the term may vary sufficiently rapidly for its effect to be ignored.

Equation (3.2) then reduces to :

$$\frac{\mathrm{d}^2\nu}{\mathrm{d}\omega\mathrm{d}\Omega} = \frac{\mathcal{Z}^2\alpha}{\pi^2\omega}\phi^2\left[\frac{1}{\frac{\omega_p^2}{\omega^2}+\phi^2+\frac{1}{\gamma^2}} - \frac{1}{\phi^2+\frac{1}{\gamma^2}}\right]^2 \tag{3.3}$$

However, at higher γ, the oscillating $\sin^2[\ldots]$ term becomes increasingly important. So far, this approach has ignored the detrimental effect of self-absorption in the radiator fibres. To avoid this, the radiation must have an energy above that of the X-ray absorption K-edge of the medium. This suggests that low $\mathcal{Z}$ materials are best suited for the role of radiator. Beryllium, lithium and polypropylene are used in foils, while Rohacell, Ethafoam and polypropylene are used in fibrous fleeces. However, the mechanical complications involved in supporting many hundreds of radiation foils and electrostatic charge buildup tend to outweigh the increased detection ability of this type of design.

While the radiating materials have a low $\mathcal{Z}$ for good X-ray transparency, the radiator gas must have a high $\mathcal{Z}$ to maximise X-ray absorption and to minimize ionization losses.

3.3 Applications in Detector Design

As already mentioned, material considerations already impose important restrictions on the design of a practical transition radiation detector. If one adds in the requirements of a low drift velocity to maximise recognition and analysis, and a limited detector length, compromises become necessary. Using the above theory, order of magnitude calculations can be performed. For example, assuming a fibrous fleece design, the optimal fibre thickness can be calculated from equation (3.2). Consider the argument A of the interference term :

$$A = \frac{2\pi L}{4\lambda}\left(\frac{\omega_p^2}{\omega^2}+\phi^2+\frac{1}{\gamma^2}\right) \tag{3.4}$$

where λ is a photon wavelength in vacuo. Defining the formation zone Z as :

$$Z = \frac{\lambda}{\pi}\left(\frac{\omega_p^2}{\omega^2}+\phi^2+\frac{1}{\gamma^2}\right)^{-1} \tag{3.5}$$

and stating that for effective TR photon production, the condition :

$$L > Z \tag{3.6}$$

must be satisfied to avoid the limiting formation zone effect. For $\phi \sim \frac{1}{\gamma}$ and significant $\omega \sim \gamma\omega_p$, Z can be written as :

$$Z \sim \frac{\lambda\gamma^2}{3\pi} \tag{3.7}$$

and with a typical X-ray photon wavelength $\lambda \sim \frac{2\pi c}{\gamma\omega_p}$, then for no saturation to occur :

$$L > \frac{\gamma c}{\omega_p} \tag{3.8}$$

Typical values of $\omega_p \sim 3 \times 10^{16}$ Hz and a $\gamma \sim 1000$ for electron identification yield a fibre diameter of the order of μm. The polypropylene fibres in the ZEUS TRD modules are of the order of 20 μm in diameter.

To work out roughly how many TR photons are emitted per interface, it is necessary to go back to equation (3.3). First, one must find the angular distribution of energy flux from a single interface $\mathrm{d}S/\mathrm{d}\phi$ by multiplying by $\hbar\omega$ and integrating with respect to ω :

$$\frac{\mathrm{d}S}{\mathrm{d}\phi} = \frac{\mathcal{Z}^2\alpha\hbar\omega\phi^3}{2}\left(\phi^2 + \frac{1}{\gamma^2}\right)^{-\frac{5}{2}} \tag{3.9}$$

The total flux is then obtained by integrating this equation with respect to ϕ to give :

$$S = \frac{\mathcal{Z}^2\alpha\hbar\omega_p}{3}\gamma \tag{3.10}$$

Thus, for typical photons of energy $\gamma\hbar\omega_p/3$, of the order of $\mathcal{Z}^2\alpha$ TR photons are emitted at a single interface.

3.4 The ZEUS Transition Radiation Detectors

The Glasgow ZEUS group has responsibility for the assembly of two of the four TRD modules which make up the full transition radiation detector. Each module

is a transition radiation detector in its own right and a cluster of four is installed in two groups of two in the ZEUS Forward Tracking Detector for purposes of providing accurate electron identification within multi-hadron jets. Isolation and identification of electron tracks in TRDs are strong for electron momenta above about 2 GeV/c and so the TRDs provide information in the momentum range between ionization-loss and calorimeter measurements. The TRDs also provide a signature which is closely located to the parent particles' track, an essential attribute in a multi-particle environment. The TRD modules all have the same basic shape and layout and are illustrated in figures 3.2 and 3.4.

Internal ZEUS studies using Monte Carlo techniques have highlighted the advantages of using a transition radiation detector over a silicon diode Hadron-Electron Separator (HES) in suppression of hadron identification. A comparison is summarised in table 3.1. Some of the specifications of the TRDs are listed in table 3.2.

Detector Configuration	Electron/Hadron (mis-id)
In Forward CAL, EMC alone	1:2
In Forward CAL, EMC + TRD	1:0.07
In Forward CAL, EMC + HES (one plane)	1:0.25
In Barrel CAL, EMC alone	1:0.6
In Barrel CAL, EMC + TRD	1:0.01
In Barrel CAL, EMC + HES (one plane)	1:0.07

Table 3.1: *Comparison of TRD and HES.*

3.5 Assembly and Testing

Each detector was transported to Glasgow in two "halves" - the cathode plane and the "backplate". As TRD1 and TRD2 are of similar design and differ only in cross-sectional dimensions, a description of the assembly is given in general terms and specific references are made only if required. The basic structure of each TRD is shown in figure 3.3. The cathode plane makes up most of the bulk

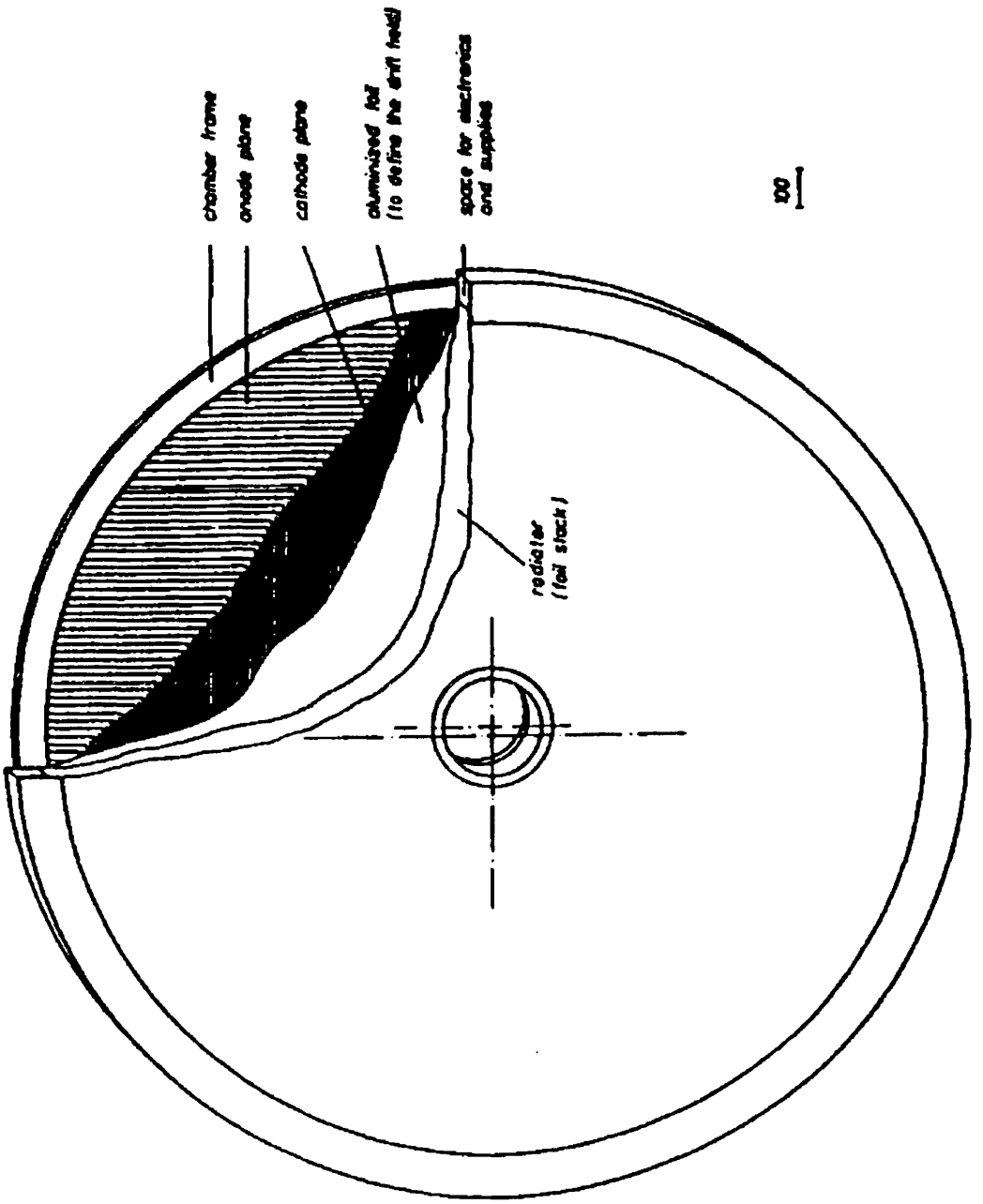

Figure 3.2: *Planar view of TRD.*

The backplate is here marked as the anode plane.

	TRD1	TRD2
Number of wires		
Sense wires	228	244
Potential wires	229	245
Cathode wires	904	968
Dimensions		
Inner chamber radius (mm)	125	125
Outer chamber radius (mm)	825	885
Angular acceptance		
TR detection (mrad)	147-443	137-448
TR detection (deg)	$8.4^o - 25.4^o$	$7.8^o - 25.7^o$
Weight (kg)		
Backplate	17	19
Cathode plane	55	61
Total	72	80

Table 3.2: *Specification of TRD1 and TRD2.*

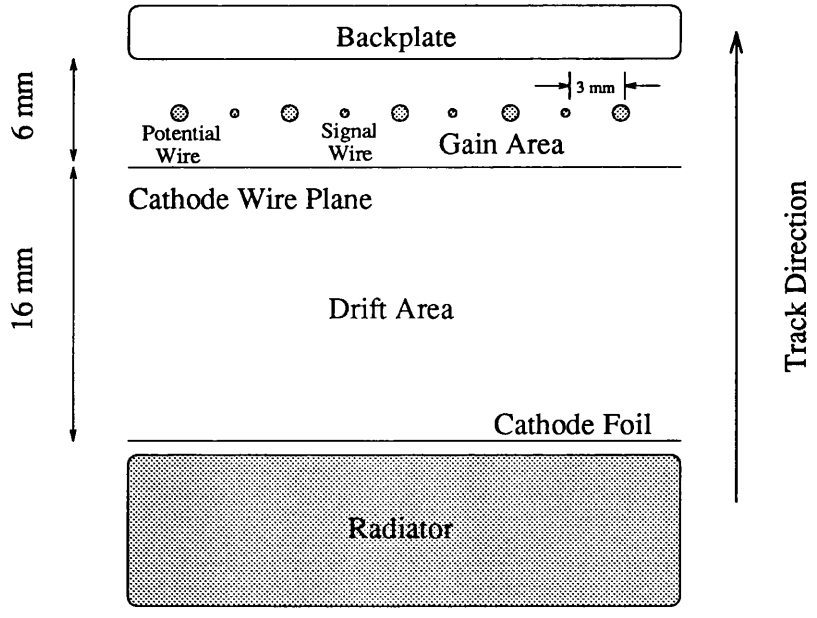

Figure 3.3: *The basic layout of a TRD module.*

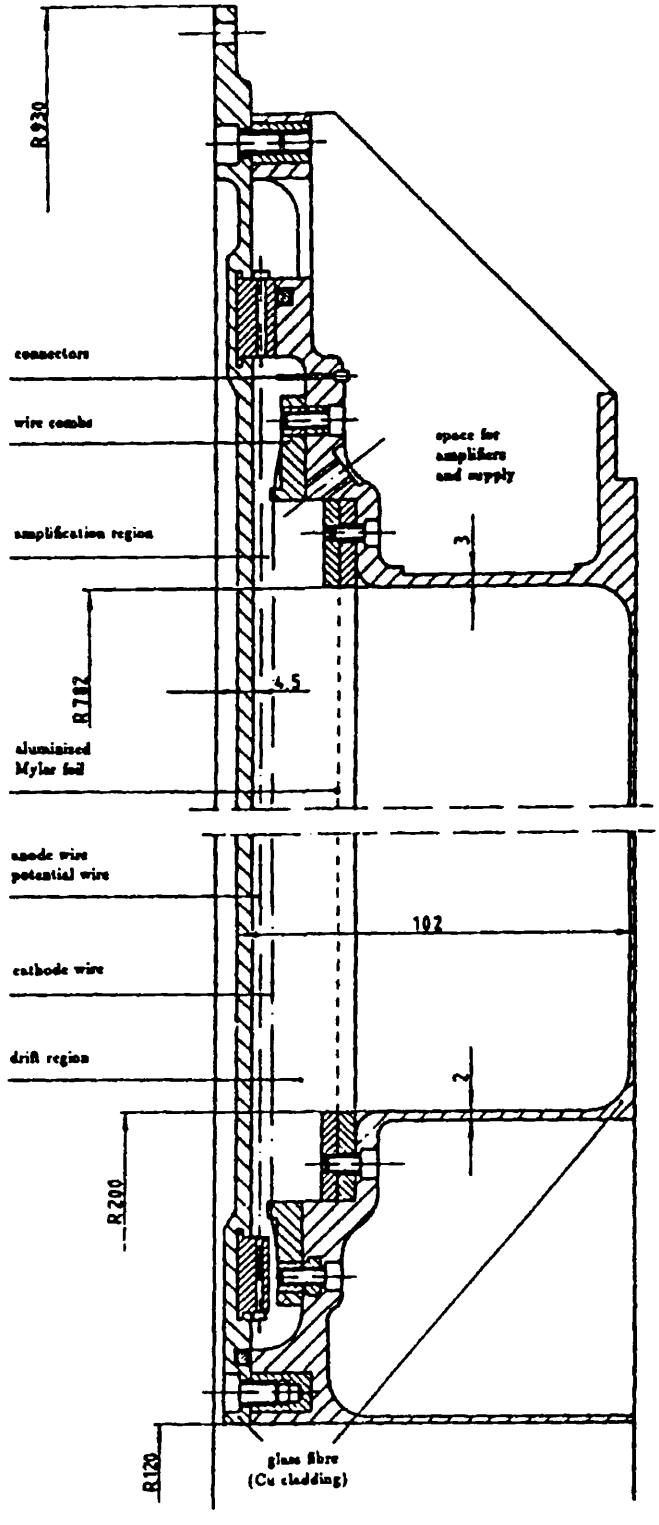

Figure 3.4: *Side view of the top half of a TRD module.*

of the detector module and consisted of a glass-fibre G10 frame containing the polypropylene fibres which make up the radiating "fleece". This fleece is isolated from the drift-chamber gas volume by layer of mylar foil of 6 μm thickness. The completed chamber is mounted vertically with the radiating fleece nearest the interaction vertex.

3.5.1 Cathode Plane Assembly and Testing

This section of work involved completing many small tasks such as mounting of "combs" of the cathode ring and assembly of readout printed circuit boards (pcbs). The most important operations were undoubtedly the wiring of the combs (each comb supports four cathode wires) and their subsequent testing for tension. Wires were strung over a Teflon-coated bar to reduce the effects of friction and then weighted. Weighted nylon line was employed to counter-tension the arrangement and thus eliminate any gross change in wire tension after the frame had been released from the wiring table. The cathode wires must be tensioned to a calculated value to prevent gross electrostatic deflection when a large electric field is set up in the chamber. Such deflections would prove disastrous if they were large enough to permit a short-circuit to the sense or potential wires on the backplate. A short-circuit would give rise to a number of "dead" wires and thus reduce or destroy the tracking ability of the detector. To counter this problem, each wire is expected to hold a tension equivalent to 0.120 kg mass to within an arbitrary $\pm 10\%$. If a wire was over-tensioned by more than $+10\%$, it was passed as low tension wires were considered most likely to cause a short-circuit. These requirements were also applied to backplate sense and potential wires. Tension measurements were obtained electronically by applying a square wave signal to the comb and then inducing oscillations by applying a magnetic field to an individual wire. The most dominant frequency returned by such oscilations was then displayed and recorded. The tension in the wire was then calculated

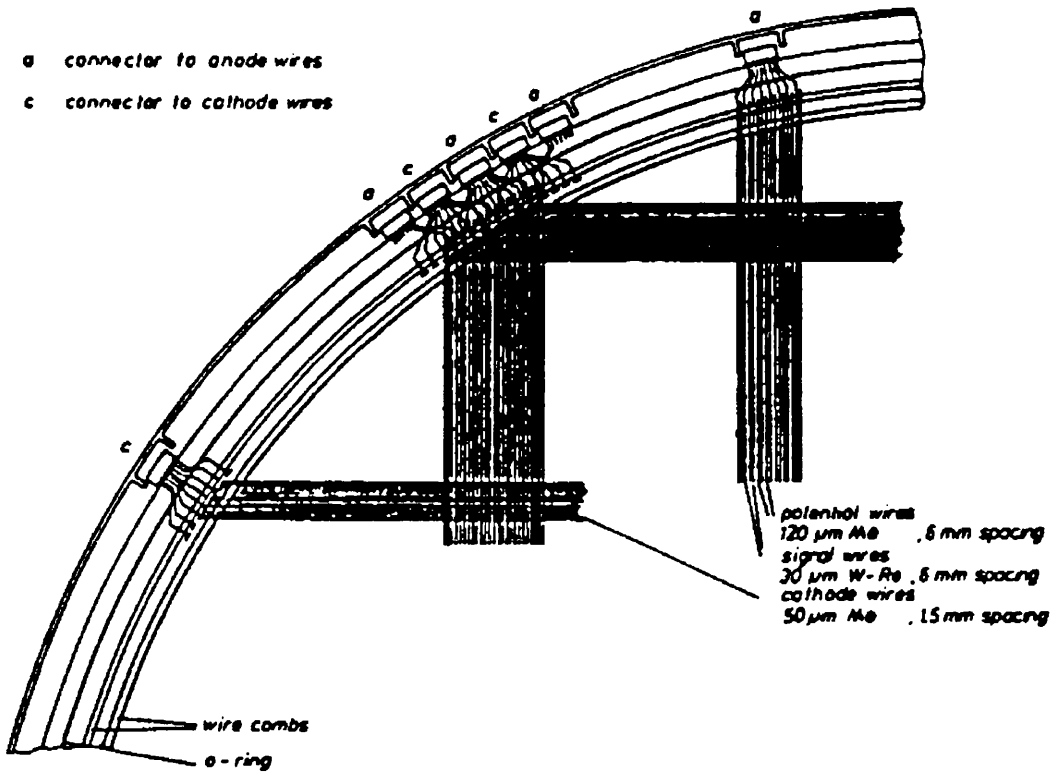

Figure 3.5: *Layout of the cathode, sense and potential wires.*
a and c show the positions of anode and cathode printed circuit boards respectively.

using :

$$T = \frac{4L^2 f^2 \rho}{n^2} \tag{3.11}$$

where T is the tension in newtons, L is the length of the wire in metres, f is the frequency of oscillation in hertz, ρ is the linear density of the wire in kilograms per metre and n is the order of the harmonic. The results for the backplate and the cathode are shown in tables 3.3 and 3.4. Figure 3.5.1 shows the comb/wire numbering scheme used during construction.

All tensions on wires in the cathode plane were checked a number of times and wires were replaced until a satisfactory tension was recorded. Both electrical con-

Wire #/side	Wire type	Date	Measured frequency (in Hz)	Expected frequency (in Hz)	Comment
1 A	Pot	13/6/91	165	164	Passed
1 A	Pot	7/7/91	165		Passed
1 A	Sen	13/6/91	167	168	Passed
1 A	Sen	7/7/91	168		Passed
51 A	Pot	13/6/91	262	264	Failed and replaced
51 A	Pot	7/7/91	435	440	Passed
51 A	Sen	13/6/91	55	94	Failed and replaced
51 A	Sen	7/7/91	97		Passed
114 A	Pot	13/6/91	215	204	High but passed
114 A	Pot	7/7/91	203		Passed
114 A	Sen	13/6/91	210	211	Passed
114 A	Sen	7/7/91	212		Passed
1 B	Pot	15/6/91	164	164	Passed
1 B	Pot	6/7/91	163		Passed
1 B	Sen	15/6/91	160	168	Failed and replaced
1 B	Sen	6/7/91	164		Passed
51 B	Pot	15/6/91	89	88	Passed
51 B	Pot	6/7/91	90		Passed
51 B	Sen	15/6/91	92	91	Passed
51 B	Sen	6/7/91	92		Passed
114 B	Pot	15/6/91	193	204	Failed and replaced
114 B	Pot	6/7/91	208		Passed
114 B	Sen	15/6/91	212	211	Passed
114 B	Sen	6/7/91	213		Passed

Table 3.3: *Specimen TRD1 sense and potential frequency measurements.*

Comb no.	Wire no.	Date	Measured frequency (in Hz)	Expected frequency (in Hz)	Comment
1 A	1	8/7/91	263	249	Passed
	2		268		Passed
	3		259		Passed
	4		259		Passed
1 B	1	8/7/91	254	249	Passed
	2		262		Passed
	3		254		Passed
	4		262		Passed
26 A	1	8/7/91	89	90	Passed
	2		89		Passed
	3		90		Passed
	4		89		Passed
26 B	1	19/6/91	90	90	Passed
	2		89		Passed
	3		90		Passed
	4		90		Passed

Table 3.4: *Specimen TRD1 cathode wire frequency measurements.*

tinuity along a comb and electrical isolation from adjacent combs were checked. Electrical resistances were also recorded. Tests performed during the wiring of the chamber led us to believe that wires on either side of the beampipe (comb numbers 26 through to approximately 50) are most vulnerable to losing tension. This is probably attributable to their greater length. However, after monitoring the situation over a number of weeks the tensions were deemed satisfactory. At this point, the cathode wire readout printed circuit boards (pcbs) were glued in place and the chamber was thoroughly cleaned and prepared for close-up.

Investigations performed after wiring showed that no measurable distortion of the chamber frame had occured. However, two remarks should be made. First, a small gap in the cathode wire plane of around 0.5 mm on TRD1 and around 1mm on TRD2 is observable. The gap occurs between comb numbers ± 25 and ± 26. Comb number ± 25 contains the wires which surround the outer beampipe region and so they are terminated on pcbs which carry signals around the beampipe.

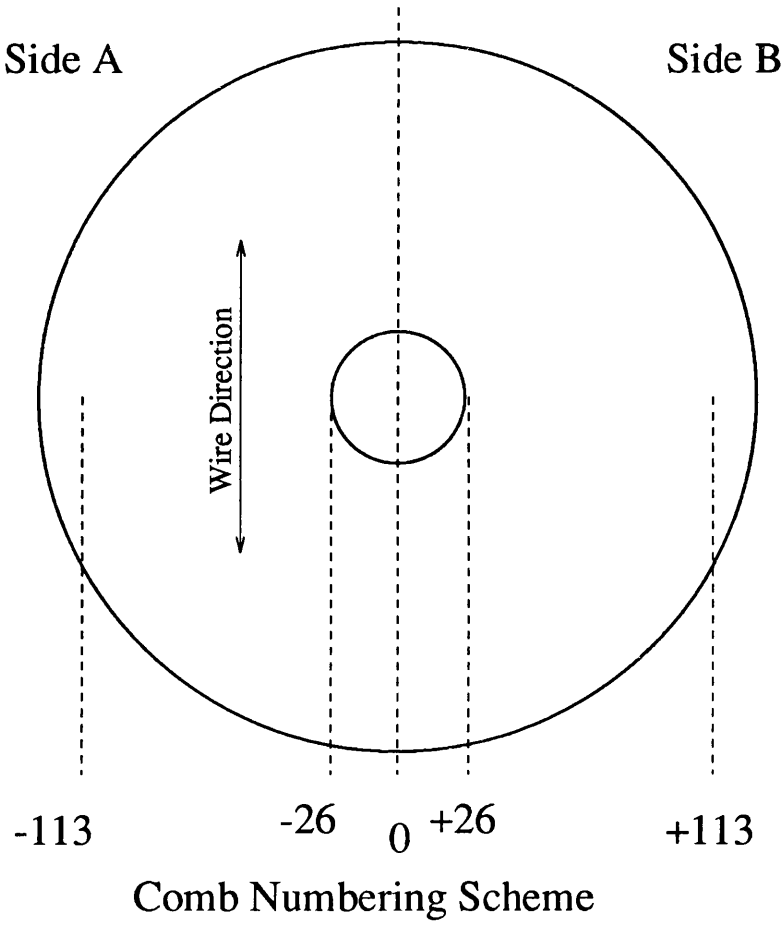

Figure 3.6: *The numbering scheme for combs in the TRDs. The scheme for wires follows the same pattern.*

Thus, they are anchored to the centre of the chambers close to the mid-point of the wires. Comb number ± 26 carries the first "straight-through" set of wires and so is not attached to the central beampipe region, being instead anchored to the outer chamber wall. Secondly, when monitoring tensions over time, it was discovered that almost all cathode wire tensions had decreased since the frame was removed from its wiring table. Both these observations suggest that a deformation of the chamber body has occured. A possible explanation is that the outer G10 frame has flexed inwards after the completion of wiring, but the inner G10 frame has remained flat. Such a deformation would explain the gap in

the wire plane between beampipe and straight-through and the overall decrease in cathode wire tensions. It is thought that when mounted, the chamber frame will recover its shape as the chamber is bolted to a flat vertical frame. Similar difficulties have since been experienced on the cathode plane of TRD2.

3.5.2 Backplate Assembly and Testing

The backplate of each of the TRDs is composed of a copper-coated G10 disc and a raised G10 ring in which are placed metal "feed-throughs". The backplate serves two main purposes. First, it acts as a seal for the drift-chamber within the detector and secondly, it supports the potential and sense wires necessary for the drift-chamber to function. As in the cathode plane, each wire on the backplate must be correctly tensioned to eliminate electrostatic deflection in the presence of large electric fields. For the potential wires, this amounted to a tension equivalent to 0.850 kg and for the sense wires it was 0.080 kg. Each tension is to be accurate to within $\pm 5\%$. Having correctly threaded a wire through the correct feed-through and tensioned it, it was pinned in place. On completion of wiring, readout pcbs were glued in place. Each potential wire was then terminated with a 1 MΩ resistor and each sense wire with a 1 MΩ resistor and a 1 pF capacitor.

Prior to closing up TRD1, atmospheric high voltage tests were carried out to check for possible short-circuits and "sparking" problems on the backplate of TRD1. It was found that the chamber drew unsatisfactorily large amounts of current (typically over 300 μA). Since this severely detracted from the detector's performance, an explanation and course of action was required.

It was thought that that chemicals in the glue are seeping into unpolished surfaces on the G10 glass-fibre ring which supports the feed-throughs and this was providing the channel through which the current flows between wires. The solution involved removing glue from between each of the feed-throughs with a scalpel, thus isolating them electrically. Although not as efficient as would have been desired, this course of action resulted in a much improved value of about 100 μA for total current drawn. As atmospheric humidity plays such an important

role in determining the behaviour of the detector at high voltages, it is expected that this figure can be further reduced to less than 50 μA by immersing the readout electronics in the nitrogen atmosphere which is the working environment of the ZEUS Forward Detector.

After enquiries were made with solvent manufacturers and colleagues at Bonn University, another possible cause was discovered. The araldite mix (5 parts of resin AY103 to one part of hardener HY956) was recommended by Bonn University where the prototype chamber was designed and developed. The mix has since been found to be hygroscopic leading to water crystals being formed as the solvent hardens. These crystals provide a path for current to flow between wires. The solution involved heating both chambers up to 40°C to melt the araldite/water crystals and evaporate away the water content, after which the glue was "painted" with an insulator. This has led to a dramatic decrease in current drawn by the chambers and these are now in the single μA range. The results are shown in table 3.5.

Module	Tested Voltage (V)	Current Drawn (μA)
TRD1	1800	2.5
TRD2	1800	5.0

Table 3.5: *High voltage test results.*

3.6 Installation

Both TRD1 and TRD2 were transported to DESY on Tuesday 17th September 1991. Installation of TRD1 and TRD2 took place in November 1991 following extensive gas and high voltage tests. Both were installed successfully as indicated by post-installation tests. A month later however, TRD2 developed a high voltage problem [56] traced to a broken potential wire. This was repaired in April 1993 during an accelerator shutdown. The detectors were successfully re-installed ready for the Summer 93 physics run, but a delay in delivery of readout

electronics[1] meant that no HERA physics has yet been done with them.

3.7 Suggested Design Improvements

Experience with the current TRD design suggests that a few small changes would have greatly assisted assembly. One such improvement could involve the design and mounting of the combs on the cathode plane. Instead of using just one design of comb for mounting both ends of the cathode wires, two separate types could be used, say type A and type B.

- Type A : The present comb is modified to include two lower lips and has a thin metal slot cut all the way through its upper surface permitting wires to to pass right through it. It should also have a screwthread tapped into its rear vertical surface.

- Type B : The present comb is modified to possess a bridge on its upper surface. The bridge is sufficiently tall to permit a 50μm wire to pass between it and the surface of the comb.

Instead of screwing the comb directly to the detector, a grooved flat mount could take its place. This mount should have two raised edges along its length and possess a rear vertical plate, about 5 mm in height at right angles to the plane of the cathode wires. A "type A" comb, with its lower lips, could then be slid into this mount and fastened through the vertical plate on the mount by a finely pitched bolt. This would allow forward-backward movement of the comb in the direction of the cathode wires simply by turning the mounting bolt, hence easily permitting fine tension changes to be made.

Instead of soldering the wires to the top of the combs, they could be fed through the slot in the comb and another in the flat mount and trapped underneath the mount when it is bolted to the detector. Ideally, each cathode

[1]Although the TRDs use the same readout electronics as the CTD, the CTD operation took precedence.

wire would be terminated at one end by a metal sphere or disk (a ball-end). Each wire would then be fed through a "type B" comb so that the ball-end sits flush with the end of the comb and the cathode wires can be stretched across to the other comb, slotted through the slot on the type A comb and trapped under the mounting plate. This method, although mechanically more complicated, and no doubt more expensive, would remove the problems associated with soldering very thin wires and assist rectification of low tension wires.

Some thought should also be given to curing the flexing of the chamber body. It could be reduced by having more rigidity in the direction of the wires, for example, carbon fibre rods within the cathode casing parallel to the wire direction. The detectors (and hence the wires) straighten out when bolted to the FDET mount. This necessarily increases the tensions in the wires and may have been the cause of the broken wire in TRD2.

3.8 Summary

TRD1 and TRD2, part of the overall ZEUS transition radiation detector, were successfully assembled, tested and installed during 1991/92. A number of points were noted :

- There is definite evidence that the cathode wire tensions are sufficient to distort the detector frame. Thus, when mounted on the ZEUS forward detector, the frame straightens abruptly and increases wire tensions significantly. For future reference, the inclusion of denser glass fibre or carbon fibre rods/strips built into the outer frame and oriented parallel to the wire direction may help.

- Care must be taken when insulating the backplate feed-throughs from each other. Prior investigation of sealant properties, especially electrical and water-retention characteristics, would have saved some valuable time and effort.

- Investigations at DESY into the chambers' gas tightness revealed that gas was escaping from the chamber via the readout electronics' access holes cut into the frame. This was solved using a flexible sealant (SilGard).

The latest TRD status (May 1993) is that the gas leak rate is less than 20 ml/min for all 4 modules of the detector. Anode (and cathode) dead channels are 8 (17) for TRD1, and 18 (16) for TRD2. Readout electronic tests are scheduled to begin in October of this year.

Chapter 4

Event Selection

4.1 The HERA Machine in 1992

In 1992, HERA ran with ten proton bunches colliding on ten electron bunches. Of the ten bunches in each beam, there was nearly always one unpaired electron or proton bunch (called the pilot bunch). Its purpose was to measure the background due to beam particle interactions with residual gas molecules in the beam line.

The beam interaction length was about 40 cm, dominated by the proton bunch length and beam lifetimes were of the order of 50 hours for protons and a few hours for electrons. The two running periods in 1992 contributed 2.1 nb^{-1} (Summer run) and 25.8 nb^{-1} (Autumn run) to the total integrated luminosity of 27.9 nb^{-1} of the data presented here. The statistical error on the luminosity is negligible but the systematic error is estimated to be approximately 5%. A graph of the day-to-day increase in integrated luminosity is shown in figure 4.1.

4.2 Status of ZEUS

Of the sixteen component detectors listed in Chapter 2, a number were either not functioning, partially functioning or operating differently from design. These include the VXD, CTD, FDET, RTD and LPS. With the exception of the CTD which was operated with Z-by-timing and only used to find event vertices, none of

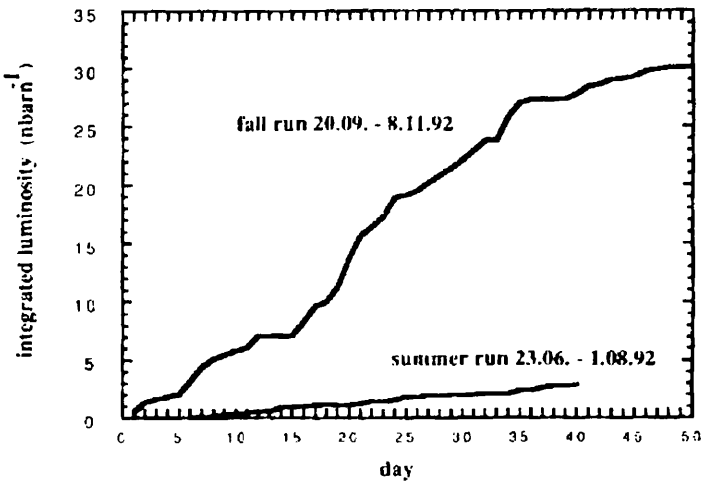

Figure 4.1: *The integrated luminosity for Summer and Autumn 1992 physics runs.*

these components were used in this analysis. The proposed magnetic field value of 1.8 T was reduced to 1.43 T to keep stresses on the calorimeter to within safe design values.

The uranium calorimeter, which provided the data used in this analysis, performed well during the two data-taking periods but 'sparking', thought to be caused by discharges in the PMT base or between PMT cathodes and shielding, did cause problems in the first level trigger. The signature of the phenomenon was an appreciable deposit of energy, random in time, registering in one of the two PMTs assigned to a cell, with very little energy elsewhere in the calorimeter. The majority of afflicted cells were in the BEMC. Algorithms have been developed and were employed in the 1992 runs in both the SLT and TLT to filter out such events.

4.3 Trigger Setup

The data reported here were collected using a trigger relying solely on the information from the calorimeter and the beam-monitoring counters (C5). The

luminosity available from HERA in the Autumn 1992 period was such that only the first and second level triggers were needed to produce an acceptable trigger rate.

For triggering, the calorimeter readout was grouped into 448 non-overlapping trigger towers having a transverse size of about 20 cm $\times$ 40 cm constructed by summing the signals from adjacent calorimeter readout towers. A first-level trigger was issued whenever the energy sum in any of the EMC (or FCAL HAC) trigger towers exceeded a programmable threshold. The data gathered in this analysis were mainly collected as a result of trigger signals from the EMC sections of the RCAL and BCAL where the thresholds were set at 2.5 GeV, except for the towers adjacent to the RCAL beampipe where a much higher threshold of 10 GeV was used. First level triggers were vetoed if their signals were received in coincidence with a signal from the C5 counters which was in time with the proton beam, although this only happened in about one in every thousand events. The total first level trigger rate was 8 Hz. A loose cut based on average FCAL and RCAL arrival times was employed by the third level trigger to reject about 35% of all triggers reaching this stage.

Monte Carlo techniques were needed to study the trigger acceptance. In general, the acceptance increases with increasing Q^2 and is approximately flat in x. For $x > 3 \cdot 10^{-4}$ and $Q^2 > 8$ GeV^2, it exceeds 97.5%. The overall efficiency of the hardware was greater than 99% in all regions of x and Q^2. The sensitivity to defects in the trigger was reduced due to multiple thresholds.

4.4 Proton-induced Beam Gas Background

Interactions between protons in the beam and residual gas molecules present in the beamline because of non-ideal vacuum conditions give a large background to ep physics events. A beam-gas event, if it happens upstream of ZEUS (ie. before the detector coming from the proton direction), can deposit energy in the rear calorimeter where it enters from the wrong side compared to a real ep event.

Thus, it could fake interesting physics. One way of reducing the effect of these beam-gas events is to consider the timing of energy deposits in the calorimeter. When a cell registers a 'hit', the front end electronics produce two quantities - a time and an energy. If the time recorded by a cell is earlier than the bunch crossing time, then clearly the event cannot be attributed to a genuine *ep* collision.

The average time measured by each calorimeter (t_F, t_R, t_B) for FCAL, BCAL and RCAL respectively is weighted by the energy of the cells involved and an offset is applied such that $t_{F,R} = 0$ ns for an *ep* event. Beam-gas events with energy in FCAL also have $t_F = 0$ ns but when they deposit their energy in RCAL, t_R differs from 0 ns by the time it takes the particles to traverse the detector, which is about 11 ns. For beam-gas events in RCAL, it is expected that $t_R = -11$ ns, where the minus sign indicates that the events occured before the bunch crossing time. Application of calorimeter timing cuts must take into account the non-negligible sizes of the proton and electron bunches. For upstream beam-gas events, both t_F and t_R depend on the size of the proton bunch but their difference $t_F - t_R$ does not. For *ep* events, t_F depends on the proton bunch length but only very slightly on the electron bunch length and vice versa for t_R. The difference of the two times is then dominated by the length of the proton bunch. The displacement of a bunch, which varies from run to run, is accounted for by an additional run-dependent offset.

The timing resolution of the calorimeter is energy-dependent so it is required that a certain minimum energy be deposited in the cell to get accurate timing. The resolution is approximately 5 ns at 100 MeV and 3 ns at 200 MeV. The resolution increases to a plateau of 0.7 ns for a few GeV. The event time for the whole calorimeter is determined from the time reconstructed in the individual channels by averaging over many channels ignoring those below a minimum energy cut (at the trigger level, this is 1 GeV for beampipe towers).

The standard method of rejecting beam-gas events using the calorimeter timing is to cut on the absolute RCAL time t_R and the FCAL-RCAL difference $t_F - t_R$. As shown in figure 4.2, two peaks are clearly visible. The broader peak

shows the beam gas events while the narrow one, centred at zero, represents the *ep* events.

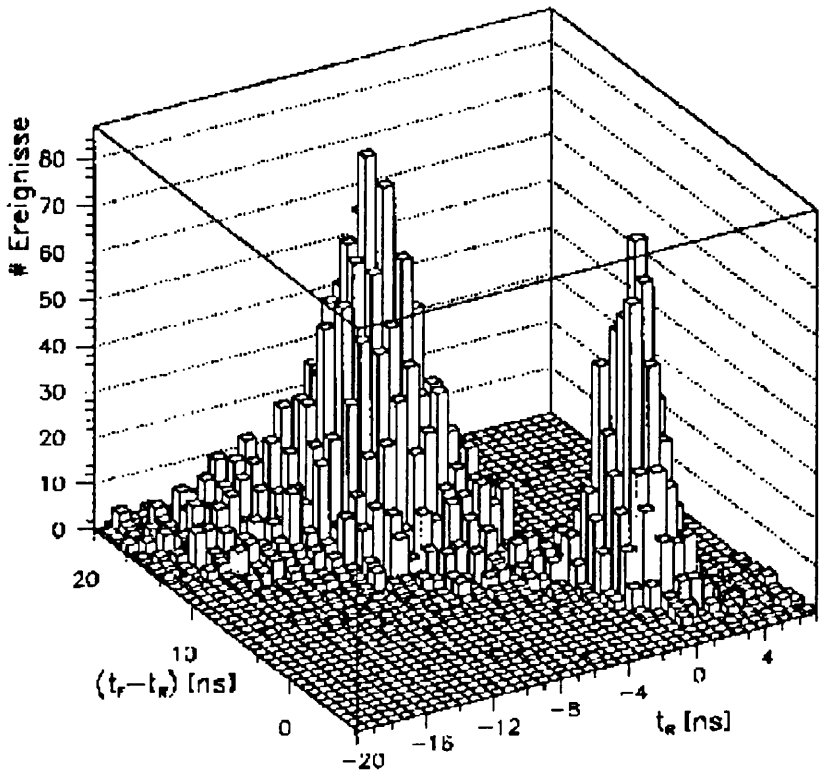

Figure 4.2: *The difference between FCAL and RCAL arrival times for a physics run.*

4.5 Investigation of Global Event Shapes

A study of global event shapes for five different event classes was undertaken :-

- Neutral Current (NC) - Born diagram (zeroth order QCD) events
- Charged Current (CC)
- Photoproduction (BGF) - $O(\alpha_s)$ events

- QCD Compton (QCD-C) - $O(\alpha_s)$ events
- Beam-Gas (BG)

The purpose of the study was to investigate how to distinguish between event classes using only global event parameters such as total event energy E_{tot}, total scalar transverse energy $\Sigma_i E_t$, vector momentum $\overrightarrow{p_i}$ etc. The Monte Carlo programs LEPTO 5.2 and AROMA were used to generate events in the DIS Group kinematic range of $x > 0.0324$ and $Q^2 > 25\text{GeV}^2$. This x value marked the (arbitrary) boundary for low x physics and the Q^2 value took the study clear of low Q^2 photoproduction background.

The investigation centered on three global variables :-

1. $\sum_i (p_{t_i}^{in})^2$: This quantity is the sum of the transverse momentum of each particle in the event. When maximized, it defines a *plane* containing (almost) all the highest p_t particles. Another quantity, $\sum_i (p_{t_i}^{out})^2$, measures the p_t not contained in the plane.

2. *Circularity* : An extension of the $\sum_i (p_{t_i}^{in})^2$ and $\sum_i (p_{t_i}^{out})^2$ calculations, it is defined by

$$\text{circularity} \;=\; 1 \;-\; \frac{A-B}{A+B}$$

where

$$A \;=\; \text{maximized} \;\sum_i (p_{t_i}^{in})^2 \;\text{and}\; B \;=\; \text{minimized} \;\sum_i (p_{t_i}^{out})^2$$

3. E_{trans} : This quantity is the scalar sum of the individual E_{trans_i} for each particle in an event. It is approximately equal to the sum of the scalar p_{t_i} for each particle in the event.

The analysis was carried out at the calorimeter cell level, this being more representative than a Monte Carlo four-vector analysis and real data was used where possible (i.e. beam-gas events from data runs were used). After studying plots of each quantity, a series of cuts were made to attempt to maximize NC event

Cut	NC	CC	BG	BGF	QCD-C
$\sum_i (p_{t_i}^{in})^2 > 20$ GeV^2 . AND . $E_{trans} > 16$ GeV	97%	86%	18%	14%	8%
Circularity < 0.2 . AND . $E_{trans} > 16$ GeV	96%	90%	8%	14%	10%
$\sum_i (p_{t_i}^{in})^2 > 37$ GeV^2	94%	77%	22%	9%	3%
Circularity < 0.2	97%	96%	51%	30%	32%

Table 4.1: *Acceptance for different event types under a variety of cuts.*

selection. The results of the study showing the percentage of events accepted after an experimental cut are listed in table 4.1.

For good separation of neutral current and charged current events from photo-gluon fusion and QCD-Compton events, an acceptance cut of :-

$$\text{Maximized} \sum_i (p_{t_i}^{in})^2 > 37 \text{ GeV}^2$$

seems the most appropriate discriminator.

The study was useful to illustrate that it is possible to base event type selection algorithms purely on global event values but these cuts were not adopted for the analysis.

4.6 Initial Event Selection

The DIS events studied in the following sections were isolated from the rest of the available data using two selection algorithms. Whether an event was selected depends on the outcome of a logical .OR. decision from the two approaches :

Algorithm 1

1. Reject the event if the signals from the C5 beam monitor are out of the correct time window.

2. Reject the event if the calorimeter timing does not correspond to an *ep* event.

3. Reject the event if no BEMC or REMC triggers are received. This cut is motivated from the fact that in a neutral current DIS event, a scattered electron is present in the calorimeter and the BEMC and REMC thresholds are set low enough to trigger on it. An REMC trigger will register if the energy in the REMC is greater than 2 GeV. An BEMC trigger will register if the energy in the BEMC is greater than 5 GeV. If both triggers fire, the logical condition for acceptance is $E_{REMC} > 2$ GeV *or* $E_{BEMC} > 5$ GeV.

4. Reject the event if there is a spark candidate in the BCAL. A spark candidate is defined as a recognized electron candidate with energy greater than 2.5 GeV, consisting of only one cell with an identified bad channel, with empty adjacent cells and the remaining energy in the calorimeter not exceeding 5 GeV.

Algorithm 2

1. Reject the event if the C5 instrumented collimator gives a veto based on the acceptable time window for *ep* events.

2. Reject the event if the calorimeter timing cut does not classify it as *ep* event.

3. Reject the event if the total energy in RCAL exceeds 36 GeV. Including calorimeter smearing effects, it is not kinematically possible for a real *ep* event to have $E_{RCAL} > 36$ GeV.

4. Reject the event if $P_l^- < -32$ GeV, where $P_l^- = \sum_{i,\theta>90^o} E_i \cos\theta_i$. Again, to fail this cut is not kinematically possible for a real *ep* collision. The sum

runs over all calorimeter cells at a polar angle $\theta > 90°$.

5. Reject the event if $\delta = E - p_z = E - \sum_i E_i \cos\theta_i = \sum_i E_i(1 - \cos\theta_i) < 5$ GeV. The sum runs over all calorimeter cells. The same variable δ is used again later. At this stage, the event vertex is artificially set to (0,0,0).

6. Reject the event if no electron with energy greater than 4 GeV is found. The electron must be found by at least one of two different electron finding algorithms. The techniques of electron finding are summarized later in this chapter.

7. Reject the event if it is a spark candidate. Here, a spark candidate is defined as an event where only cell is assigned to the identified electron and the total remaining energy in the calorimeter does not exceed 1 GeV.

The DST selection accepted $2.7 \cdot 10^5$ events from a total of $5 \cdot 10^6$ triggers. Cosmics were then removed using an algorithm based on the topology of cosmic muon energy deposits in the calorimeter.

4.7 Neutral Current Event Preselection

Further cuts are needed to remove beam-gas interactions, cosmics and photoproduction events. At this stage, variables like P_l^- and P_z are calculated using the reconstructed vertex if available, otherwise a vertex of (0,0,0) is used. A vertex is obtained from a fit to reconstructed tracks in which two or more tracks contribute to the fit and the reduced $\chi^2 < 10$. 53% of the final event sample met this criterion. The preselection cuts take the form :

1. Calorimeter timing must be consistent with *ep* event classification. However, tighter cuts are imposed. An energy weighted time average in FCAL and RCAL is made, where only PMT's with an energy greater than 200 MeV contribute and the maximum weight is 2 GeV. The applied cuts are :

$$-6 \text{ ns} < t_F < 6 \text{ ns} \tag{4.1}$$

$$-6 \text{ ns} < t_R < 6 \text{ ns} \tag{4.2}$$

$$-6 \text{ ns} < t_F - t_R < \left(\frac{t_R}{2} + 6\right) \text{ ns} \tag{4.3}$$

Events which do not pass these cuts are rejected. If the times are not calculable, the event is accepted by default.

2. Reject the event if it was recorded while the CTD HV was not turned on.

3. Reject the event if test triggers are registered.

4. Reject events belonging to empty or pilot bunches.

5. Reject spark candidates. These are now defined by the most energetic cell having $(E_{left} - E_{right})/(E_{left} + E_{right}) > 0.9$ where $E_{left,right}$ refers to the PMT's assigned to the cell. Neither side must be in the bad channel list or be an electron candidate with only one cell and zero imbalance.

6. Reject events with vetoed by the veto wall.

7. Events which the TLT flags as being beam-gas interactions are rejected.

8. If the LUMI electron calorimeter registers an electron candidate, its energy must not exceed 5 GeV. Since neutral current DIS events produce an electron in the calorimeter, no such electron may be found in the LUMI. This cut helps to get rid of photoproduction events which fake an electron in the calorimeter when the actual electron was found in the LUMI. Events not passing this cut are rejected.

9. Reject the event if $P_z = \sum_i E_i \cos\theta_i < -33$ GeV.

10. Reject the event if $E_{RCAL} > 35$ GeV.

11. Reject the event if δ is not in the range 32 GeV $< \delta <$ 60 GeV. This cut can be understood as follows. $E - p_z$ can be written :

$$E - p_z = (E - p_z)_{had} + (E - p_z)_{elec} \tag{4.4}$$

with $(E - p_z)_{had}$ equal to $2E_e y_{JB}$ from equation (1.11) and

$$(E - p_z)_{elec} = E_L(1 - \cos\theta_L) = 2E_e(1 - y_{elec}) \tag{4.5}$$

from table 1.3. Thus,

$$E - p_z = 2E_e(1 + (y_{JB} - y_{elec})) \tag{4.6}$$

which, since it concerns the same kinematic variable y will be approximately equal to $2E_e = 53.4$ GeV in DIS events. $E - p_z$ can exceed 53.4 GeV due to calorimeter smearing effects but can also be considerably lower in events with hard initial state QED radiation (the electron energy is consequently reduced). The cut is a versatile one :

- Photoproduction events in which the electron stays in the beampipe but which are selected because an energy deposit has been falsely interpreted as the scattered electron have a low δ.
- Background events from proton beam-gas interactions upstream of the detector also have a low δ.

With these cuts, the DST sample was reduced to 14574 events. Both this set of cuts and the preceding initial selection cuts were performed before the data was made available to the general user for analysis.

4.8 Final Experimental Cuts

A set of experimental cuts designed to further reduce background contamination have been implemented [57]. The cuts are as follows :

1. An identified electron (see next chapter) was required to tag the event as a neutral current one. The electron energy must be above 5 GeV to reduce the background from falsely identified hadrons.
2. EMC cells with an energy deposit of less than 60 MeV and HAC cells with less than 110 MeV were not considered. Cells were also ignored if an

individual photomultiplier tube (PMT) contained less than 30 MeV for an EMC or 45 MeV for a HAC cell. The cuts were chosen to minimize the influence of noise on the measurement of kinematic variables.

3. The energy deposited in the forward calorimeter must be greater than 1 GeV in an attempt to reduce event sample contamination by possible electron-residual gas interaction background. Monte Carlo tests indicate that this cut removes all these latter events at the expense of only $\approx 1\%$ of DIS events. However, subsequent investigation (described in section 5.10.4) showed that one Monte Carlo model is very sensitive to this cut.

4. The reconstructed Q^2 for each event should be greater than 10 GeV^2. This is equivalent to a fiducial cut on the electron and forces it out of the rear beampipe area where accurate measurement and reconstruction is difficult.

5. A cut of 10° was made on each calorimeter cell which registered a hit in an event. Only cells which had $\theta_{cell} > 10°$ were accepted. This cut loosely defines the first ring of calorimeter cells which surround the beampipe hole in the forward direction. The purpose of the cut was to reduce the influence on the distributions of the proton remnant.

6. δ for the event is required to be greater than 35 GeV.

7. Reject the event if $y_{JB} < 0.02$ (equivalent to $\delta_{had} < 0.04E_e$). Events which do not satisfy this cut are known to be poorly reconstructed as they suffer from noise effects and the calorimeters' finite resolution [58].

From the preselected neutral current event sample of 14574 events, application of the above cuts selected 2127 events. The x-W^2 distribution of these events is shown in figure 4.3.

It should be noted that the previous three sets of cuts are standard ZEUS Collaboration DIS cuts.

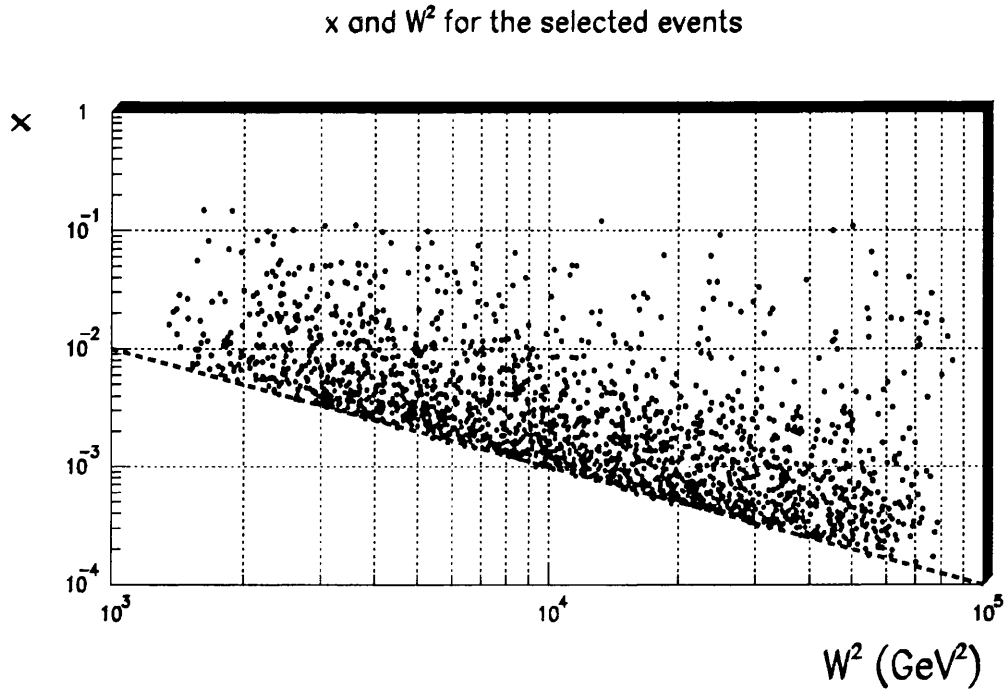

Figure 4.3: *Distribution of the selected data events as a function of* W^2 *and* x. *The dotted line represents the relation* $W^2 = Q^2(1-x)/x$ *with* $Q^2 = 10$ GeV^2.

4.9 Kinematic Reconstruction

A check was also made on the effectiveness of the reconstruction of Bjorken x. For the purposes of this analysis, a cut on reconstructed x has been made such that events are sorted into regions :

1. low $x \rightarrow x < 10^{-3}$
2. medium $x \rightarrow 10^{-3} < x < 10^{-2}$
3. high $x \rightarrow x > 10^{-2}$

The place where the importance of accurate kinematic reconstruction of x shows up is in the analysis of detector data where information is lost in calorimeter cell cracks, through the beampipe or by "sparking" photomultiplier tubes. All these effects contribute to a loss of accuracy in kinematic reconstruction.

Monte Carlo studies show that typically 10% of the low x events will migrate because of inaccurate reconstruction into the medium x bin while approximately 8% of the medium x sample migrates in the opposite direction. No events move between the low x and high x bins, while 50% of the high x events should be in the medium x bin and 10% of the medium x events should be in the high x bin. To attempt to correct for any false x reconstruction, the production of correction factors was made "x-sensitive". Thus when applied to the actual detector data, the influence of incorrect x reconstruction was reduced. This was achieved at the stage of correction factor determination by filling the four-vector histograms ("generated" data) according to the true x value given by the generator involved and filling the calorimeter histograms ("MC accepted" data) according to the reconstructed value of x. When applied to data, these factors then help to compensate for the migration of events into the wrong x bin. Figure 4.4 illustrates the pattern for a sample of CDM Monte Carlo data. The function :

$$(x_{real} - x_{recons})/x_{real} \tag{4.7}$$

is particularly helpful as it clearly shows the general trend of migration for each x region. Negative values of equation (4.7) imply that the reconstructed value of x is greater than the actual value, while positive values indicate the reverse. This is displayed explicitly in the right hand plots of figure 4.4 where it is shown that in general, kinematic reconstruction by the double angle method overestimates x in the low x bin, but underestimates it in the medium and high x bins. The accuracy of high x reconstruction is such that this region will be neglected in the analysis to follow. For the low x and medium x cases, the migration of events into the wrong x bin, while not negligible, is tolerable. Thus, these two regions will form the basis of the analysis.

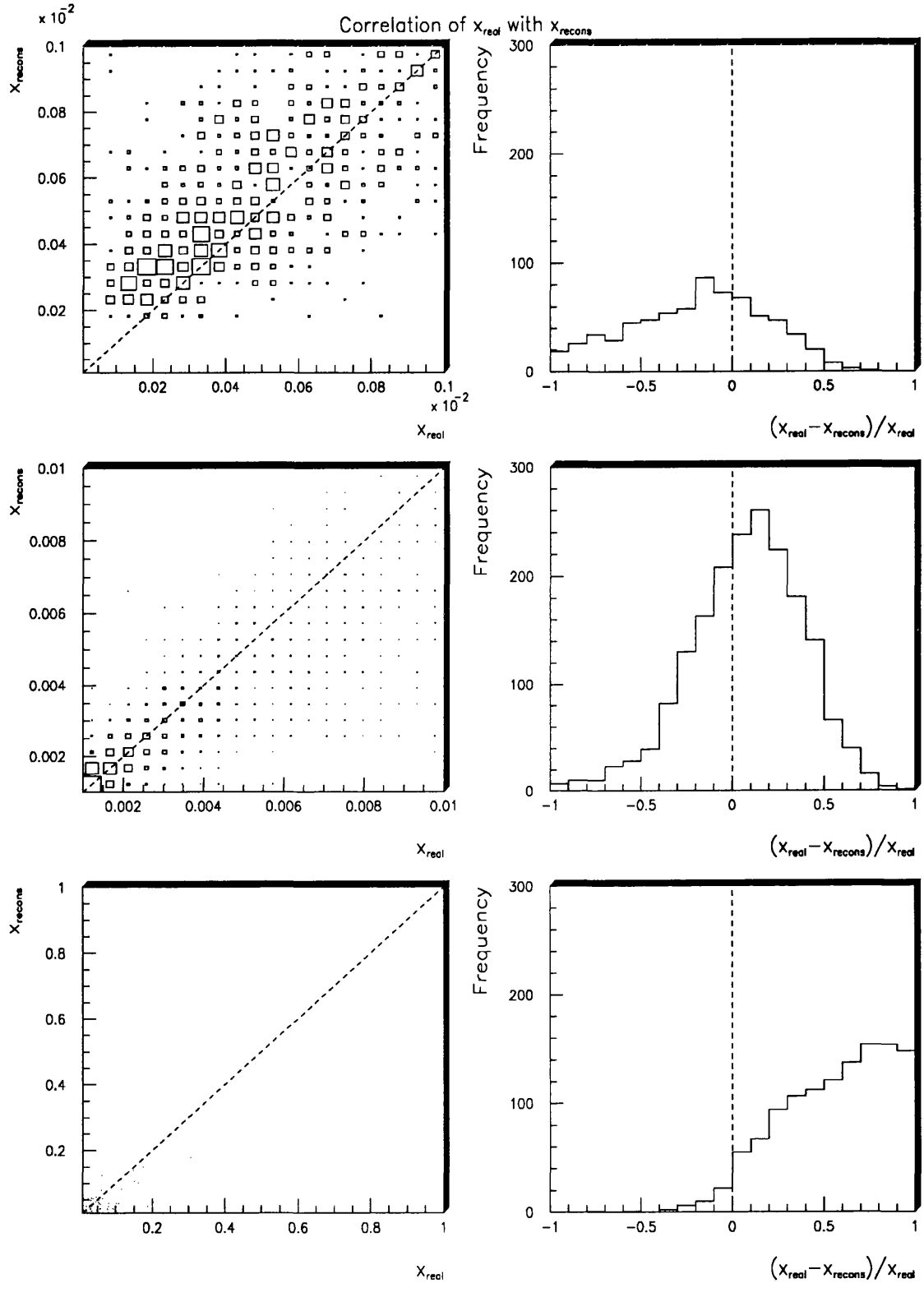

Figure 4.4: *A comparison of true x and reconstructed x values.*

4.10 Calorimeter Energy Reconstruction

The correlations between the real and reconstructed energy sums (per event), for both the full energy and its transverse component, were studied in low, medium and high x bins. The results, shown in figures 4.5 and 4.6 show that in the low x and medium x regions, there is good correlation between true transverse/full energy and reconstructed transverse/full energy. As can be seen from the "pull" plots, the low x bin shows a negative offset indicating that in general, the reconstructed value of the total energy is less than the true value. This is to be expected given the general loss of information accrued when a four-vector particle moves through dead material, loses particles by decay and suffers from the imposition of calorimeter cell noise cuts. The medium x events also show a slight negative offset for the same reasons. The high x events show a much bigger offset in the opposite direction attributable to the influence of the proton remnant in the forward direction.

4.11 Electron Identification

An important task in selecting neutral current DIS events is to identify the scattered electron correctly. For the purposes of this analysis, a cone-based electron identification algorithm ("Elect1") has been used. It works on the principle of analysing the topology of the energy deposited in the calorimeter cells and identifying EMC cells with high energy content (candidate cells). Inner and outer cones are then constructed around these candidates. Hadrons typically produce wide showers that extend deep into the calorimeter whereas electromagnetic showers show a small lateral and longitudinal spread in energy deposition. The discrimination between an electron and a hadron is based on the energy weighted mean radius of the EMC energy deposits within the inner cone and a combination of the EMC energy and the ratio of HAC to EMC energy in the outer cone. When applied to the data, it enables x to be reconstructed and

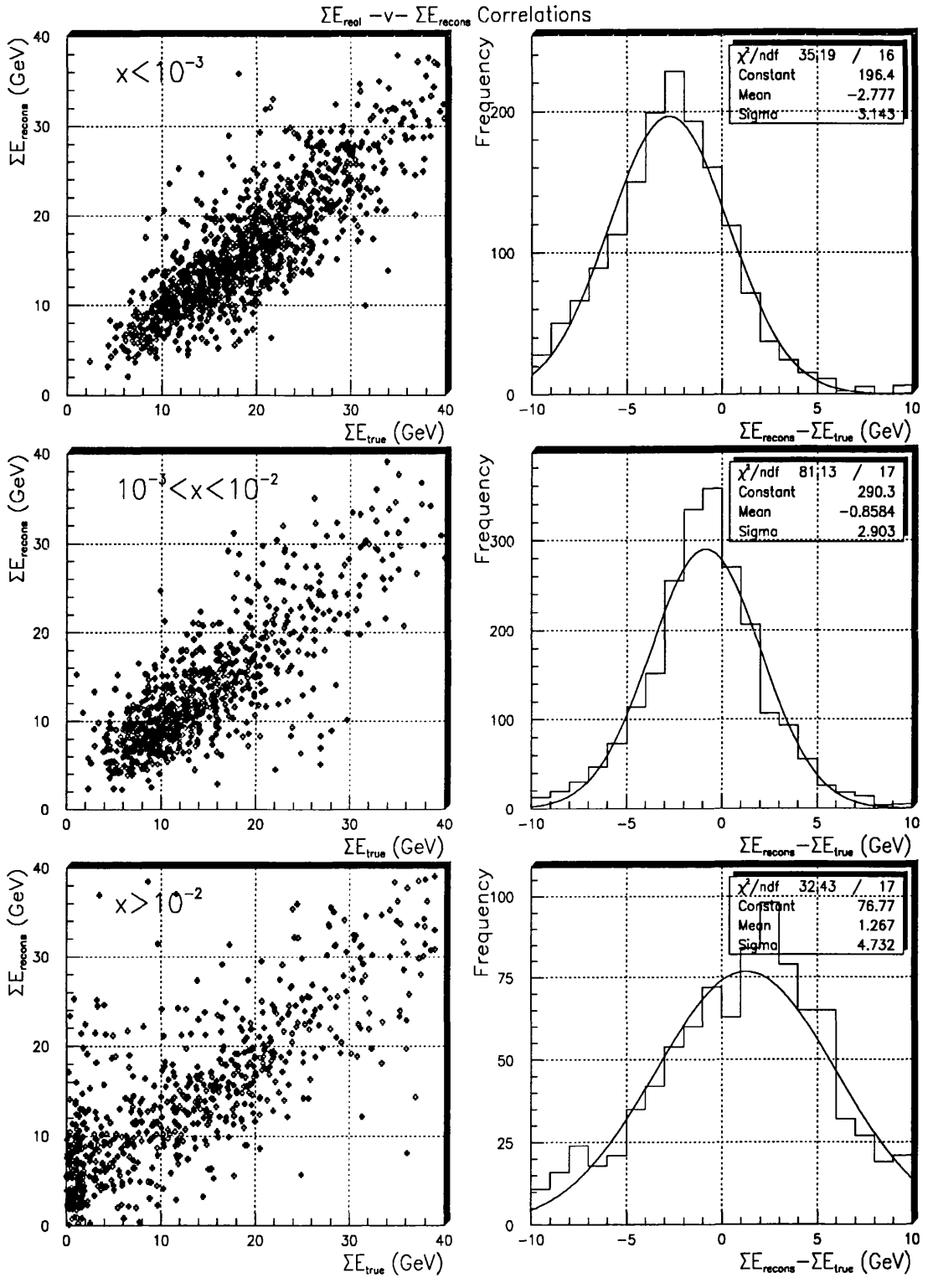

Figure 4.5: *Correlations in the total energy per event for true Monte Carlo data against reconstructed Monte Carlo data in each x bin.*

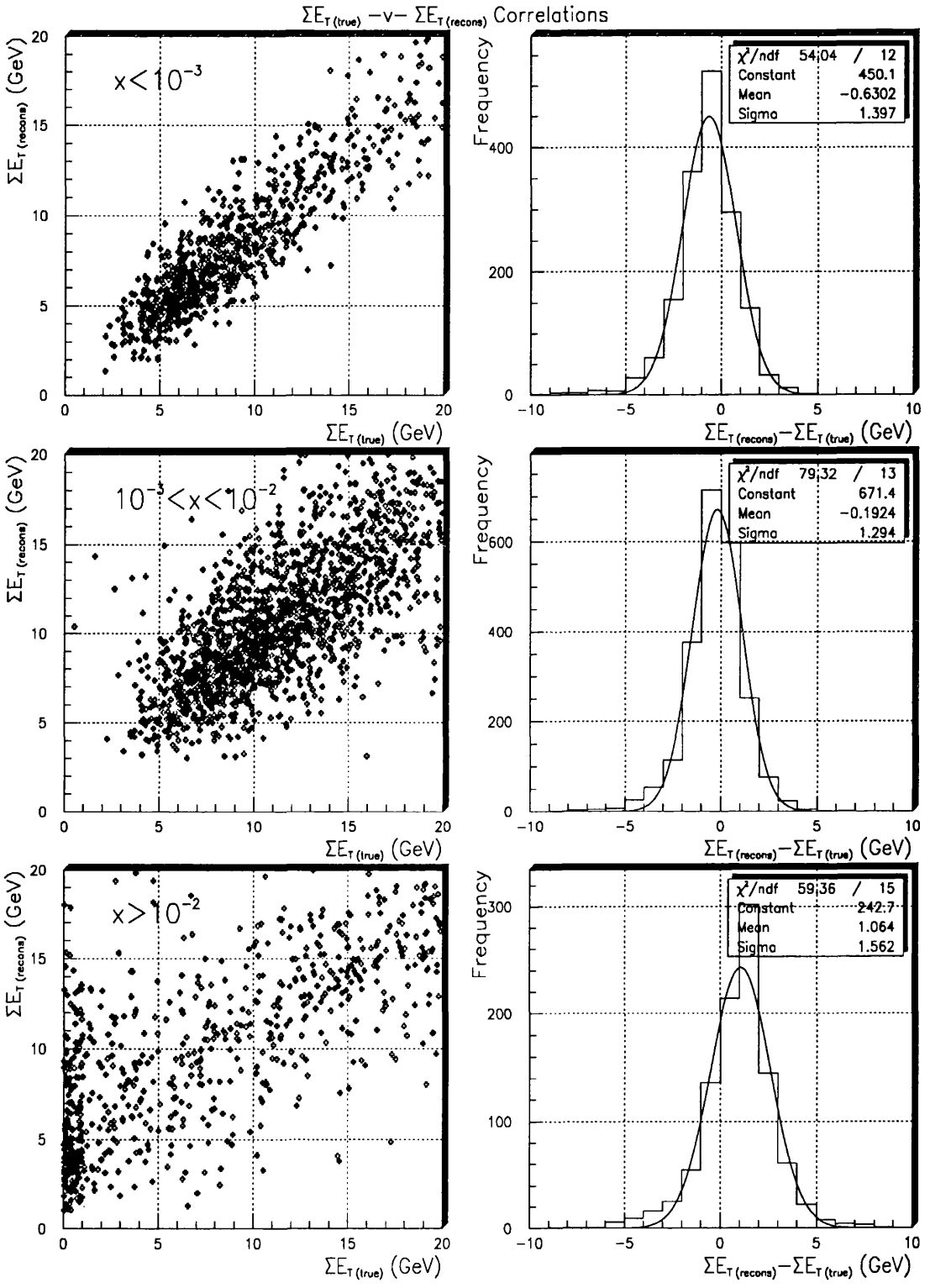

Figure 4.6: *Correlations in the total transverse energy per event for true Monte Carlo data against reconstructed Monte Carlo data in each x bin.*

binned according to the previously mentioned scheme. The breakdown of events in the various x bins is given in table 4.3.

4.12 Photoproduction Background

An important source of background to DIS events comes from resolved photon interactions where part of the photonic remnant can enter the electromagnetic calorimeter, faking a scattered electron signal. An estimate of the contribution to the selected DIS data sample of photoproduction events was calculated. A set of minimum bias PYTHIA photoproduction events covering a known range of y were passed through the analysis chain and of the 7216 events analysed, only 11 passed the experimental cuts described earlier. The data was broken down into three y ranges as listed in table 4.2.

PYTHIA Photoproduction sample				
Step		$0.6 < y < 0.75$	$0.75 < y < 0.88$	$0.88 < y < 0.99$
1	# evts read	2438	2460	2318
2	# events accepted	1 ± 1	2 ± 1.41	8 ± 2.83
3	$\sigma_{\gamma p}$ (nb)	0.55×10^3	0.40×10^3	0.30×10^3
4		Integrated Luminosity 27.9 ± 1.4 nb^{-1}		
5 = 3 × 4	Expected # evts	15317 ± 769	11231 ± 564	8249 ± 414
6 = (5/1) × 2	Expected # photoprod. events	6.3 ± 6.3	9.1 ± 6.5	28.5 ± 10.2

Table 4.2: *Photoproduction background calculation.*

Using the figure obtained from the photoproduction sample in table 4.2 and the breakdown of DIS events shown in table 4.3, it can be calculated that the

x range	# DIS events	# Photoproduction events
$10^{-4} < x < 10^{-3}$	632	10
$10^{-3} < x < 10^{-2}$	1200	1
$10^{-2} < x < 1$	295	0
Total # events	2127	11

Table 4.3: *Breakdown of events for the observed DIS data sample and PYTHIA photoproduction Monte Carlo sample.*

selected DIS data sample is contaminated by photoproduction events to the level of $6\% \pm 3\%$ in the low x region and $2\% \pm 1\%$ overall.

4.13 Summary

A series of experimental cuts were performed on available ZEUS data to obtain a DIS sample of 2127 events covering the range $10^{-4} < x < 1$ with $Q^2 > 10$ GeV^2. Investigation reveals that the high x region, $> 10^{-2}$, is not accurately reconstructed and so has not been considered in the analysis to follow. In addition, reconstruction of total energies by the calorimeter is shown to be reasonable in the medium and low x regions. The potential contamination of the observed DIS sample by photoproduction events is studied and calculated to be of the order of $2\% \pm 1\%$ overall.

Chapter 5

Analysis and Results

5.1 Outline

The purpose of the study is to distinguish between some of the currently available DIS Monte Carlo models on the basis of their treatment of QCD cascade processes, in particular higher order gluon emission effects. This is to be achieved by comparing and contrasting several simple energy flow distributions generated by Monte Carlo models and their corresponding distributions as observed in the data. Many plots were initially investigated - for example, $(\sum E_t^{in})^2$, $(\sum E_t^{out})^2$, $< E_t^{out} >$ as a function of W^2, circularity, individual multiplicities, energies and momenta before six were selected :

1. Pseudorapidity $\eta = -\log(\tan\frac{\theta}{2})$ weighted by the cell's transverse energy
2. Pseudorapidity η weighted by the cell's energy
3. Total energy, $\sum_i E_i$, per event
4. Total transverse energy, $\sum_i E_{t_i}$, per event
5. "P_t balance" which plots the azimuthal distribution of cells with respect to the scattered electron, $\phi_{cell} - \phi_{elec}$ weighted by each cell's transverse energy (see figure 5.1).

6. "Delta Eta" $\Delta\eta = \eta_{cell} - \eta_{QPM}$, weighted by cell's energy. η_{cell} is the pseudorapidity of a calorimeter cell while η_{QPM} is the pseudorapidity of the struck quark as estimated by the simple quark-parton model (see figure 5.2)

These plots were chosen with simplicity and information content in mind and highlight three prime areas of interest - energy flow in the detector, overall ("global") event information and the physics of gluon emission.

Energy flow is studied using energy and transverse energy weighted pseudorapidity (η) plots, chosen in preference to polar angle distributions. Transverse momentum p_t (effectively transverse energy as particles are assumed to be massless at the energies high involved here) and rapidity y are natural variables to choose when studying QCD and hadronization phenomena away from high energy remnant radiation. Softer hadronization processes provide a particle flux which is flat in rapidity and azimuth but Gaussian in p_t. In Lorentz invariant phase space, differential cross-section terms contain expressions like :

$$\int \mathrm{d}^4p\ \delta(E^2 - p^2 - m^2) \sim \int \mathrm{d}p^3/2E \sim \int \mathrm{d}y\ \mathrm{d}p_t^2\ \mathrm{d}\phi \tag{5.1}$$

which suggests y, p_t and ϕ variables are appropriate for these event shape studies. A convenient property of rapidity is its additive nature under a Lorentz boost to another frame moving with velocity β parallel to the incident beam direction (z-direction) so that $y' = y + \frac{1}{2}\ln((1-\beta)/(1+\beta))$. Thus, any change in rapidity Δy stays the same in the new frame. Taking all produced hadrons as massless, we can change from rapidity $y = \ln((E + p_L)/(E - p_L))$ to pseudorapidity $\eta = -\ln\tan(\theta/2)$ and use the polar angular information θ from calorimeter cells as the basis for studying the detector's response to both Monte Carlo and real data.

Global information on event structures in the detector is provided by summed energy and transverse energy distributions which show explicitly the mean E_t or E per event. The latter, of course, will not equal the sum of the incoming beam energies primarily because of beampipe losses.

The P_t balance and $\Delta\eta$ plots are designed to illustrate the presence or absence of higher order gluon emission. In the P_t balance plot, gluon emission in the

azimuthal plane will show up in the form of a broader, flatter distribution in ϕ. In the $\Delta\eta$ plot, it shows up as a positive shift from zero because of the recoil imparted on the struck quark by radiated gluons. The P_t balance and $\Delta\eta$ plots will be referred to hereafter as the gluon emission plots.

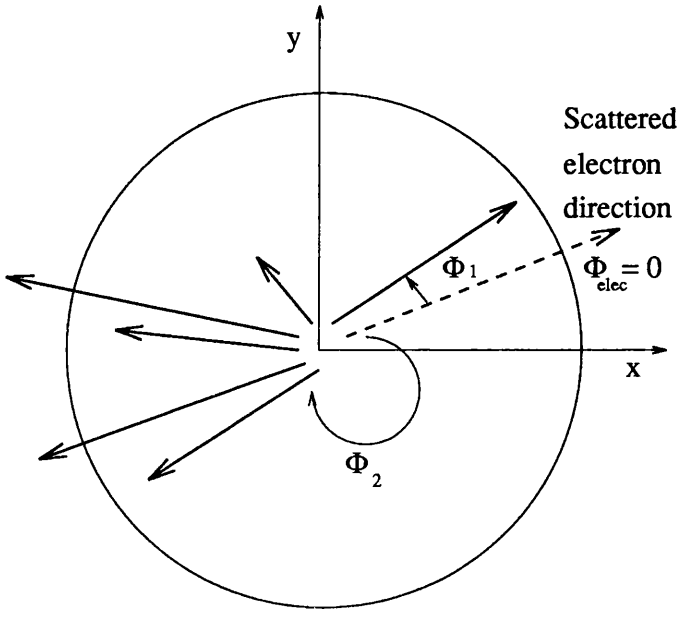

Figure 5.1: *Schematic of the P_t balance calculation.*

5.2 Uncorrected Data Distributions

It is instructive to briefly discuss the form of the observed data distributions for all three regions of x (see figure 5.3) before comparing the low and medium x data with the predictions of several Monte Carlo models. It should be noted that only calorimeter cell information is used in the study. Clustering algorithms leading to the formation of condensates (groups of adjacent cells) are not employed.

Studying first the polar distributions of transverse energy and full energy flow, it is clear that moving between the different x regions causes the pseudorapidity distributions show distinct differences. The E_t weighted plot, which is approximately flat in the range $-1.5 < \eta < 1.5$ for the low x data becomes more peaked

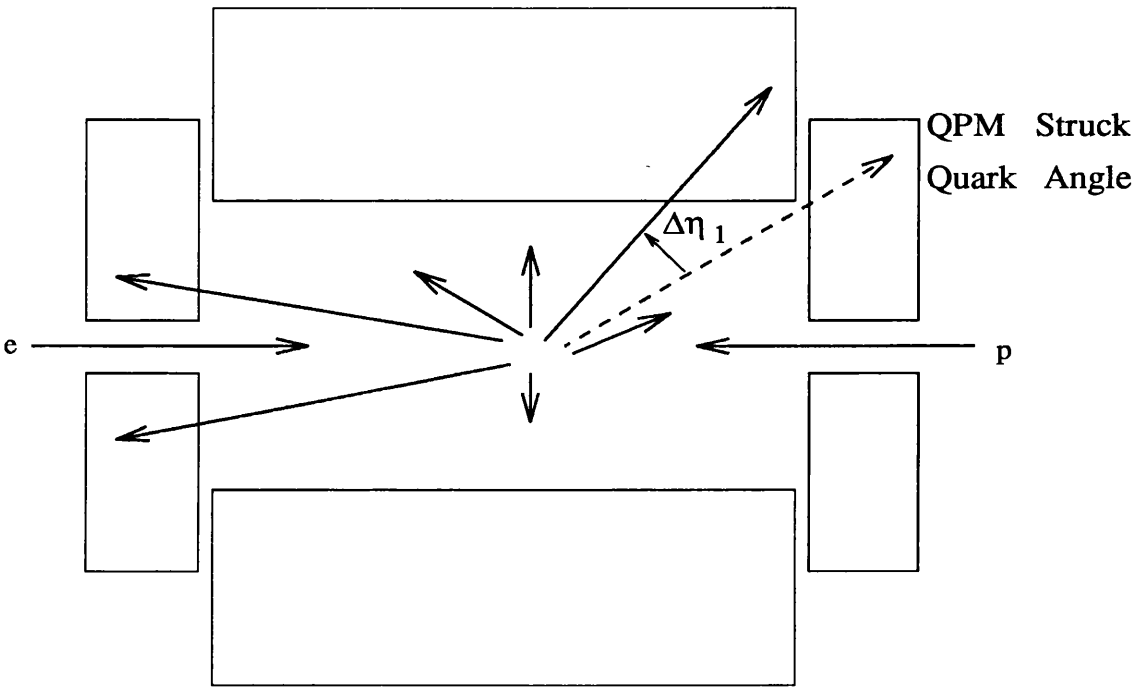

Figure 5.2: *Schematic of the $\Delta\eta$ calculation.*

in the forward region as x increases. This means that the transverse energy of particles in the rear and middle sections of the detector is decreasing as x increases while transverse energy of those in the forward direction increases. ie. in the simple quark-parton model, as we move to higher x, the struck quark gains a bigger fraction of the incident proton's momentum in the +z-direction. Thus, collision with an electron is less likely to cause the quark to be deflected into the barrel or rear calorimeters. The general shift in the flow of hadrons from the backward direction at low x values to the forward direction at high x values is, of course, also illustrated when we consider the flow of total energy as a function of η. At high x, there is virtually no energy from the hadronic system recorded in the rear section of the detector.

Turning to the summed transverse/full energy plots, we can see a net reduction in energy present in the calorimeter as we move from the low x to the medium x data. The low x distribution is peaked at around 15 GeV in the total energy

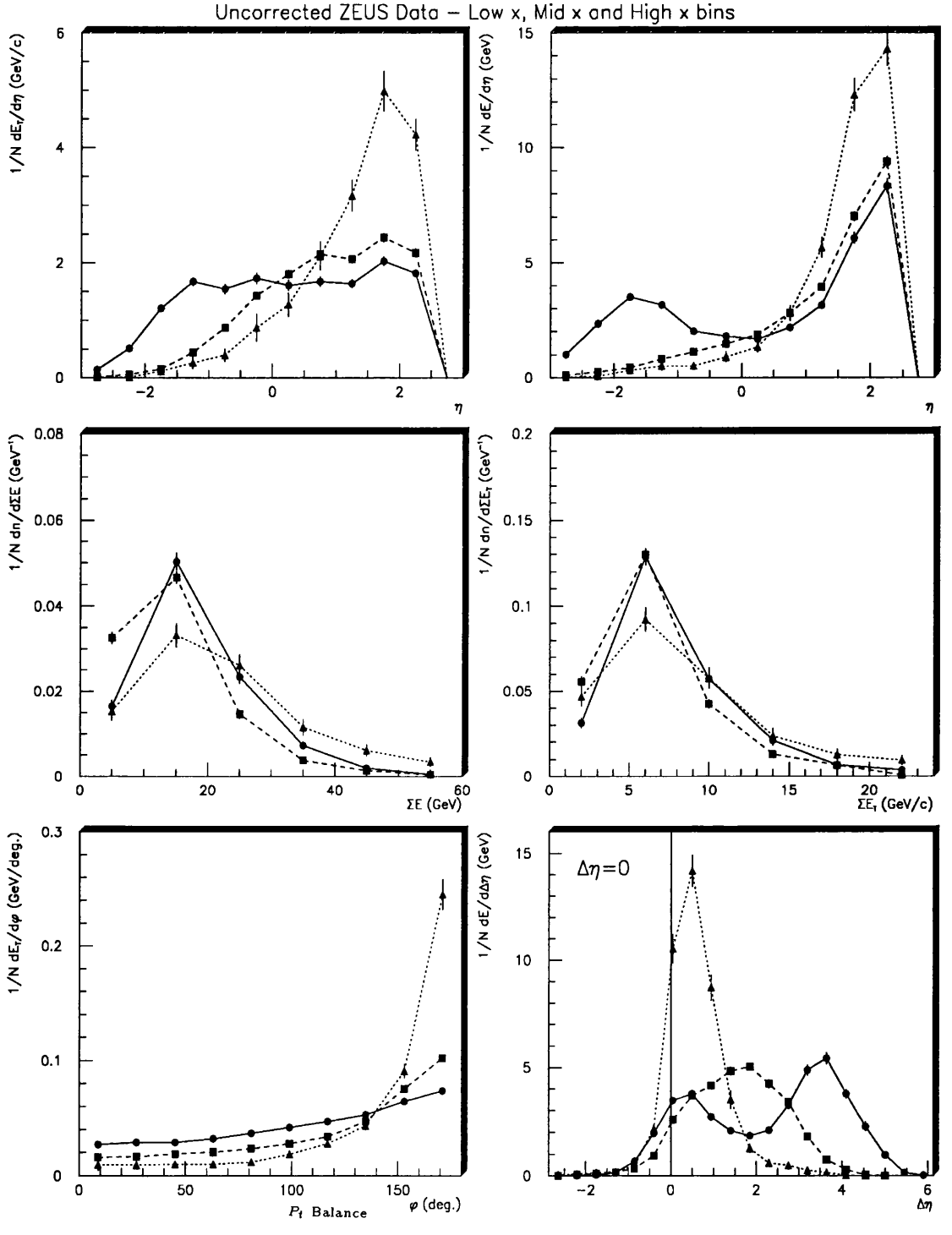

Figure 5.3: *The uncorrected data distributions.*

The solid circles represent the data in the region $x < 10^{-3}$, *the solid squares are for the region* $10^{-3} < x < 10^{-2}$ *and the solid triangles show the region* $x > 10^{-2}$.

plot illustrating the presence of high energy particles in the detector. Moving to the medium x region, this energy is steadily lost because particles have less transverse momentum and greater longitudinal component, taking them into the forward part of the detector where the imposed 10^o cut removes many of them from the analysis. The result is an apparent loss in energy. Normally, the effect would be shown even more clearly in the shape of the high x plot, but it should be noted that combining the high x value with the imposed high y cut of $y > 0.02$ at fixed s means that the events in the high x bin correspond to high Q^2 interactions. This sort of reaction will deposit a significant amount of energy in the BCAL and FCAL.

The P_t balance plot shows how the flow of transverse energy in the calorimeter relative to the scattered electron position varies as a function of ϕ. All plots show a peak at ϕ of 180^o where the E_t of the hadrons balances that of the scattered electron. At low x, there is a broad spread of particles with relatively high transverse energy over all the azimuthal range, rising to a peak directly opposite (in ϕ) the electron position. This pattern suggests the presence of a diffuse spray of hadrons is only partially concentrated in the struck quark direction. The distributions become more peaked as x increases suggesting that fewer particles with significant energy lie between the scattered electron and the struck quark position.

The $\Delta\eta$ plots show the flow of energy between the struck quark and the target remnant. The low x distribution clearly shows a two-peak structure with most of the energy appearing at positive values of $\Delta\eta$. The struck quark is well separated from the remnant and a flow of energy is present between them. There is evidence of a positive shift away from zero in the struck quark peak. The separation of the two peaks becomes less clear as x increases reflecting the way in which the struck quark direction is swinging round to the forward direction. At high x, there is only a slight skewness in the distribution as the struck quark becomes inseparable from the debris of the remnant at low θ.

5.3 Comparison with Monte Carlo Models

In each plot, uncorrected ZEUS data are represented by solid dots. Errors bars on the observed data represent the statistical error only. If they are not shown, they are within the spread of the symbol. Only the low x and medium x regions are studied here for reasons discussed in section 4.9.

None of the Monte Carlo models used for this comparison have been tuned for this analysis, default parameter settings being used where appropriate.

The plots shown illustrate how uncorrected ZEUS data compares to Monte Carlo data which has been passed through the ZEUS detector simulation program (MOZART), the trigger simulation (ZGANA) and the reconstruction package (ZEPHYR).

5.4 Matrix Elements

$x < 10^{-3}$

In figure 5.4, the angular distributions for the ME model are compared to the data. We see that in both plots, there are regions of good agreement, primarily in the extreme backward direction. The transverse energy weighted plot shows disagreement starting at $\eta > -1$ ($\theta \approx 140^{o}$) and the distribution does not recover as we move to forward polar angles. The energy weighted plot overestimates the data in the rear direction, shows reasonable agreement for $-1 < \eta < 1$ ($40^{o} < \theta < 140^{o}$) but then underestimates the data in the forward direction.

The two total transverse/full energy plots indicate that the ME model cannot reproduce the high energy tail seen in the data, indicating that the average energy per event predicted by the model is too low. This is reinforced by the shape of the P_t balance plot where the model consistently underestimates the response of the data except at angles almost directly opposite the scattered electron position. It shows the wrong shape compared to data, being flatter up to $\phi \approx 100^{o}$, then rising quickly. The $\Delta\eta$ plot illustrates the point that the ME model as it stands, even with $O(\alpha_s)$ corrections to the Born diagram, does not accurately model the processes of gluon emission which occur in the data. The data shows a peak at $\Delta\eta \sim 0.5$ while the model centres its peak at $\Delta\eta \sim 0$. In addition, the ME approach cannot reproduce the shape of the remnant peak at large $\Delta\eta$.

$10^{-3} < x < 10^{-2}$

In this region of x, shown in figure 5.5, the agreement between observed data and ME model predictions improves. From the E_t weighted η plot, it is possible to claim good reproduction of the data in the region $-2 < \eta < 0$, but thereafter the model cannot match the high E_t seen towards the backward region of the detector. A similar pattern emerges in the E weighted η plot, this time with good agreement in the range $-2 < \eta < 1$ but the model fails to match the

increase in energy shown by the data beyond this.

Both the total energy and total transverse energy plots confirm the trend seen in the low x data - the model consistently fails to reproduce the high energy events observed in the data. Studying the P_t balance plot, the model again shows the wrong shape compared to the data with activity generally too low until directly opposite the scattered electron position, followed by a sudden jump to values in excess of the data. In the $\Delta\eta$ distribution, we can see that the ME model associates too much energy with the simple QPM prediction of the struck quark direction while underestimating the broader spread of the data to large $\Delta\eta$ values.

5.5 Matrix Elements + Parton Showers

$\underline{x < 10^{-3}}$

Distributions from the ME+PS model, which as described earlier includes both the ME calculation to $O(\alpha_s)$ and additional parton shower processes, are also shown in figures 5.4 and 5.5. In the transverse energy weighted plots, the ME+PS response generally follows the shape of the ME model for $\eta < -1$ but it then rises to values much higher than that seen for the data in the range $-1 < \eta < 1$ before falling away again in the forward direction. In the energy weighted polar distributions, the ME+PS model shows better agreement with the data than the ME approach for $\eta < -1$ but again overestimates the flow of energy in the pseudorapidity range from $-1 < \eta < 1$ and underestimates it for $\eta > 1$.

Unlike the ME model, the ME+PS approach shows quite good agreement in the total E_t and total E plots, accurately reproducing the tail seen in the data. It also fares well in the P_t balance distribution, only beginning to predict a more energetic response than observed in the data at large values of ϕ. However, although the model does show a similar positive shift from zero in the $\Delta\eta$ plot as the data, it overestimates the flow of energy between the struck quark and the remnant (illustrated by the shoulder on the remnant side of the struck quark

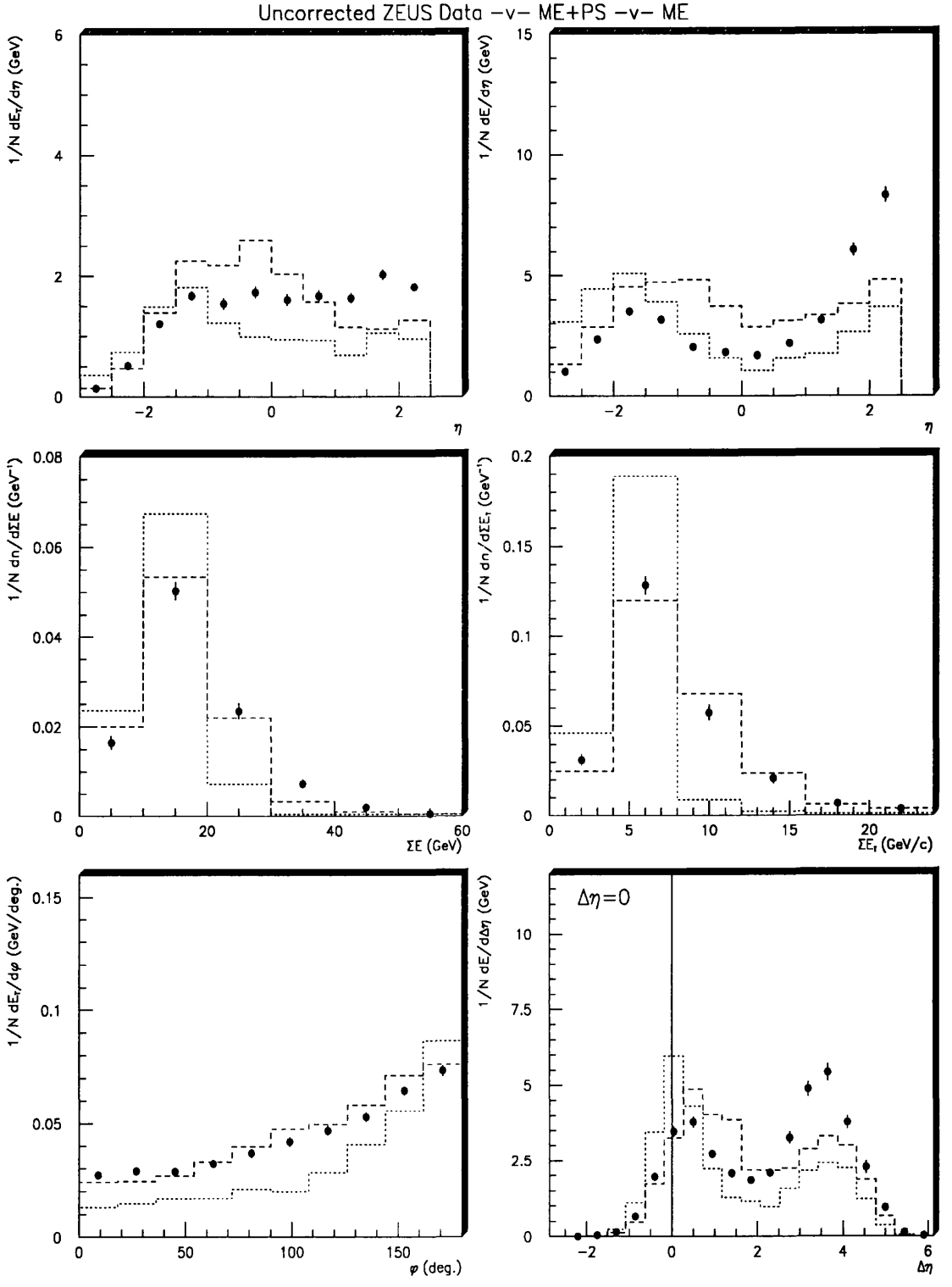

Figure 5.4: *The distributions for ME+PS (dashed) and ME (dotted) compared to uncorrected data for* $x < 10^{-3}$.

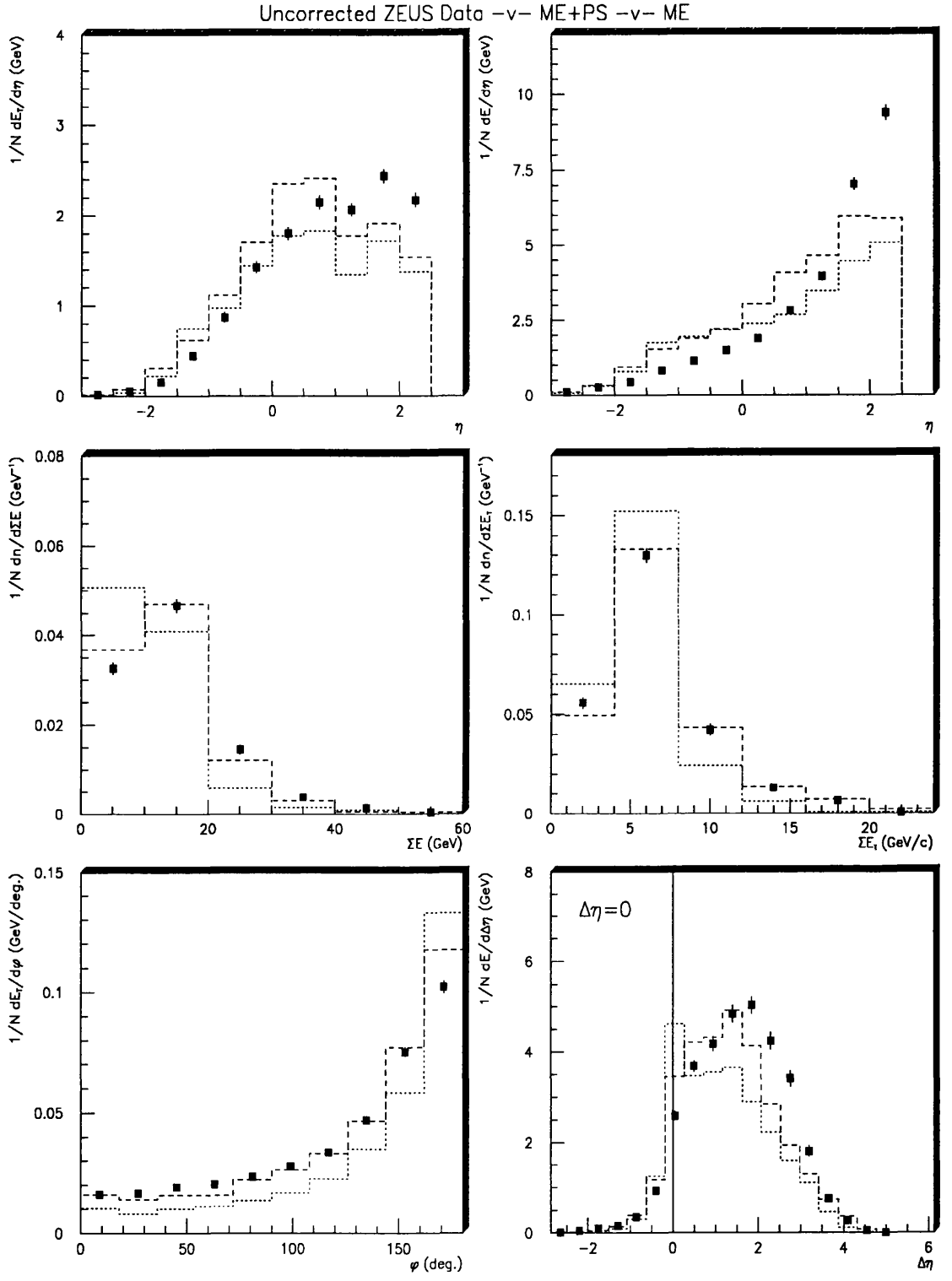

Figure 5.5: *The distributions for ME+PS (dashed) and ME (dotted) compared to uncorrected data for* $10^{-3} < x < 10^{-2}$.

peak) and does not show the magnitude of response seen in the data for the remnant peak.

$10^{-3} < x < 10^{-2}$

The basic pattern illustrated by the low x data is again reflected in the medium x comparison shown in figure 5.5. The E_t weighted pseudorapidity distribution is distorted in favour of the $\eta \approx 0$ region at the expense of the large $+\eta$ direction where the model shows too little activity compared to the data in this forward direction. This is shown more clearly in the E weighted distribution where ME+PS predicts too much energy as a function of polar angle until $\eta \approx 1.5$ ($\theta \approx 25°$) where it is overtaken by the response of the data.

The total energy/transverse energy plots are encouraging with the model correctly predicting the response of the data throughout the range. Combined with the knowledge gained from the polar angle distributions and the low x predictions discussed above, it suggests that the model is assigning the correct energy to an event but distributing it incorrectly throughout the detector, concentrating on energy flow in the mid-sections of the detector rather than in the forward direction. This points to problems in the treatment of the remnant.

The P_t balance plot continues to show the same good agreement with data as observed at low x but there is an overestimated response to transverse energy in directions opposite that of the scattered electron. This response, not seen in the low x distributions, again reflects the mis-assignment of energies by the model. The difficult problem of how to treat the proton remnant is also observed in the $\Delta\eta$ plot where the model does quite a good job in predicting the data response up to $\Delta\eta \approx 2$ and then falls away quite sharply as it nears the remnant region of $\Delta\eta$ space.

5.6 Lund Parton Showers

$\underline{x < 10^{-3}}$

A glance at figure 5.6 will illustrate immediately that the Lund parton shower approach on its own does not reproduce the observed data distributions, regardless of the choice of virtuality scale used in the Monte Carlo. In general, the PS(Q^2) and PS($Q^2(1-x)$) underestimate the data points while PS(W^2) overestimates them. The disagreement is more severe than in the ME approach reflecting the difficulty of modelling hard gluon emission with parton showers. The effect of varying the virtuality scale (which affects the phase space available to emitted gluons) is clearly illustrated. At the small values of Bjorken x involved here, the difference between Q^2 and W^2 contained in the relation :

$$W^2 = Q^2 \frac{1-x}{x} \tag{5.2}$$

becomes evident, the x dependent factor becoming of the order of 100. When given the W^2 scale as the basis for gluon emission phase space, there is clearly a considerable overestimation of particle response in the pseudorapidity range $\eta \approx -1$ to $\eta \approx 2.4$ (polar region $10^o - 140^o$). Adopting a Q^2 scale shows no improvement in agreement with observed data but this time the parton shower model underestimates particle activity in the same pseudorapidity range. The numerical factor $(1-x)\ \max(1, \ln 1/x)$ modifying the Q^2 scale in one choice of virtuality has magnitude ≈ 5 in this low x region. By including this factor, the PS($Q^2(1-x)$) achieves quite good reproduction of the data in the very forward region but follows the trend of the PS(Q^2) scale elsewhere.

Figure 5.6 shows that none of the PS approaches can reproduce the summed energy/transverse energy totals very well. As expected, the PS(Q^2) and PS($Q^2(1-x)$) do not reproduce the high energy tail of the summed energy plot. Neither can they match the observed data's summed transverse energy distribution. The PS(W^2) distributions can match the general pattern of the data energy flow but emphasises the high energy part of the spectrum at the expense of good agreement

in the low energy region.

Both the P_t balance and the $\Delta\eta$ plots show up best the disagreement between data and Lund parton shower models. In the P_t balance plot, the PS(Q^2) and PS($Q^2(1-x)$) models are more peaked in ϕ illustrating the lack of particles in the azimuthal region between scattered electron and struck quark. A scale which allows significantly more gluon radiation would show a flatter distribution over all ϕ as can be seen from the PS(W^2) result. Unfortunately, as mentioned earlier this latter choice of scale permits too much emission and grossly overestimates the data response.

Turning to the $\Delta\eta$ plot, the effect of the gluon phase space constriction imposed by the PS(Q^2) and PS($Q^2(1-x)$) scales is shown in the lack of a positive shift in the left hand peak of the $\Delta\eta$ plot. At low Q^2, the choice of these two scales to control gluon emission is effectively equivalent to a simple quark-parton model approach i.e. no gluon emission. The PS(W^2) distribution shows no evidence of the double-peak structure shown in the data as a result of increased gluon emission between the struck quark and the remnant filling the "trough" between the colour sources.

$10^{-3} < x < 10^{-2}$

As observed in figure 4.4, the majority of events in the medium x region occur near $x \approx 10^{-3}$. Hence the x dependent factor in equation (5.2) is still large implying that the W^2 scale still offers significantly more phase space for gluon emission that either the Q^2 or $Q^2(1-x)$ $\max(1, \ln 1/x)$ scales. The numerical factor multiplying Q^2 in this latter scale is still ≈ 5 in most cases but can to fall to ≈ 2 at the large x end of the bin. This "modified" Q^2 is the most successful of the three shown in figure 5.7 at predicting the response of the data. The patterns observed in the low x region are for the most part repeated in this medium x range. Of particular note is the modified Q^2 response in the $\Delta\eta$ plot. Here we see definite evidence that the peak representing the struck quark has shifted away from zero in a positive direction and that the distribution has broadened

compared to the normal PS(Q^2) response. However, none of the three models does any better in accurately reproducing the flow of energy exhibited by the data in this medium x range than they did at the low x range described earlier.

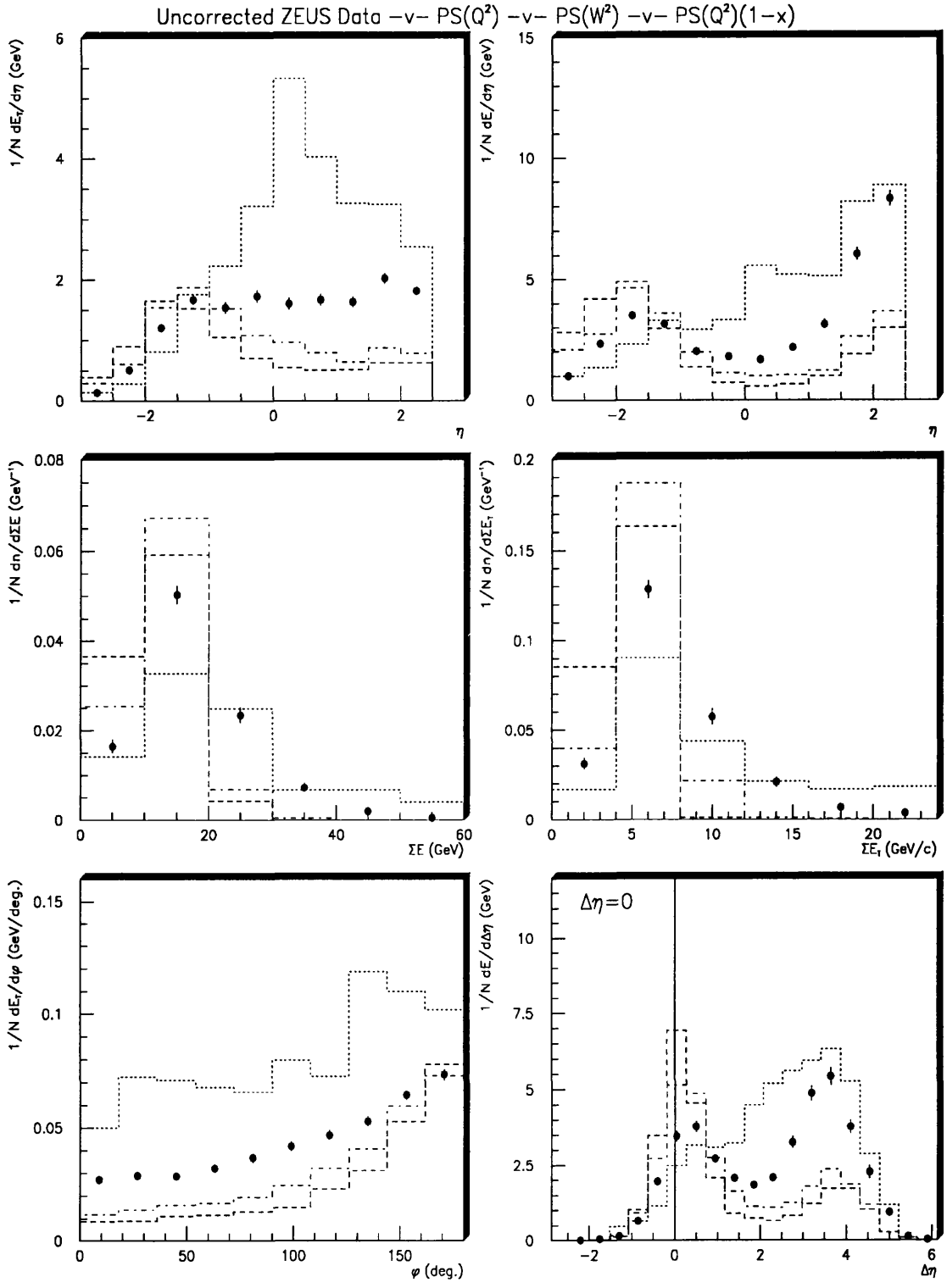

Figure 5.6: *The distributions for PS(Q^2) (dashed), PS(W^2) (dotted) and PS($Q^2(1-x)$) (dash-dotted) compared to uncorrected data for $x < 10^{-3}$.*

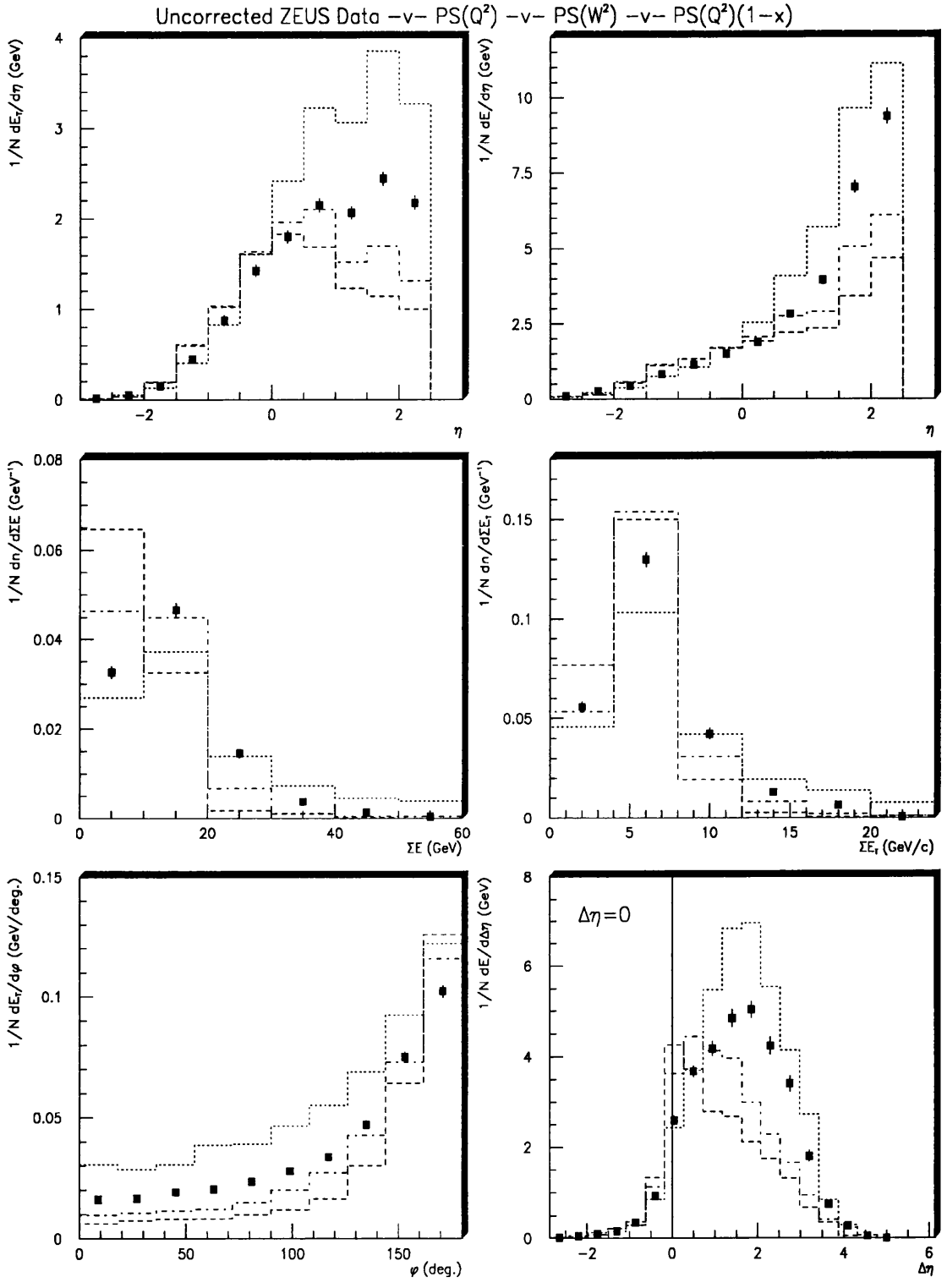

Figure 5.7: *The distributions for PS(Q^2) (dashed), PS(W^2) (dotted) and PS($Q^2(1-x)$) (dash-dotted) compared to uncorrected data for* $10^{-3} < x < 10^{-2}$.

5.7 The Colour Dipole Model

$x < 10^{-3}$

As can be observed in figure 5.8, the CDM model with and without the inclusion of a special boson-gluon fusion treatment shows reasonable agreement with data. The biggest problem area for the CDM model without BGF seems to be in the description of E_t-weighted plots where an excess E_t has been attributed to the parton emissions in the region $-1 < \eta < 1$ ($40^o < \theta < 140^o$). Inclusion of a BGF treatment appears to make a significant change to the pseudorapidity distributions but shows up less when summed energy and transverse energy distributions are studied. The model which does not include a BGF treatment must always contribute more E_t in an event compared to one which includes the treatment. Of the two $O(\alpha_s)$ processes available for Monte Carlo models, the QCD Compton (QCD-C) process involves emitting "harder" gluons than the BGF process because the latter splits its energy between two outgoing quarks whereas the former attributes energy to one gluon only. On a parton level, the created quarks in the BGF process individually carry less E_t than the lone gluon emitted in the QCD-C event. Hence the better agreement with data observed in the CDM+BGF polar distributions compared to the CDM by itself.

Figure 5.8 also shows that the CDM and CDM+BGF models overestimate the response of the data in the P_t balance plot. Again, the inclusion of a special BGF treatment seems to correctly modify the basic CDM prescription, bringing better agreement with observed data. Differences between the CDM and CDM+BGF models also show up well in the $\Delta\eta$ plot. Both models are in close agreement with each other except in the region $1 < \Delta\eta < 2$ where the addition of a BGF treatment is successful in bringing the Monte Carlo in line with the observed data. However, regardless of which CDM approach is taken, there is still a region of mismatch between the peaks.

$10^{-3} < x < 10^{-2}$

The probability for incurring $O(\alpha_s)$ processes decreases as x increases. Consequently, there will be less difference between the CDM and CDM+BGF approaches in the medium x region studied in figure 5.9. Overall, agreement with data for both models is still good with perhaps the biggest discrepancy occuring in the $\Delta\eta$ distributions. The two Monte Carlo models show the same premature drop at $\Delta\eta \approx 2$ seen in the ME+PS model, most certainly a another sign that a good understanding of modelling of the proton remnant has still be be achieved.

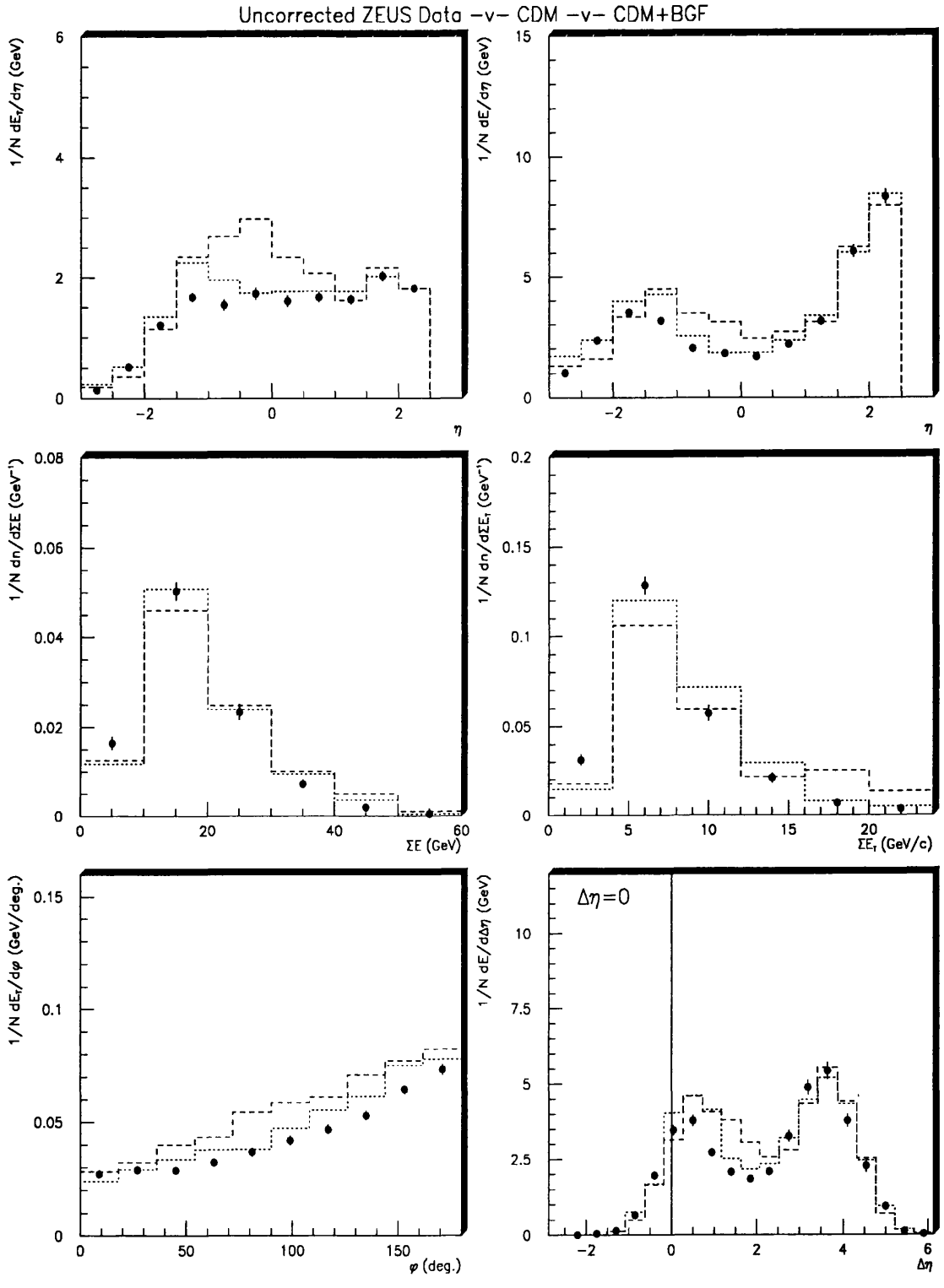

Figure 5.8: *The distributions for CDM (dashed) and CDM+BGF (dotted) compared to uncorrected data for* $x < 10^{-3}$.

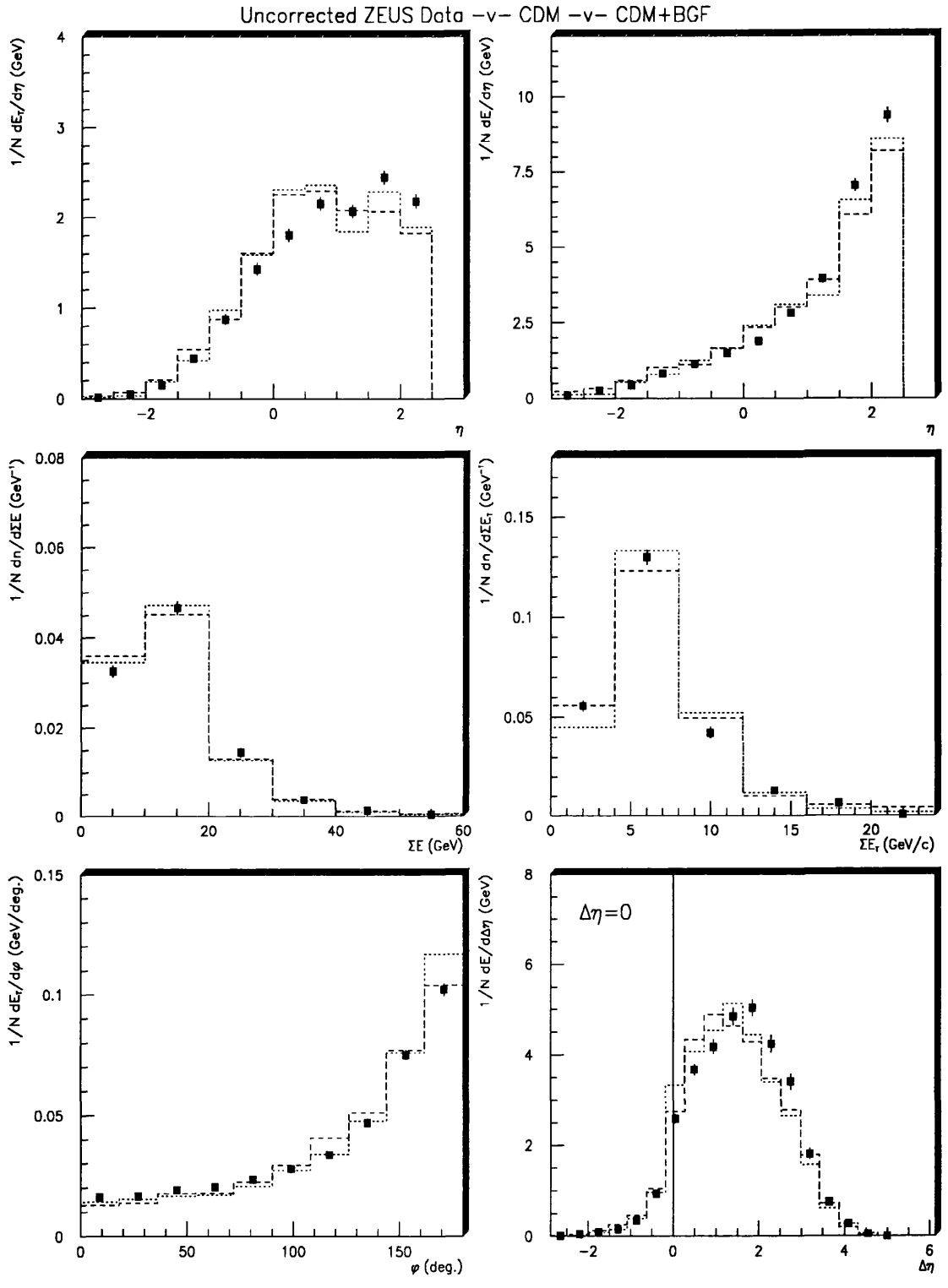

Figure 5.9: *The distributions for CDM (dashed) and CDM+BGF (dotted) compared to uncorrected data for* $10^{-3} < x < 10^{-2}$.

5.8 The HERWIG Parton Shower Model

$\underline{x < 10^{-3}}$

It is clear from figure 5.10 that in general HERWIG is capable of correctly predicting the overall shape of each angular distribution. The differences between model and data in the energy flow plots are on the whole small except for the very forward region ($\theta > 150^{o}$) where neither the inclusion or suppression of the soft underlying event treatment correctly predicts the response of the data.

However, figure 5.10 also shows that both the summed energy and summed transverse energy distributions do not really reproduce the observed data values, appearing to peak at too high values. Consequently, both distributions overstretch the data at values of $\sum E$ of 20 GeV but suppressing the soft underlying event seems to recover better agreement. This is indicative of the HERWIG model allowing too much phase space for gluon emission. Since this allowance is controlled by a function :

$$\text{virtuality scale} \propto E^2(1 - \cos\psi) \tag{5.3}$$

where E is the energy of the parton and ψ is its angle with respect to its colour connected partner, it may be that the branching process is attributing too much energy to emitted partons and/or their angle of emission is too low.

The P_t balance distribution for HERWIG without SUE (shown in figure 5.10) is a good representation of the data upto $\phi \approx 100^{o}$ but rises too quickly beyond this, reflecting the overestimation of energy and transverse energy in final state particles discussed earlier. The shape of the Monte Carlo model when it includes the SUE treatment is overall slightly better but is attributed too much E_t across the ϕ range.

In the $\Delta\eta$ plot, the positive shift indicating gluon emission is present and the general agreement between the models and data is good. The shape of the right hand remnant peak appears to be best modelled by HERWIG without the soft underlying event as including the process leads to an overestimation of the energy

in the remnant direction.

$10^{-3} < x < 10^{-2}$

Again, differences between the approaches which include and suppress the SUE (which are simply differences in the hadronization scheme) are reduced by moving to larger x values as illustrated in figure 5.11. While not allowing as much scope for distinguishing which approach best models the data, it is possible to observe that, as expected, the basic trends are the same. The large discrepancy between data and Monte Carlo in the forward region shown by both E_t and E weighted plots appears to be resolved by less active clustering approach, namely suppressing the soft underlying event. While all the plots show that the basic trend of the data is followed, it is clear that the two different cluster techniques employed are not entirely successful because the $\Delta\eta$ plot shows a marked difference between data and Monte Carlo in the region of the proton remnant. Suppressing the soft underlying event causes to little gluon emission in this region while including SUE allows too much.

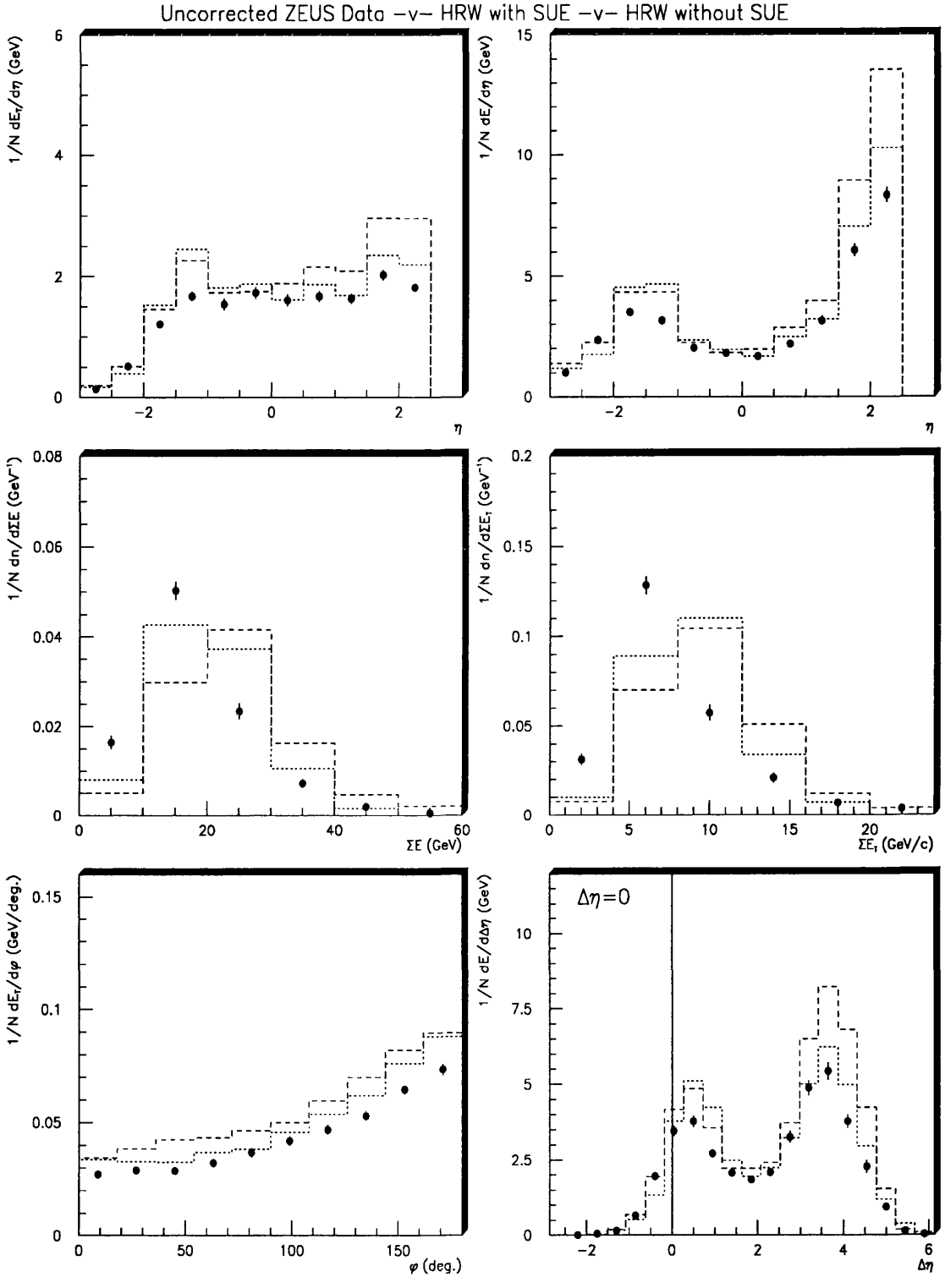

Figure 5.10: *The distributions for HERWIG with SUE (dashed) and HERWIG without SUE (dotted) compared to uncorrected data for* $x < 10^{-3}$.

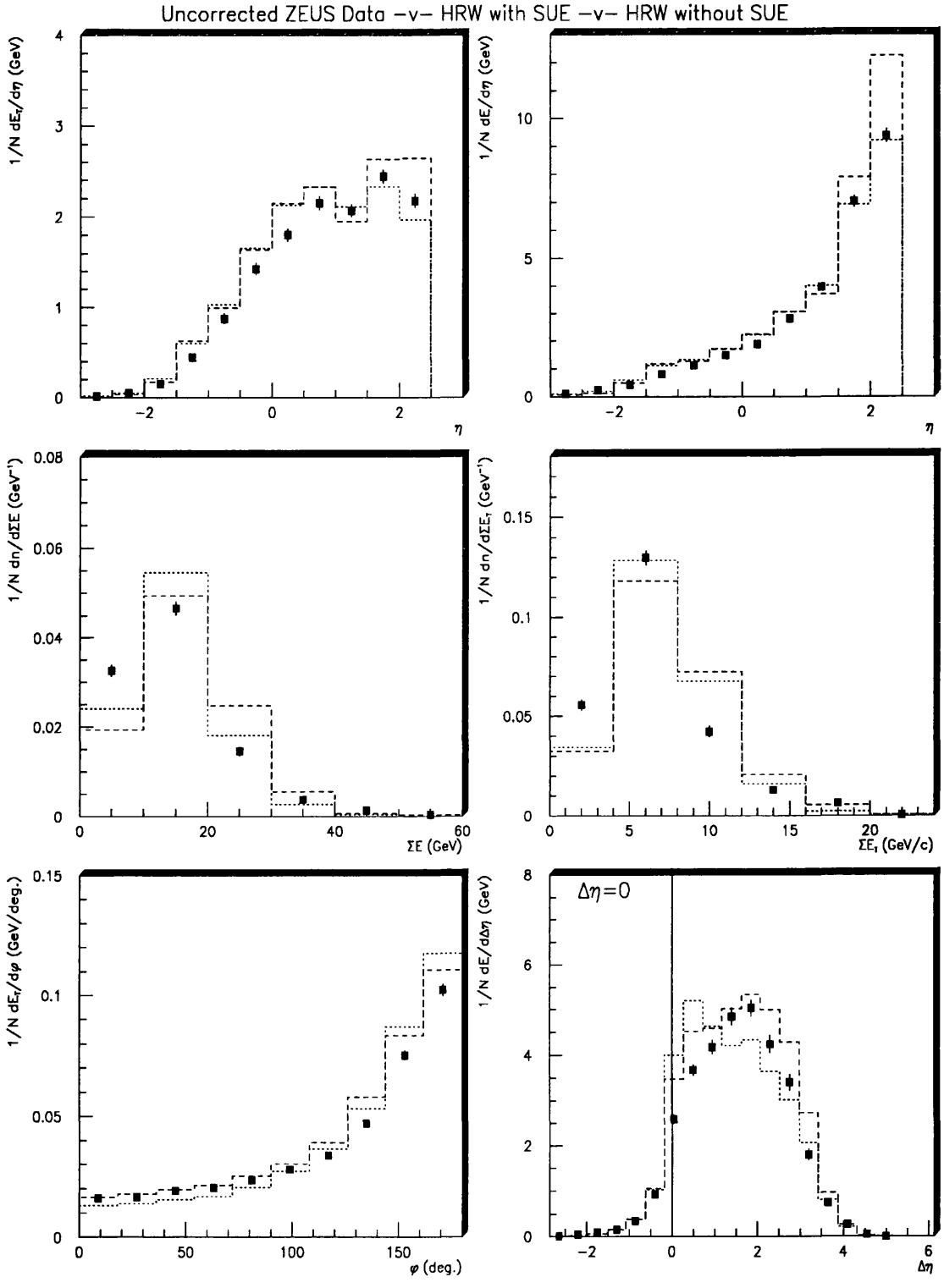

Figure 5.11: *The distributions for HERWIG with SUE (dashed) and HERWIG without SUE (dotted) compared to uncorrected data for* $10^{-3} < x < 10^{-2}$.

5.9 Summary of Model Comparison Results

Clearly the inclusion of final state gluon emission processes in the QCD cascade process is of vital importance in getting accurate reproduction of observed ZEUS data. Models which do not include this feature (ME) and those which include it but restrict its potential by using kinematic limits (PS(Q^2) and PS($Q^2(1-x)$)) do not represent the data with sufficient precision. However, as illustrated by the PS(W^2) scale, the story is not one of just permitting sufficient phase space for gluon emission. Rather, care must be taken to ensure that the available phase space is suitably restricted. The ME+PS representation, HERWIG with and without a soft underlying event treatment, and the colour dipole model represented by ARIADNE all appear to predict the shape of the observed distributions with a reasonable degree of accuracy given that no model parameter tuning has been performed in the analysis. It is clear that the treatment of the proton remnant within Monte Carlo models needs special care and will benefit from the work on this area which is to be carried out by both the ZEUS and H1 collaborations.

Table 5.1 contains the results of simple test designed to give a general quantitative measure of the agreement between uncorrected data and each of the Monte Carlo distributions. The values included in each are calculated from :

$$\text{Figure of Merit} = \frac{(\text{data point} - \text{MC point})^2}{(\sigma_{\text{data point}})^2 + (\sigma_{\text{MC point}})^2} \tag{5.4}$$

and are divided by the number of data points in the relevant plot.

5.10 Systematic Checks

This section seeks to determine whether the large discrepancies observed between some of the Monte Carlo data sets and the detector data can be attributed to various generator parameter settings. Note, this is not an attempt to "tune" Monte Carlo to data. Rather, it is simply a brief study to estimate whether or

Plot # $\Longrightarrow$ MC Model $\Downarrow$	1	2	3	4	5	6
$10^{-4} < x < 10^{-3}$ data sample						
ME	80	80	40	60	70	50
ME+PS	40	40	4	2	4	30
PS(Q^2)	150	140	70	100	130	90
PS(W^2)	270	230	50	50	500	110
PS($Q^2(1-x)$)	80	80	40	50	60	40
CDM	50	40	9	40	50	30
CDM+BGF	10	10	4	8	10	10
HRW+SUE	50	50	70	70	50	30
HRW+NO SUE	20	20	20	50	10	20
$10^{-3} < x < 10^{-2}$ data sample						
ME	30	40	50	20	70	50
ME+PS	30	30	4	4	7	10
PS(Q^2)	60	80	140	40	110	60
PS(W^2)	80	50	90	80	180	20
PS($Q^2(1-x)$)	30	30	30	10	30	30
CDM	10	10	2	20	7	8
CDM+BGF	9	9	1	8	6	7
HRW+SUE	10	20	30	30	10	10
HRW+NO SUE	10	10	20	30	10	30

Table 5.1: *A summary of the analysed data sets and their approximate agreement with the observed uncorrected data.*
The numbers refer to the distributions as follows : 1. E_t weighted η 2. E weighted η 3. $\sum E_i$ 4. $\sum E_{t_i}$ 5. E_t weighted $\Delta\phi$ 6. E weighted $\Delta\eta$

not some of the models can start to reproduce more accurately the observed data distributions.

In order to investigate the effect of changing Monte Carlo generator parameters on the shape of the investigated distributions, a number of systematic checks were carried out using Monte Carlo data samples. These involved comparing distributions for a number of different parameter settings to see if any significant deviation from the default distribution was discernible. The parameters investigated include structure function parametrizations, the addition of QED radiative corrections and various generator variables (see below for details). All

comparisons are carried out at the four-vector level and do not include the full calorimeter response. Each plot is restricted to cover the range $10^{-4} < x < 10^{-3}$ as disagreement between the data and the models is most apparent here.

5.10.1 Electron Identification

Following the description of the electron identification given the last chapter, two different algorithms ("Elect1" and "Eexotic") were compared.

The algorithms differ in the assignment of cuts controlling cone size, energy distributions and thresholds. The results of analysing the selected data sample and the PYTHIA photoproduction sample with each algorithm is shown in table 5.2 and figure 5.12. The results clearly show that as far as this analysis goes, the choice of electron finder is not of crucial importance. Although Eexotic would reduce the photoproduction background by a significant amount compared to Elect1, it also reduces the population of the low x bin by 30%. However, it does not change the conclusions drawn in section 5.9.

5.10.2 QED Corrections

The effect of adding initial state QED bremsstrahlung from the incoming electron on the global event distributions was investigated. The effect will be much the same for each Monte Carlo model. As an illustration, sample plots are shown for the case of the CDM with and without QED radiative corrections. As can be seen in figure 5.13, the QED radiative corrections for the CDM make little impact on the shape of the distributions with the exception of the region near the target remnant (right hand peak) on the $\Delta\eta$ plot where a small increase in response is observed. The shape of all the QED corrected distributions is, however, generally the same for each case. This pattern is repeated in the other Monte Carlo models and the conclusion is that QED corrections are not a major factor in determining these event shapes.

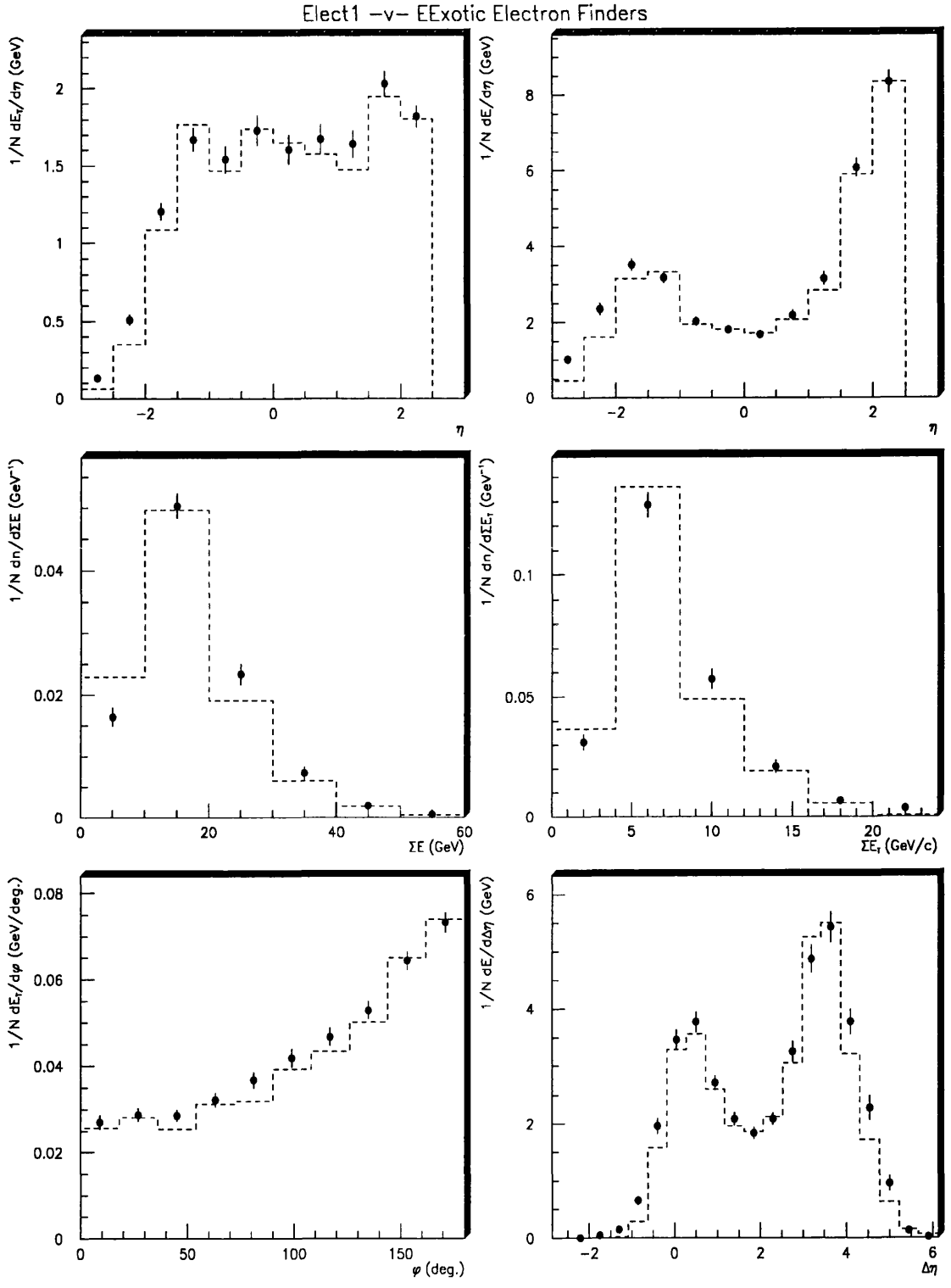

Figure 5.12: *The spectrum of distributions for uncorrected data analysed with "Elect1" (solid dots) and "Eexotic" (dashed line). Both representations illustrate the behaviour of the data.*

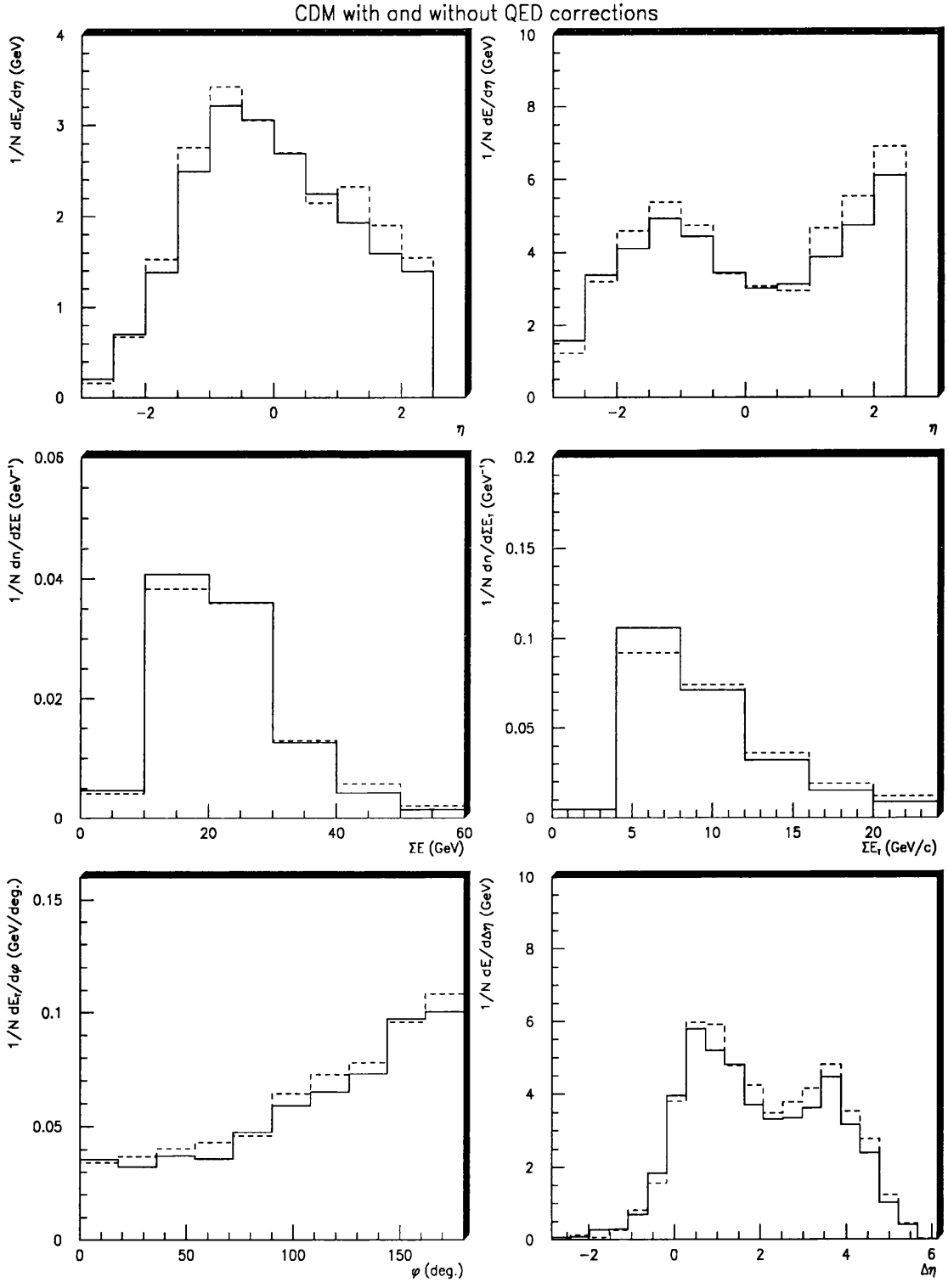

Figure 5.13: *The spectrum of distributions for the CDM without (solid) and with (dashed) QED corrections.*

Electron Identification Algorithm →	Elect1	Eexotic
Selected DIS data sample		
$10^{-5} < x < 10^{-3}$	632	445
$10^{-3} < x < 10^{-2}$	1200	1152
$10^{-2} < x < 1$	295	264
Total # events accepted	2127	1861
PYTHIA photoproduction sample		
Total # events accepted	11	3
$10^{-5} < x < 10^{-3}$	10	3
$10^{-3} < x < 10^{-2}$	1	0
$10^{-2} < x < 1$	0	0

Table 5.2: *Comparison of two separate electron finders acting on observed detector data and a PYTHIA photoproduction sample.*

5.10.3 Parton Density Parametrizations

An important consideration in the comparison of real ep data with Monte Carlo data is the choice of proton's parton density parametrization, or structure function. These functions control the distribution and activity of the proton's partonic constituents and a number of widely differing predictions have been made about their behaviour. To investigate the general response, the three Lund parton shower models were studied with two different (and extreme) choices of structure function set. With the recent publication of $F_2(x, Q^2)$ behaviour by ZEUS [59] and H1 [60], the MRS'D0 and MRS'D− parametrizations were studied along with those predicted by Morfin and Tung (MTB1 and MTB2) [62]. Figure 5.14 shows the comparison for the Lund PS model with W^2 virtuality scale (chosen because this allows maximum gluon emission and therefore will show any difference to maximum effect). It is clear that choice of structure function (even at the very low x range investigated here) is relatively unimportant in this analysis. While some of the

distributions do change noticeably, especially for the MRS'D− parametrization, it is not enough of a change to change the conclusions drawn in section 5.9. A similar pattern is seen for the other two Lund PS approaches so it is deemed not to be an overriding factor in these global event distributions at low x.

5.10.4 FCAL Energy Cutoff

It was noted that removing the FCAL energy cut of 1 GeV had little significant effect on the data (on average 1% more events were accepted) and all the Monte Carlo models bar one - namely HERWIG without the inclusion of the soft underlying event which passed about 11% more events. For those models which were effectively unchanged by the cut, their global distributions remained unchanged within error. However, the HERWIG model without the SUE option showed significant changes in the global event shape variables.

The effect of the cut is seen quite clearly in figure 5.15. When the cut is ignored, there is naturally a larger number of events accepted. However, these extra events contribute little to the transverse/total energy of the sample overall, so in general the E and E_t weighted pseudorapidity distributions lie below those which include the cut. The total energy/transverse energy plots illustrate how little energy the extra events contribute by the increased population of the low E and E_t bins. The energy-weighted $\Delta\eta$ plot shows the most striking change as the influence of the target remnant at large $\Delta\eta$ is reduced (the events contribute less energy) and the struck quark peak shifts to lie at $\Delta\eta \sim 0$ indicating that the events contain little significant gluon radiation.

As can be seen in figure 5.16, the multi-cluster nature of a HERWIG event which includes the soft underlying event will fill in the region between the struck quark and the remnant while an event without the SUE treatment will show a depletion in the same region but only in events which have little or no gluon radiation. For low energy events, the $E_{FCAL} < 1$ GeV will remove the events with no SUE treatment while keeping those with the multi-cluster nature.

The typical event structure for a HERWIG event without SUE which failed

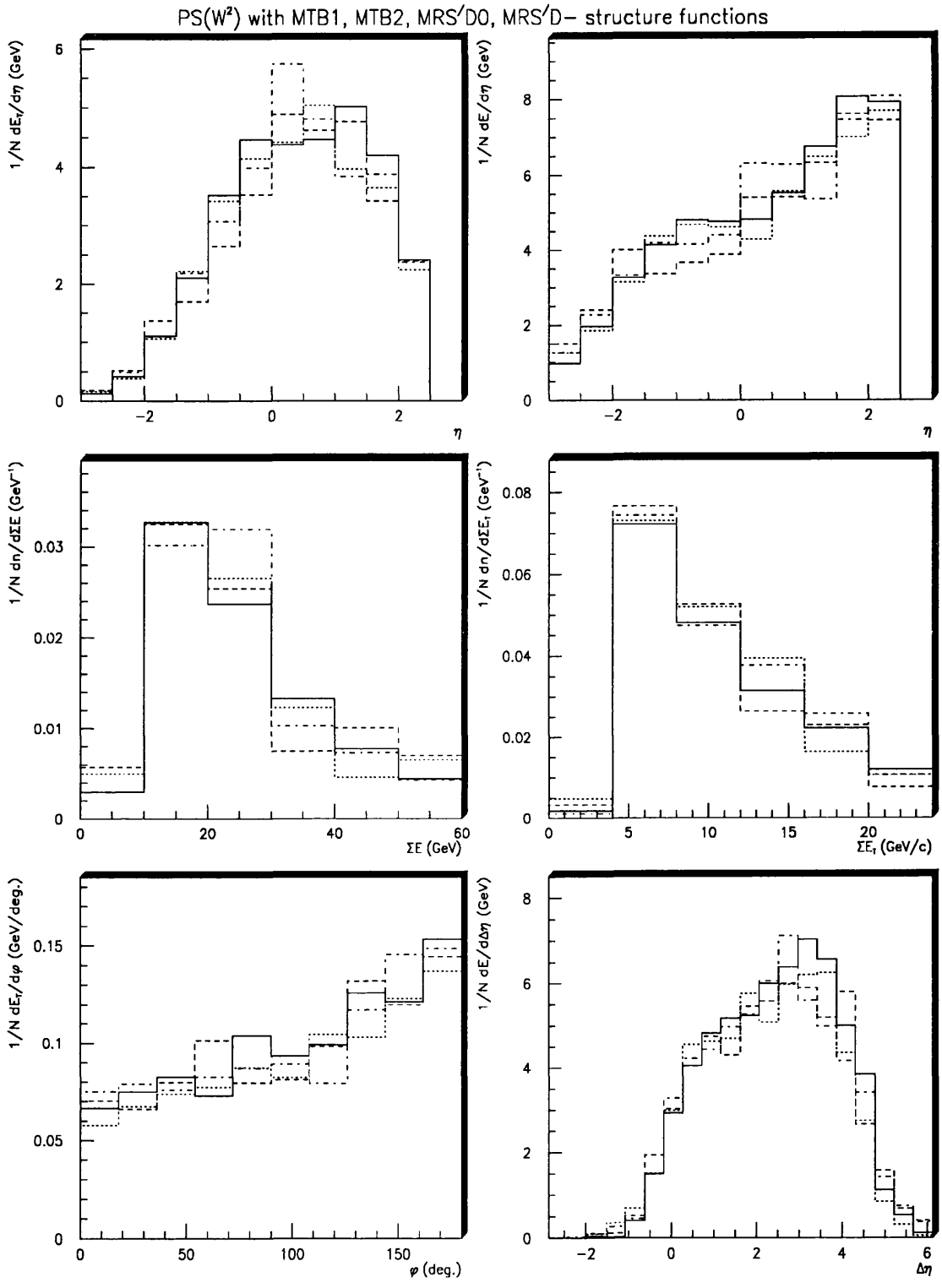

Figure 5.14: *The spectrum of distributions for PS(W^2) with MTB1 (solid), MTB2 (dashed),* MRS'D0 *(dotted) and* MRS'D− *(dash-dotted) structure function sets.*

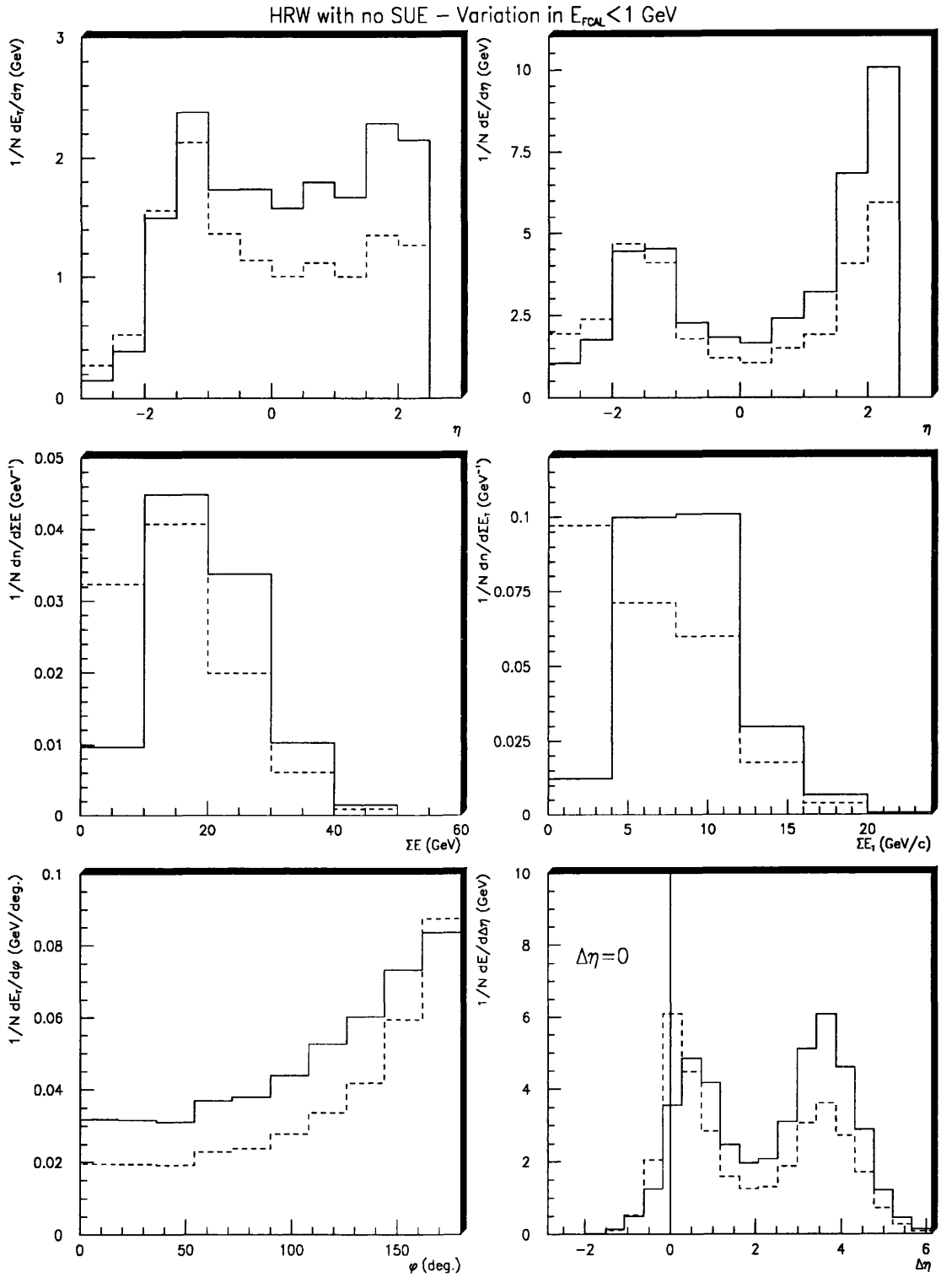

Figure 5.15: *The spectrum of distributions for HERWIG with no SUE when the* $E_{FCAL} < 1$ *GeV cut is included (solid) and excluded (dashed).*

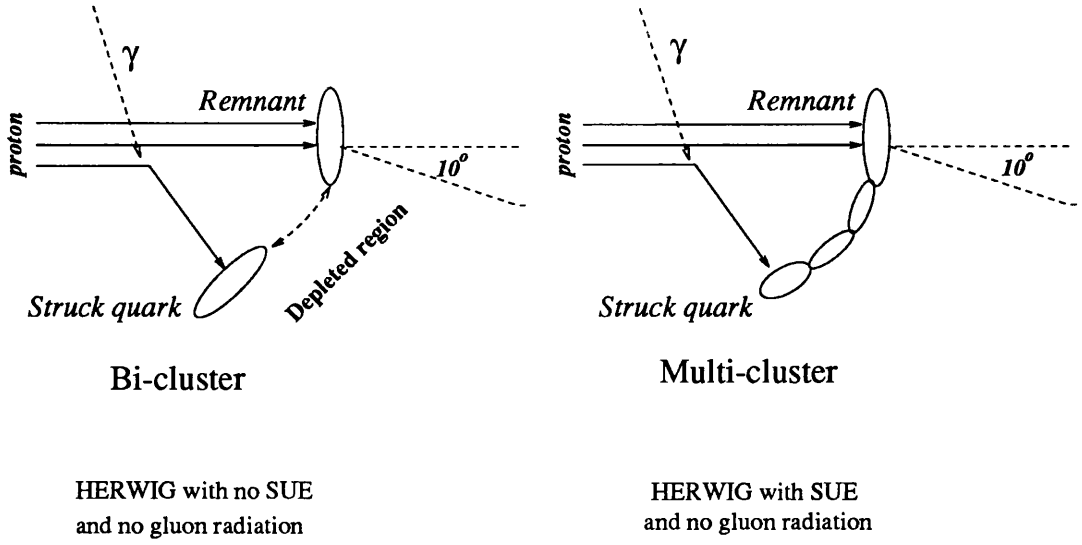

Figure 5.16: *Schematic of a HERWIG event with and without the soft underlying event treatment.*

the $E_{FCAL} < 1$ GeV cut is shown in figure 5.17. A similar event, this time from HERWIG with SUE and which passed the cut is shown in figure 5.18. Both events have similar kinematic cuts. As can be seen from the FCAL energy diagrams beside the event display, the event which passed the cut has a much larger spread of particles in the FCAL region around the beampipe compared to the event which failed the cut. This is attributable to the clustering method - the event which passed had the SUE treatment included, meaning a multi-cluster final state. The event which failed had the SUE suppressed meaning a bi-cluster state. In this latter state, the cluster which forms the remnant has totally disappeared into the beampipe or 10^o cut region. The remaining cluster goes to form the struck quark which in this low x region appears in the BCAL. There are no clusters formed between the remnant and the struck quark to produce energy in the FCAL.

5.10.5 LEPTO Model Parameters

It is possible within Monte Carlo programs to alter parameter values. In a lot of cases, the default parameter settings are educated estimates or have been

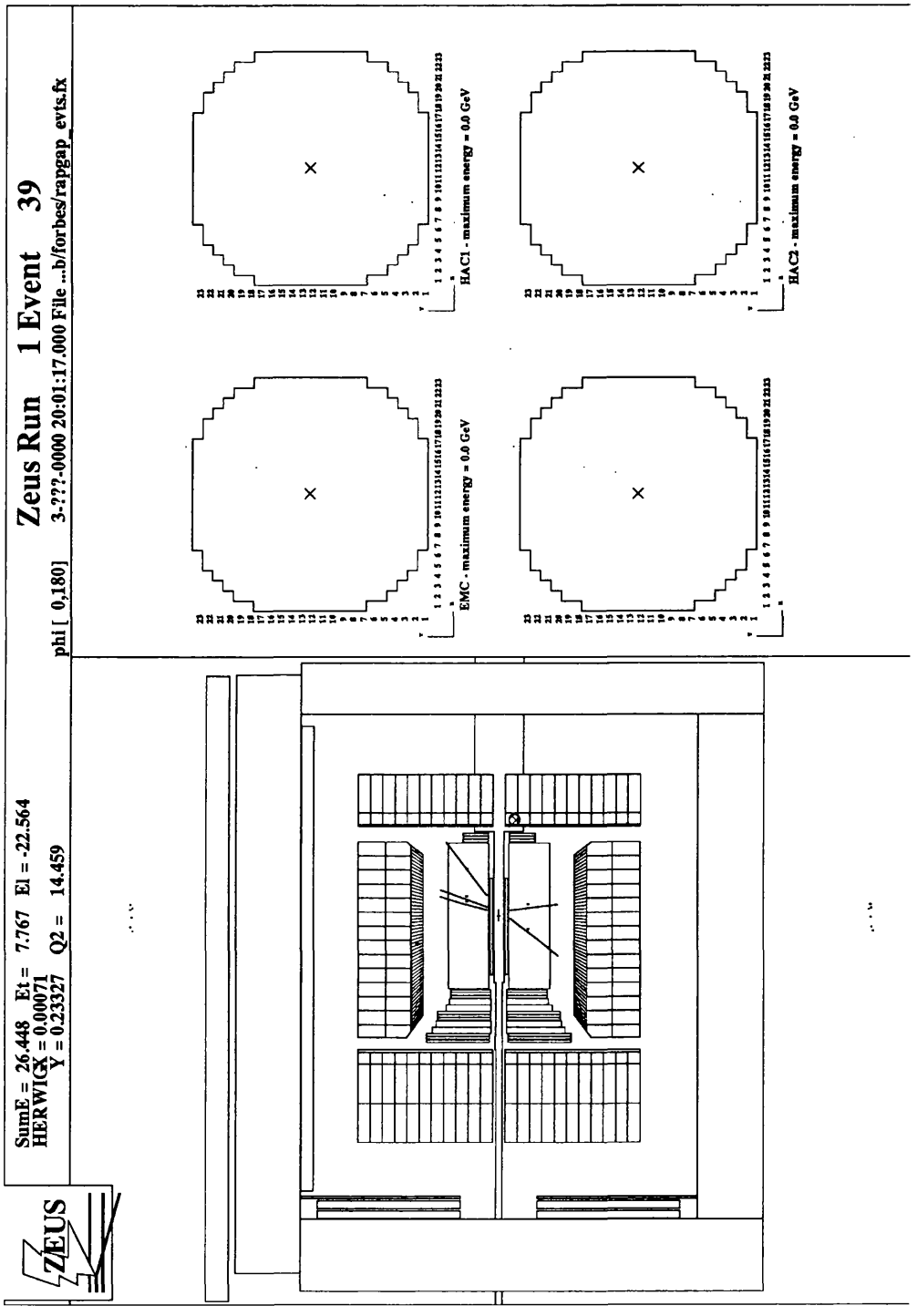

Figure 5.17: *A HERWIG event without SUE which failed the* $E_{FCAL} < 1$ *GeV cut.*

The kinematics are $x = 0.00071$, $y = 0.23327$ *and* $Q^2 = 14\ GeV^2$.

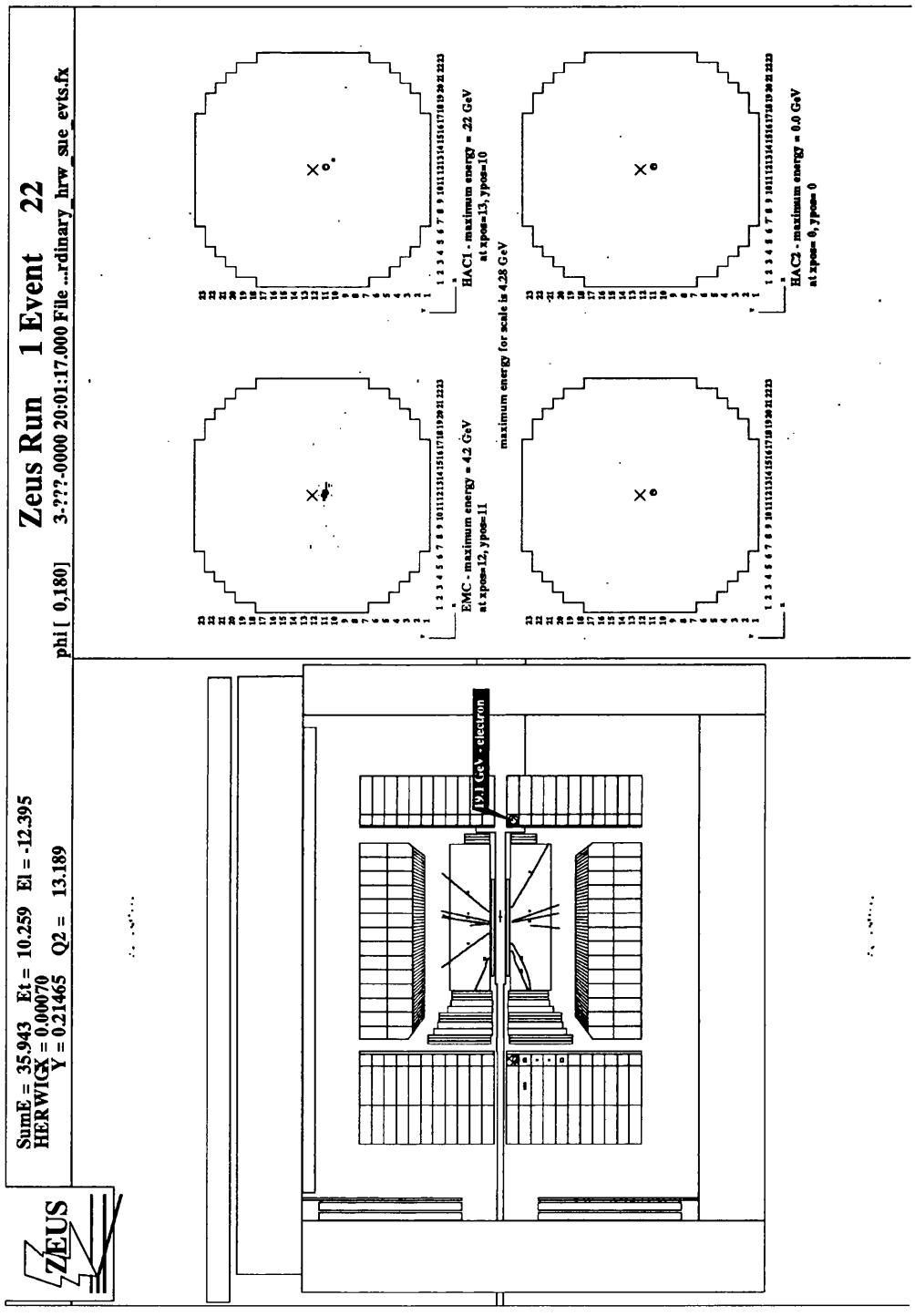

Figure 5.18: *A HERWIG event with SUE which passed the* $E_{FCAL} < 1$ *GeV cut. The kinematics are* $x = 0.00070$, $y = 0.21465$ *and* $Q^2 = 13$ GeV^2.

reached by "tuning" Monte Carlo to fit observed data. It is important therefore to investigate how each model is affected by changing some of these parameters.

5.10.6 Matrix Element Divergence Cutoffs y_{cut} and m_{ij}

As has been discussed earlier, matrix element calculations are divergent in the limit when the gluon energy or the opening angle between partons vanishes. For practical Monte Carlo simulations as performed in LEPTO, it is necessary to impose a cutoff to avoid the singular regions of the matrix elements. This is done by requiring a minimum invariant mass m_{ij} between any pair of partons in the final state, including the remnant system. This cutoff is implemented by the requirement that $m_{ij}^2 > y_{cut}W^2$ where the value of y_{cut} is chosen to be as small as possible in order to include as much of the phase space space as possible while still avoiding the divergence. Thus, it is possible within LEPTO to vary both m_{ij} and y_{cut} to investigate their effect.

For y_{cut}, which has a default value of 0.015, the extreme low value studied was 0.0001 and the upper value was 0.025. m_{ij} was varied between 0.5 GeV and 2.5 GeV from a default value of 2 GeV. It should be noted that y_{cut} is the dominant cut at large energies (large W) and m_{ij} dominates at low energies. Figure 5.19 shows the response of the ME model and illustrates the effect of changing y_{cut}. A considerable decrease in y_{cut} compared to the default value results in a considerable increase in hadronic activity. This is understandable given that a low y_{cut} permits closer approach to ME singularities. The consequent higher gluon emission cross sections in first order processes results in greater gluon activity. When the hadronization stage is reached, the increased number of gluons manifests itself in an increased multiplicity of hadrons. However, while appearing to make the ME model agree better (qualitatively) with the observed data, it should be noted that there is still no shift in the left hand peak of the $\Delta\eta$ plot to match the shift in the observed data. The effect on the distributions of changing m_{ij} was negligible and so the distributions are not shown.

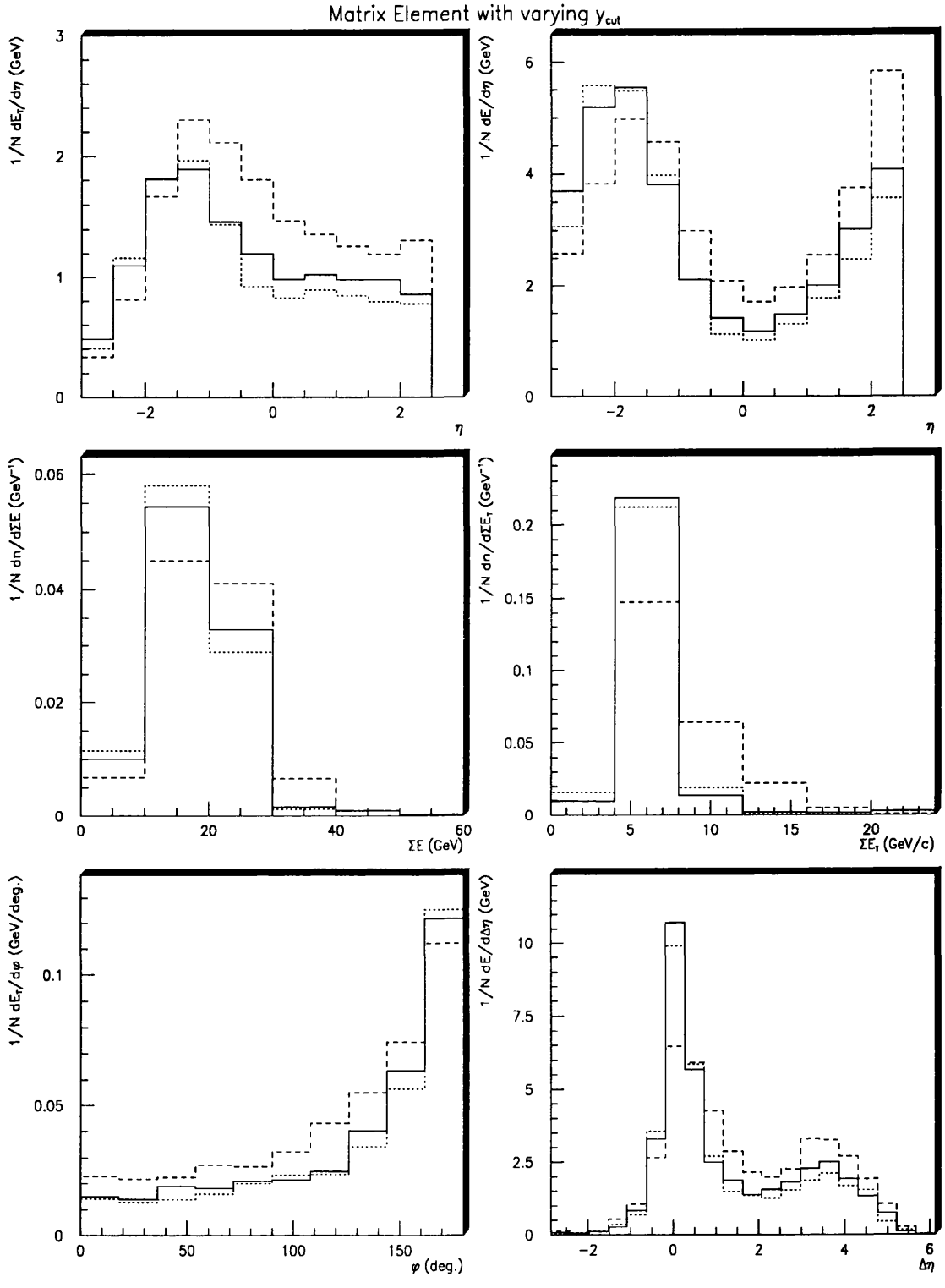

Figure 5.19: *The spectrum of distributions for y_{cut} of 0.015 (solid), 0.0001 (dashed) and 0.025 (dotted) in the ME model.*

5.10.7 Minimum Virtuality Cutoffs

In both initial and final state QCD showers, it is possible to control the values at which partons emitted in a shower are no longer allowed to branch. Investigation revealed that there is no significant effect on the shape of the distributions when these parameters are adjusted, hence the distributions are not shown. The pattern is similar for the Lund PS model with Q^2 and $Q^2(1-x)\max(1, \ln\frac{1}{x})$ virtuality scales.

5.10.8 Primordial k_T

This parameter controls the width of the Gaussian distribution for the primordial transverse momentum k_t of partons in the nucleon. The default value is 0.44 GeV and checks were carried out for ME, PS(Q^2), PS($Q^2(1-x)$) and PS(W^2) models with QED corrections to see if they could be brought more into line with the observed data. The extreme values used in this test were 0.0 GeV and 1.0 GeV. Again, there is no significant deviation from the default distributions when the parameter is varied and hence no plots are shown. This conclusion does not change when the other two Lund PS virtuality scales are investigated.

5.10.9 QCD Scale Parameter Λ in IS and FS Radiation

The value of Λ_{QCD} in initial and final state shower production was varied by factors of 4 in both directions for PS and ME models. The results show that the distributions are virtually insensitive to changes in these parameters. No significant difference was observed for the other virtuality scales examined either. Again, plots are not shown.

5.10.10 String Parameters : a, b, σ_q

It is to be expected that even relatively small changes in the parameters controlling the Lund fragmentation function (see equation (1.26) in section 1.12)

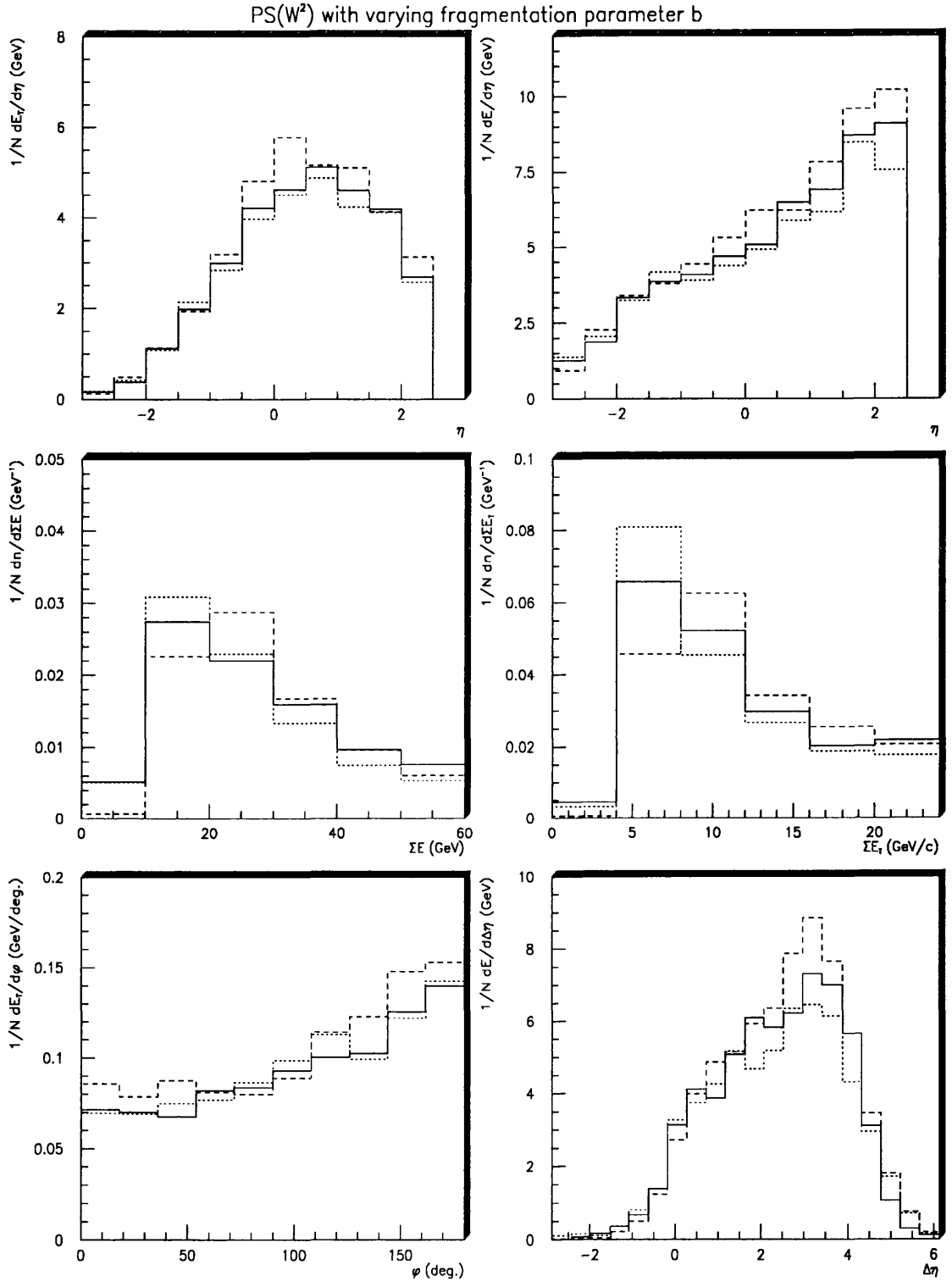

Figure 5.20: *The spectrum of distributions for* $b = 0.9\ GeV^{-2}$ *(solid),* $b = 0.2\ GeV^{-2}$ *(dashed) and* $b = 1.8\ GeV^{-2}$ *(dotted) in the PS(W^2) approach.*

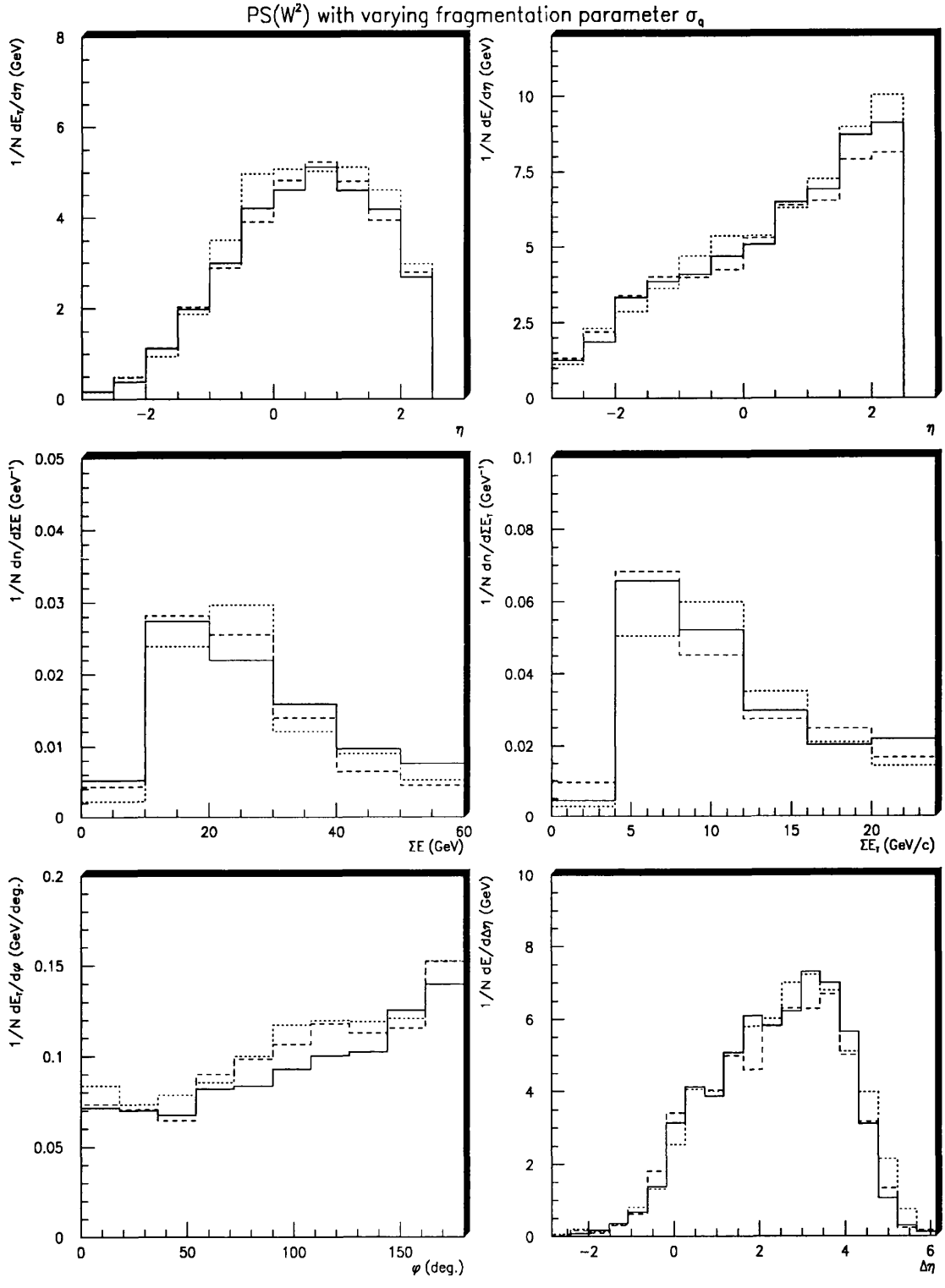

Figure 5.21: *The spectrum of distributions for* $\sigma_q = 0.35$ *GeV (solid),* $\sigma_q = 0.1$ *GeV (dashed), and* $\sigma_q = 1.0$ *GeV (dotted) in the PS(W^2) approach.*

will result in quite significant changes in the shape of global distributions. Investigation of the three PS models and the ME model reveals that no real change is seen when a is varied so the distributions for this parameter are not displayed. Conversely, figures 5.20 and 5.21 show significant deviations from the respective default distributions when b and σ are varied. These plots suggest that by decreasing the magnitude of b and increasing that of σ_q, an appreciable increase in the energy and transverse energy of produced hadrons is obtainable. There is still no net shift in the position of the left hand peak in the $\Delta\eta$ which would bring the distribution more in line with observed data. In addition, neither set of p_t balance plots shows the broadness associated with the observed data. The changes are not, however, sufficient to change the conclusions drawn earlier.

5.11 Summary of Systematic Checks

A series of systematic checks has been performed on some of the models which showed less than good agreement with the observed data. It has been found that changing some of the Monte Carlo parameters (see table 5.3) makes little difference to the overall shape of the distributions presented. Others have a more significant effect but still not enough to bring the Lund PS models and ME models into line with the data.

The most significant areas of interest involve the HERWIG model. Although in its basic form, HERWIG, with or without a soft underlying event treatment, generally shows good agreement with data, it has been found that there is one point to which it is particularly sensitive. The application of a cut, $E_{FCAL} < 1$ GeV, has a significant impact on the acceptance of HERWIG data which suppresses the soft underlying event ("HRW without SUE"). The same cut has only a negligible effect on the other Monte Carlo models, including the other HERWIG approach which does not suppress the soft underlying event ("HRW with SUE"). The behaviour exhibited by HERWIG in the two forms studied here is indicative that the choice of hadronization scheme for this model (ie. with or without SUE)

is particularly important. This study reveals that the model which suppresses the SUE is biased by the cut on $E_{FCAL} > 1$ GeV, an effect not reproduced by the observed data.

Parameter Investigated	MC Array Element	Default Value	Values Investigated	MC Model
y_{cut}	PARL(8)	0.015 GeV	0.0001 - 0.025 GeV	ME
m_{ij}	PARL(9)	2.0 GeV	0.5 - 2.5 GeV	ME
k_t	PARL(3)	0.44 GeV	0.0 - 1.0 GeV	ME, All PS
a	PARJ(41)	0.5	0.25 - 1.5	ME, All PS
b	PARJ(42)	0.9 GeV^{-2}	0.2 - 1.8 GeV^{-2}	ME, All PS
σ_q	PARJ(21)	0.35 GeV	0.1 - 1.0 GeV	ME, All PS
ISR Q^2_{min}	PYPAR(22)	1 GeV^2	0.25 - 4.0 GeV^2	All PS
FSR m_{min}	PARJ(82)	1 GeV	0.25 - 4.0 GeV	All PS
ISR Λ_{QCD}	PYPAR(21)	0.25 GeV	0.08 - 1.0 GeV	All PS
FSR Λ_{QCD}	PARJ(81)	0.40 GeV	0.1 - 1.6 GeV	All PS

Table 5.3: *A summary of the investigated Monte Carlo parameters.*

5.12 Correcting the ZEUS Data

All of the analysis so far has used raw ZEUS data and was compared to Monte Carlo data which had been passed through the ZEUS detector simulation. In order to assist future "tuning" of Monte Carlo models, the detector data has been corrected using simple histogram bin-to-bin corrections. The production of correction factors involves comparing the Monte Carlo four-vector data (from the "FMCKin" table) with Monte Carlo calorimeter data (from the "Caltru" table) and calculating correction factors as ratios for each bin in each distribution [63] :

$$\frac{(\mathrm{d}n/\mathrm{d}x)_{true}}{N_{true}} = \underbrace{\frac{\frac{(\mathrm{d}n/\mathrm{d}x)_{generator}}{N_{gen}}}{\frac{(\mathrm{d}n/\mathrm{d}x)_{MC\ detected}}{N_{MC}}}}_{Correction\ factor} \frac{(\mathrm{d}n/\mathrm{d}x)_{observed}}{N_{obs}} \tag{5.5}$$

where

- $(\mathrm{d}n/\mathrm{d}x)_{true}$ is the true distribution;
- $(\mathrm{d}n/\mathrm{d}x)_{generator}$ is the is the original distribution as generated in the Monte Carlo (called "four-vector" or "FMCKin" data);
- $(\mathrm{d}n/\mathrm{d}x)_{MC\ detected}$ is the distribution generated in the Monte Carlo and subjected to all experimental effects (called "calorimeter", "accepted" or "Caltru" data);
- $(\mathrm{d}n/\mathrm{d}x)_{observed}$ is the directly measured distribution.

The correction factors are then stored in a file and read in when detector data analysis was performed. This method is an attempt to make the detector data distributions independent of the ZEUS machine, so enabling detailed "tuning" of the Monte Carlo data to be made at a later date. A sample of results showing the four-vector and calorimeter distributions for a sample of CDM Monte Carlo is shown in figure 5.22. In general and as expected, the Caltru calorimeter information lies lower than the original four-vector information giving rise to it because there is a loss of information going from the latter to the

former. The calorimeter's finite resolution, cracks, and dead material are all contributing factors in this loss. However, there is an increase in the calorimeter's response compared to the four-vector data when the extreme forward direction is considered, suggesting that the 10° cut in θ in the forward direction is just on the boundary of reducing the influence of the remnant.

Various effects, including calorimeter cell energy cutoffs and histogram bin sizes (resolution effects) result in the correction factors obtained using the scheme outlined in equation (5.5) being dependent on the Monte Carlo model used to produce them.

To check some of these effects, three independent Monte Carlo data sets were used to generate separate correction factors and the distributions compared. The three Monte Carlo programs used invoked the CDM, ME+PS and HERWIG approaches respectively.

As can be seen in figure 5.23 which compares corrections obtained from these models, the differences between the independent sets of correction factors are not negligible, even for schemes such as ME+PS and CDM which only differ in their QCD cascade processes. This suggests that to accurately calculate the correction factors in a non-biased way involves using several different Monte Carlo models.

The energy resolution has been estimated from the previous energy-energy correlation plots at about 5 GeV in the low x bin and medium x bins. The resolution in η is estimated as ≈ 0.25 [64]. Erring on the side of caution, bin widths for the total energy and transverse energy plots are 10 GeV and 4 GeV respectively, while those for the η and $\Delta\eta$ plots are 0.5 and 0.45 respectively.

The set of correction factors used to correct the ZEUS data in this analysis derives from equal contributions of CDM, ME+PS and HERWIG data and a systematic error σ_{MC} is added to the data distributions to account for the variations between models. The source of this error is shown graphically in figure 5.24. As can be seen in figure 5.25, the errors on certain bins of the total energy, total transverse energy and $\Delta\eta$ distributions are very large ($> 50\%$). These correspond to bins whose contents are statistically low and so it is not

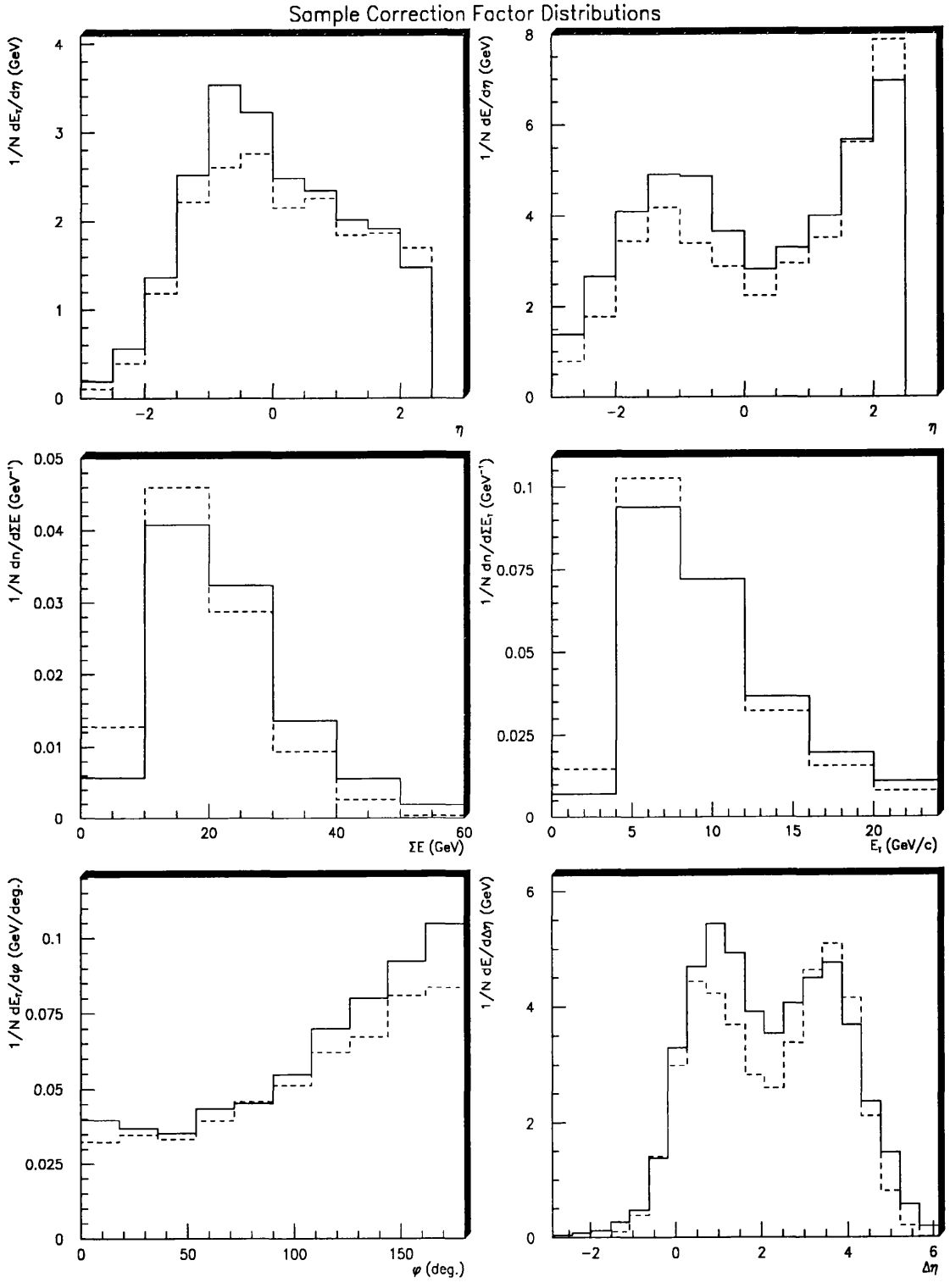

Figure 5.22: *Four-vector (solid) and calorimeter distributions (dashed) for the low x bin* $10^{-4} < x < 10^{-3}$.

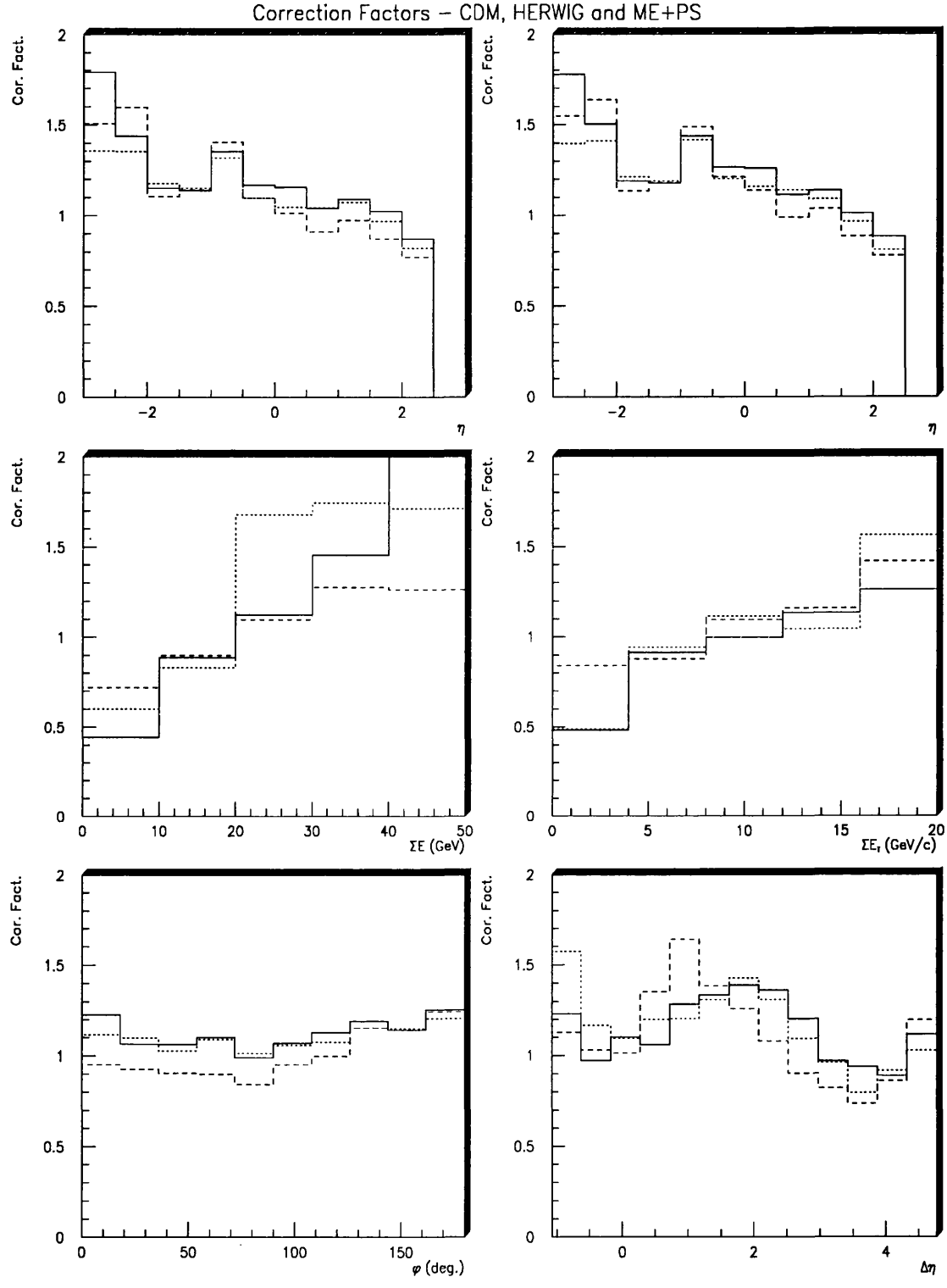

Figure 5.23: *A comparison of the correction factors for the CDM (solid), HERWIG (dashed) and ME+PS dotted) model.*

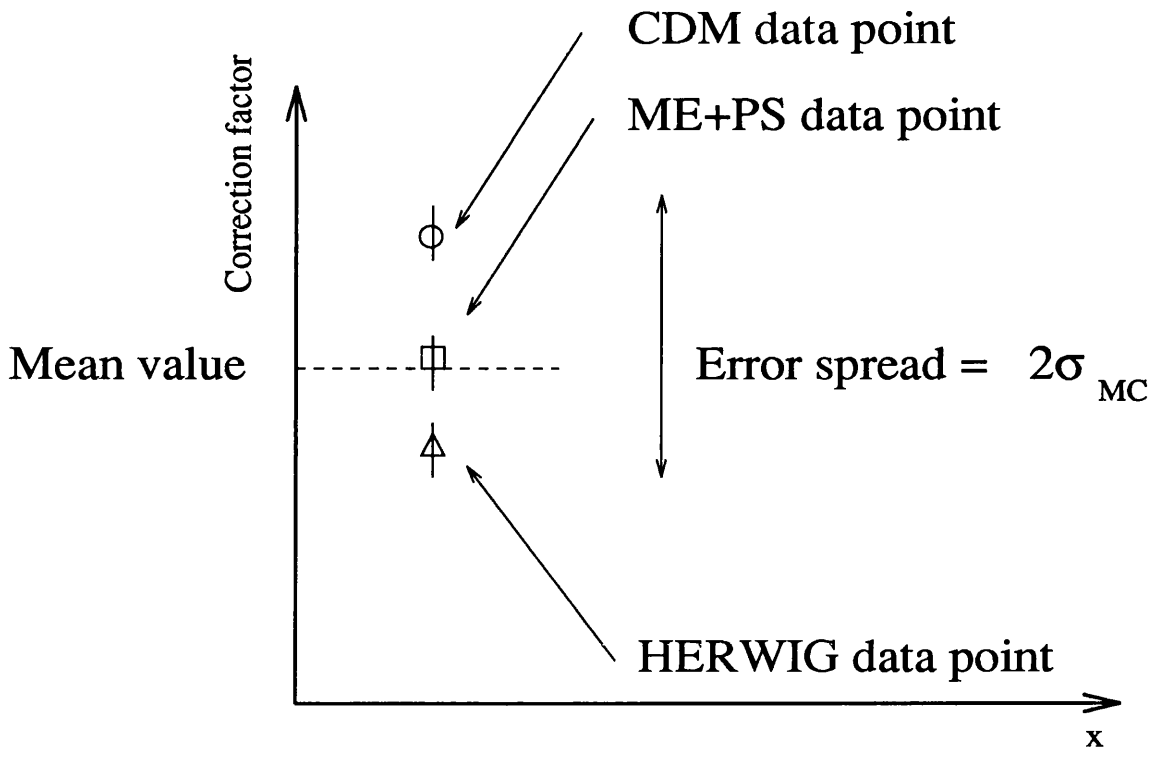

Figure 5.24: *The method of determining the systematic error due to the choice of Monte Carlo model.*

meaningful to correct the data in these areas.

5.13 Comparing Corrected and Uncorrected Data

The effect of the correction factors on the data is shown in figures 5.27 and 5.28. The large systematic errors attributable to differences between Monte Carlo models reduce the effect of the corrections quite considerably in certain areas but on the whole, obvious trends are visible - for example in the pseudorapidity distributions where there is evidence of a reduction in energy in the very forward direction together with an increase of it in the rear direction.

In both figures, the total transverse and full energy plots lack some corrected data points at the extreme end of the spectrum. As mentioned earlier, this is

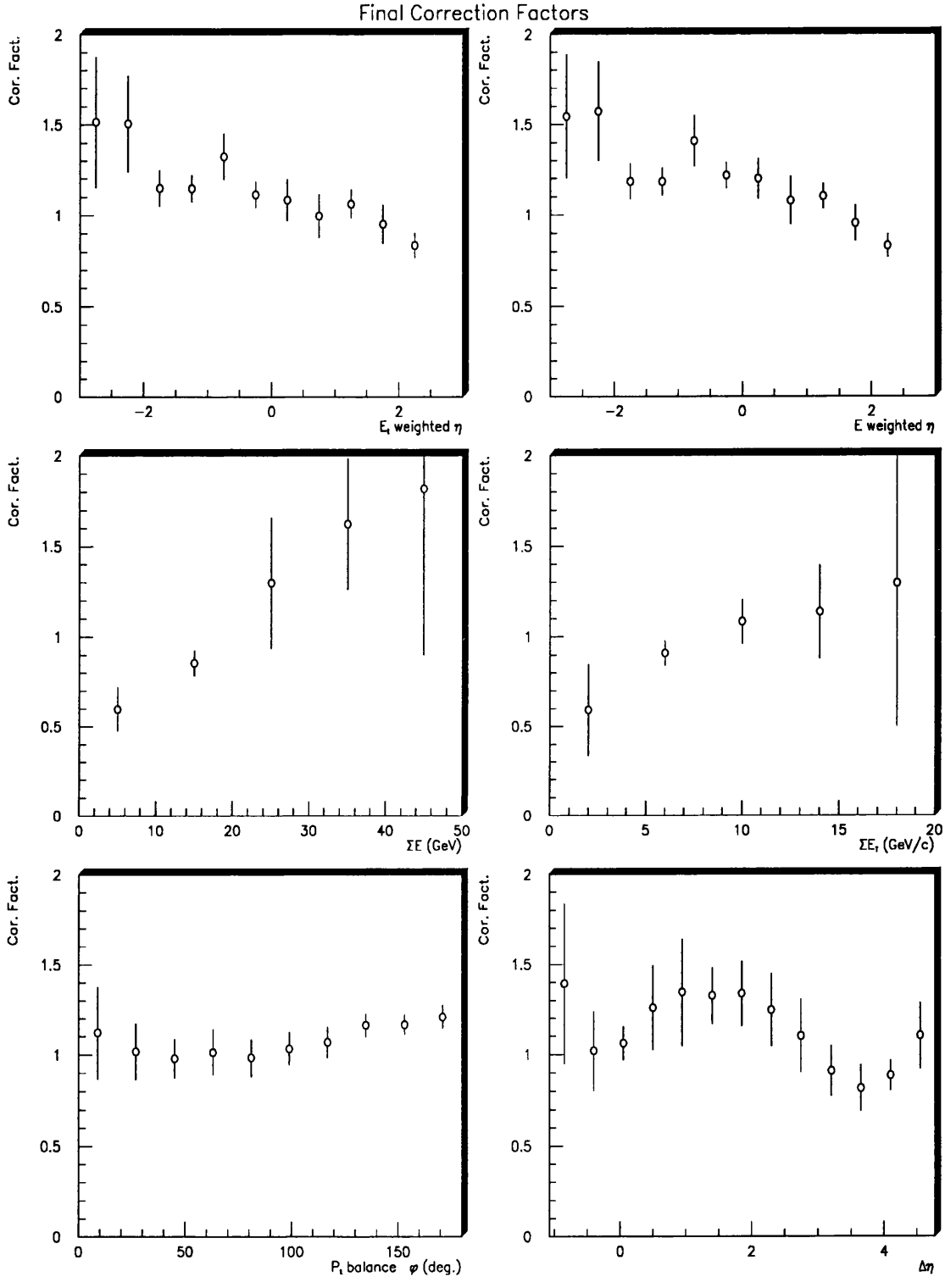

Figure 5.25: *The overall correction factors used in this analysis in the region* $x < 10^{-3}$.

The error bars represent the systematic errors σ_{MC} *due to different Monte Carlo models.*

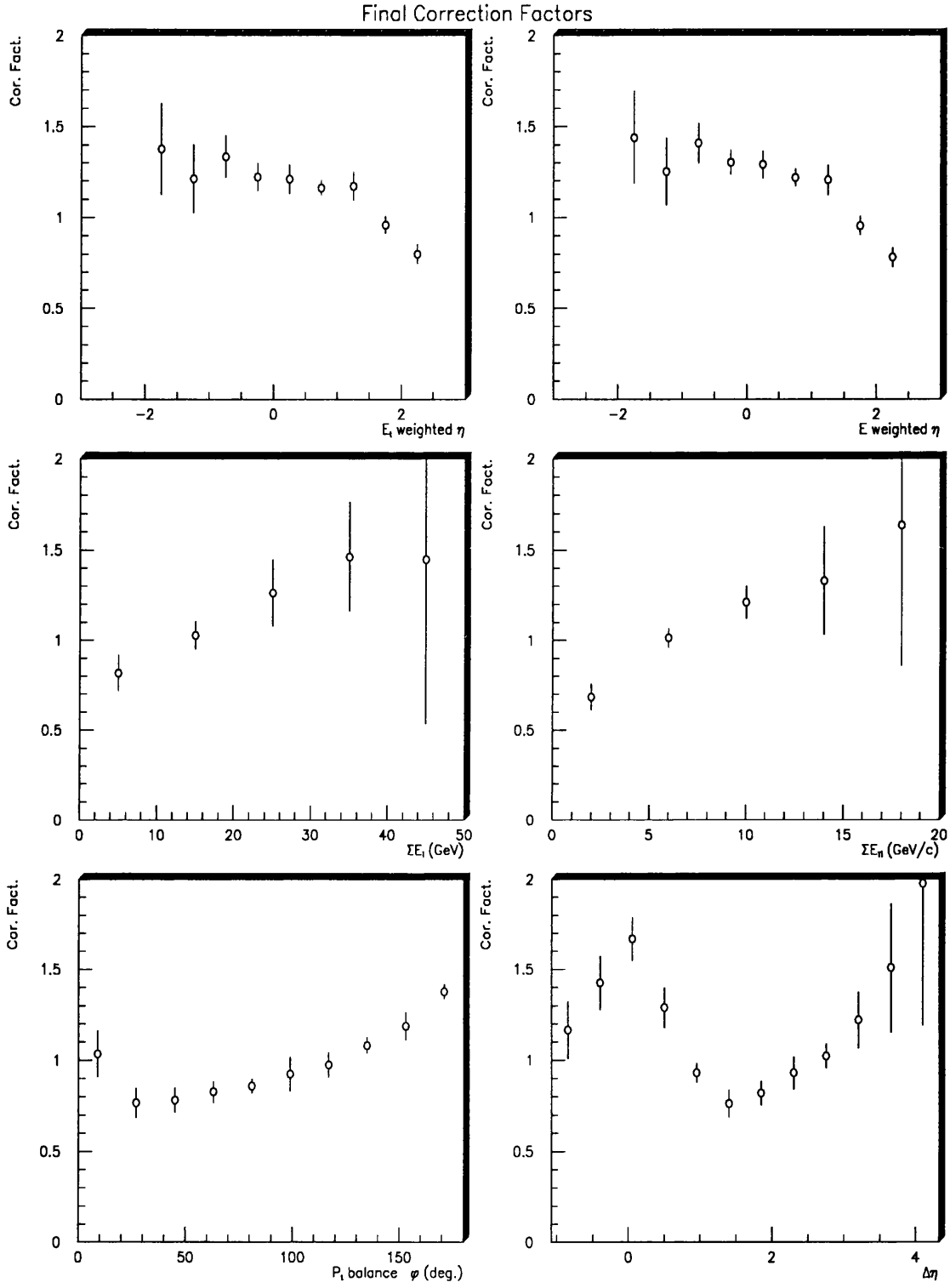

Figure 5.26: *The overall correction factors used in this analysis for the region* $10^{-3} < x < 10^{-2}$.

The error bars represent the systematic errors σ_{MC} *due to different Monte Carlo models.*

because correction factors in this region possessed very large errors rendering correction meaningless. The entries in these bins were set to zero. In both of the x regions displayed here, there is a decrease in mean energy/transverse energy per event together with a "boost" in higher energy bins, reflecting the more even spread in energy across the detector seen in the pseudorapidity distributions.

In the low x region, both gluon emission plots show interesting features after correction. The P_t balance plot now rises more sharply at high ϕ while the $\Delta\eta$ plot reveals an increase in response in the trough between struck quark and remnant peaks. In the medium x range, there is a slight suppression of activity in the low ϕ part of the P_t balance plot but an increase is visible at $\phi > 150^o$. The $\Delta\eta$ plot in this x range shows the opposite tendency to the low x distribution in that activity between the QPM struck quark direction and the remnant region has been decreased causing a double-peak structure to become evident.

5.14 Comparison to Monte Carlo Models

The effect of using corrected ZEUS data in a comparison with Monte Carlo models means that it is possible to study the models at the detector-independent four-vector level rather than at the detector-dependent level of the previous calorimeter cell analysis.

The models which the previous cell level study has rejected as unsuitable to describe the uncorrected data do not fare any better when compared to corrected data. Still, although in general agreement with the corrected data improves (mostly as a result of the larger error in the data points), it is not a big enough improvement to reverse any of the conclusions drawn earlier. A record of how each model fares against the corrected data in the low x region is presented in table 5.4. A few of the models which exhibit reasonable agreement are compared to corrected data in figures 5.29 and 5.30.

Those models which performed well against uncorrected data continue to do so against corrected data but as expected, they also retain their weaknesses :

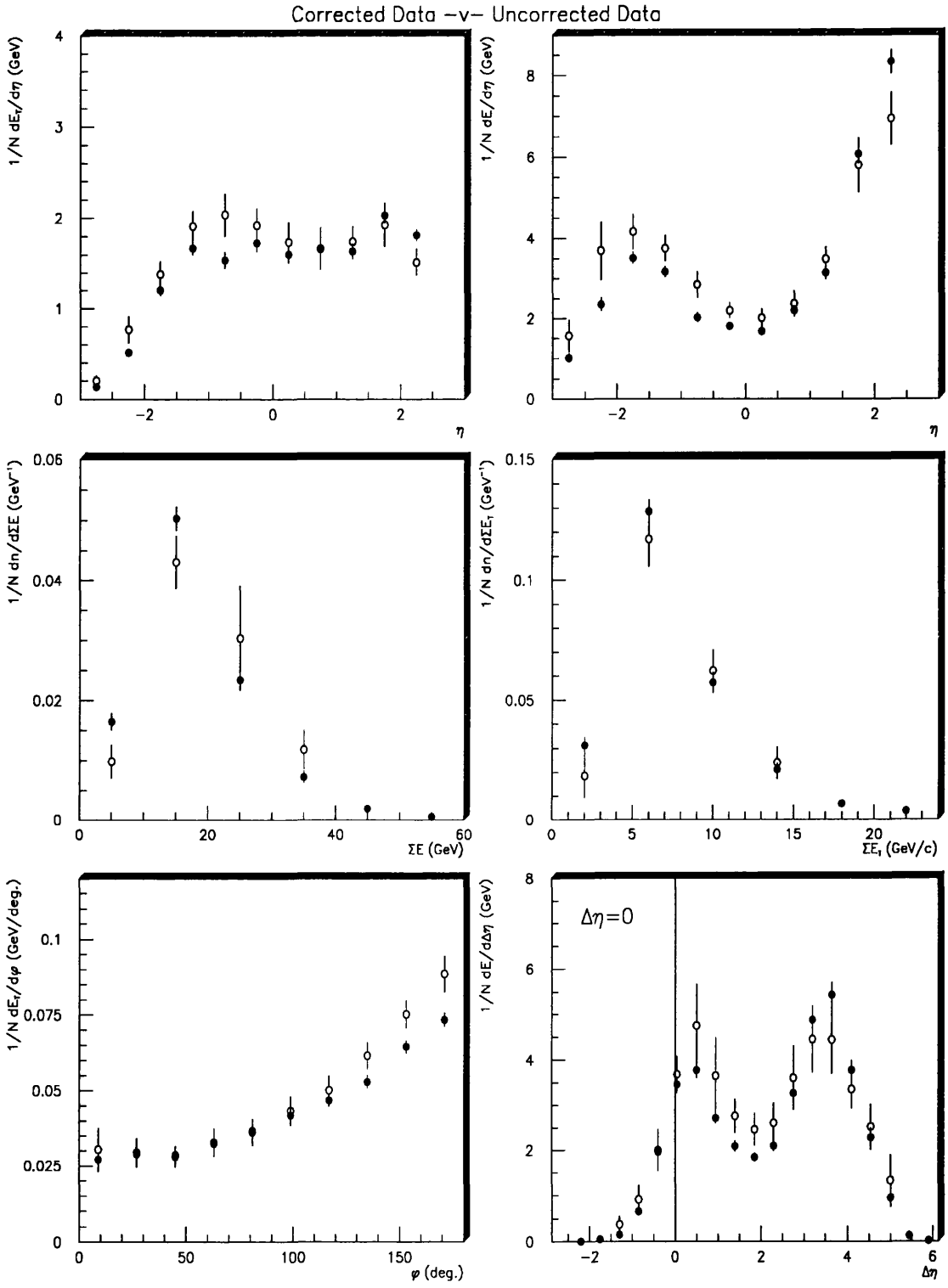

Figure 5.27: *Corrected data (open circles) compared to uncorrected data (solid circles) in the region* $x < 10^{-3}$.

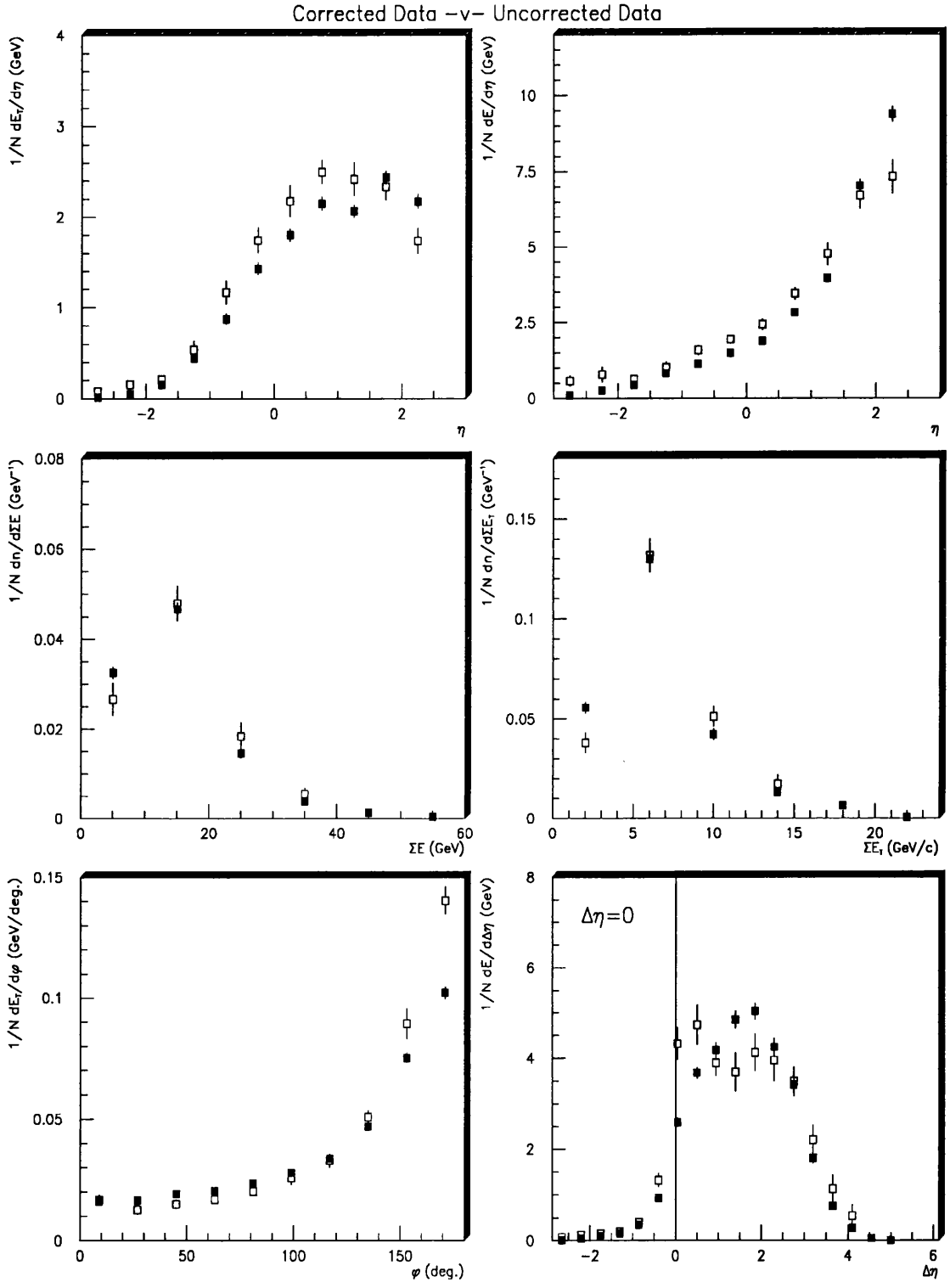

Figure 5.28: *Corrected data (open circles) compared to uncorrected data (solid circles) in the region* $10^{-3} < x < 10^{-2}$.

- ME+PS fails to reproduce the transverse energy weighted polar angle distributions and disagrees considerably when compared to the $\Delta\eta$ distribution of the data especially in the remnant region.

- CDM by itself has a similar problem to ME+PS in the transverse energy weighted polar angle plots, somewhat alleviated by the addition of a BGF treatment. Both gluon emission plots show a general overestimation of the data response for both models.

- HERWIG continues to have problems in the very forward region. In addition, it does not accurately reproduce either the total transverse energy or full energy responses shown by the data.

5.15 Summary and Conclusions

Calculation of correction factors has been performed using three independent Monte Carlo models and the results applied to the ZEUS data to reduce the influence of acceptance and smearing effects.

Repeating the Monte Carlo model comparisons, this time using four-vector data and comparing it to the corrected ZEUS data reinforces the conclusions drawn from the previous chapter. The Lund parton shower models with Q^2, W^2 or $Q^2(1-x)\ \max(1, \ln\frac{1}{x})$ and the matrix element approaches, when taken by themselves, cannot accurately reproduce the form of the data. The colour dipole approach, particularly with the inclusion of BGF processes, matrix elements matched to parton showers and the HERWIG model predict the corrected data response with a reasonable degree of accuracy although it is noted that care should be taken when adopting the HERWIG model with suppression of the soft underlying event.

This thesis has shown that of the broad range of available DIS Monte Carlo simulations, only those which incorporate $O(\alpha_s)$ gluon emission processes suitably restricted in the phase space governing colour coherence effects can accurately

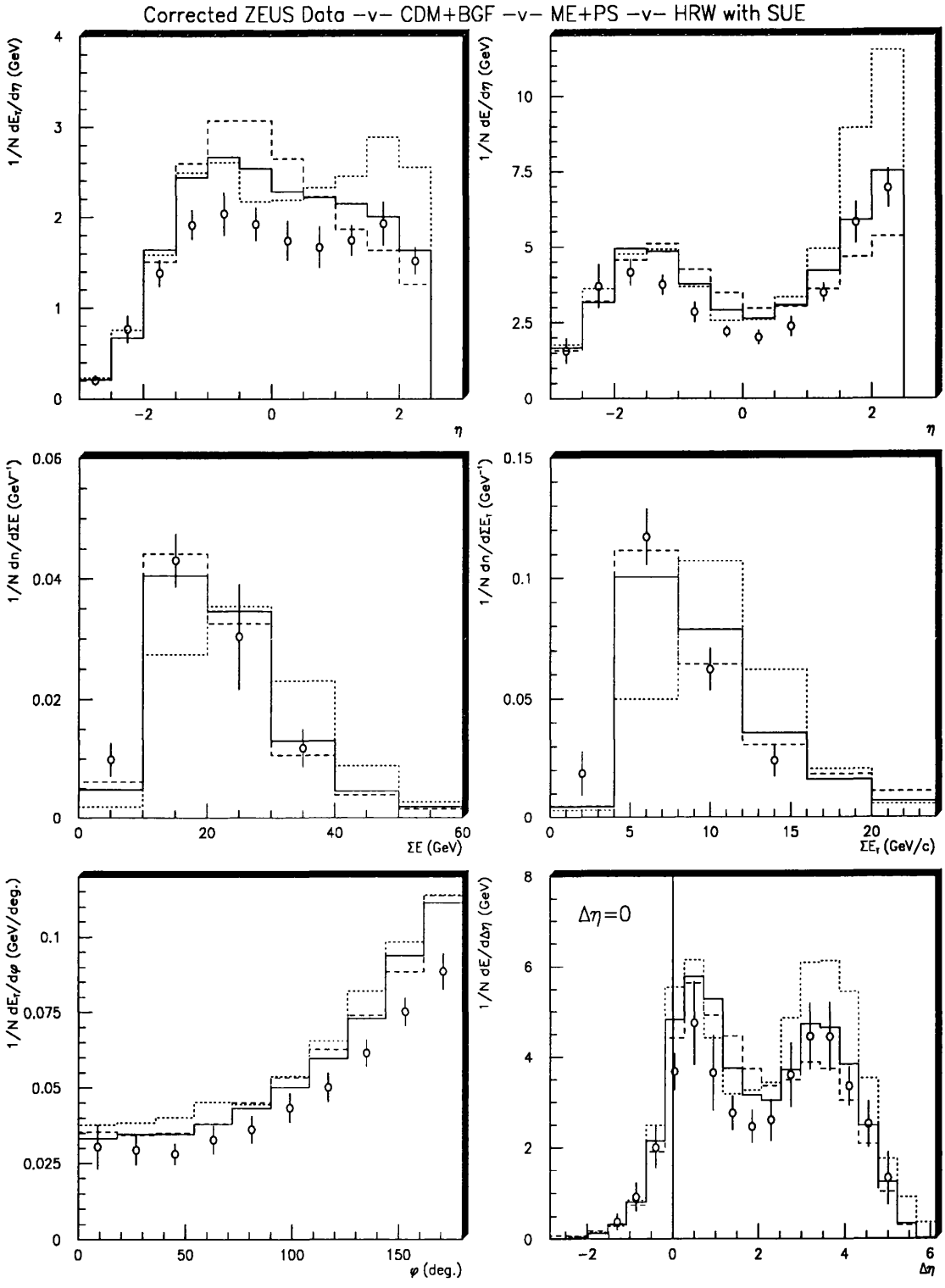

Figure 5.29: *The corrected data against CDM+BGF (solid line), ME+PS (dashed) and HERWIG with SUE (dotted) in the region* $x < 10^{-3}$.

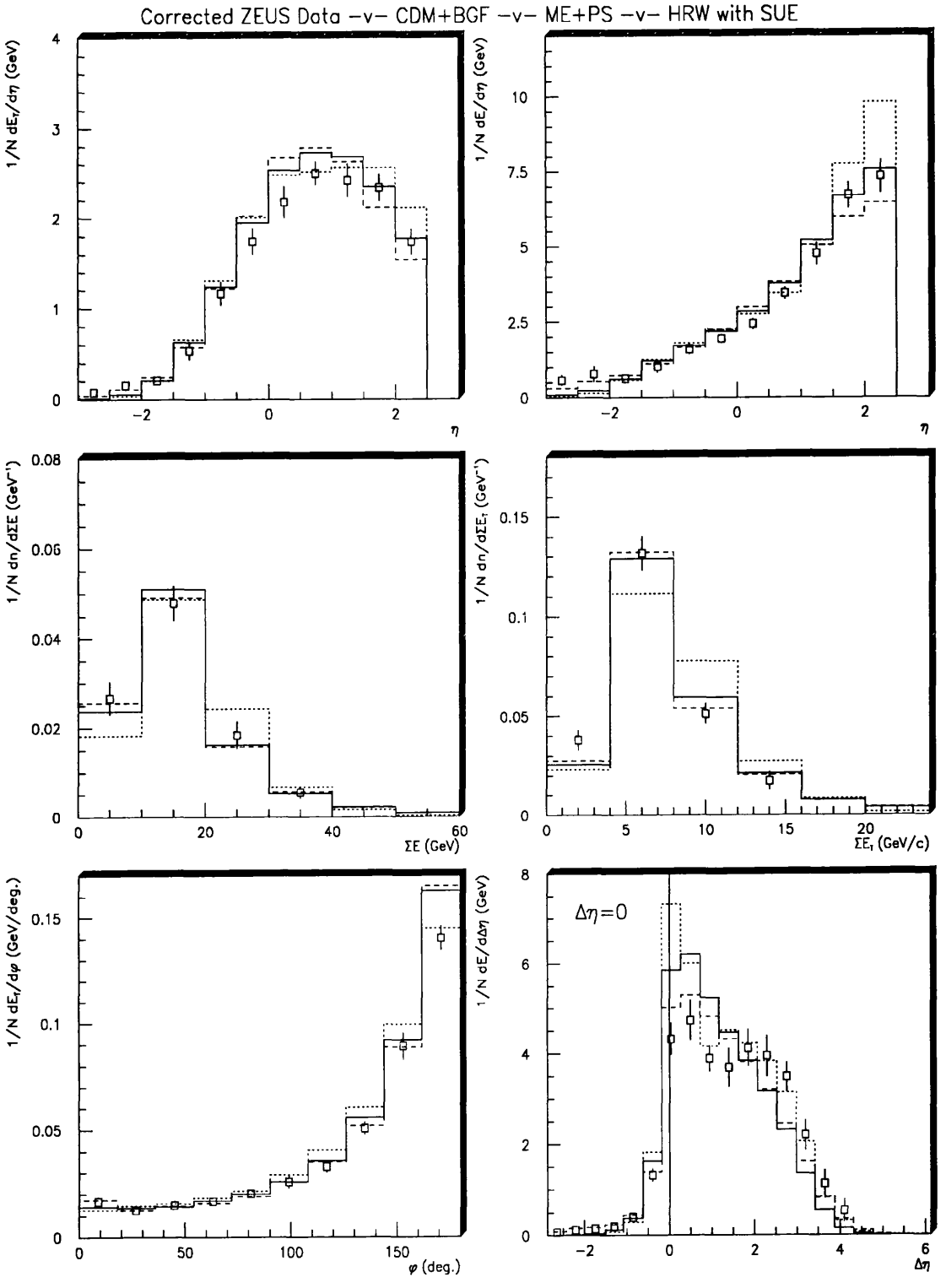

Figure 5.30: *The corrected data against CDM+BGF (solid line), ME+PS (dashed) and HERWIG with SUE (dotted) in the region* $10^{-3} < x < 10^{-2}$.

Plot # $\Longrightarrow$ MC Model $\Downarrow$	1	2	3	4	5	6
$10^{-4} < x < 10^{-3}$ data sample						
ME	10.9	11.9	3.8	19.8	17.2	16.2
ME+PS	5.4	6.2	0.9	0.4	0.5	1.9
PS(Q^2)	19.8	21.4	5.5	22.6	26.6	21.3
PS(W^2)	57.2	40.2	2.4	3.7	79.4	9.5
PS($Q^2(1-x)$)	10.1	10.9	6.4	10.4	8.1	6.3
CDM	10.4	10.5	1.1	2.6	8.0	3.6
CDM+BGF	3.9	4.2	0.7	1.8	4.7	1.3
HRW+SUE	7.6	8.8	5.0	13.2	8.4	3.0
HRW+NO SUE	4.5	5.3	3.0	14.2	5.2	1.7
$10^{-3} < x < 10^{-2}$ data sample						
ME	5.8	6.1	2.7	2.7	21.9	7.0
ME+PS	3.1	3.4	2.3	0.5	2.8	2.3
PS(Q^2)	13.7	13.1	7.9	7.1	37.5	11.0
PS(W^2)	20.1	9.6	2.0	3.1	35.4	4.8
PS($Q^2(1-x)$)	5.1	4.7	2.8	2.5	6.6	8.0
CDM	3.8	3.9	0.4	3.1	1.8	2.3
CDM+BGF	2.0	2.2	0.3	1.5	2.0	5.4
HRW+SUE	2.6	3.9	1.5	6.0	2.2	5.5
HRW+NO SUE	2.1	2.4	1.1	7.0	2.6	7.7

Table 5.4: *A summary of the analysed data sets and their approximate agreement with corrected ZEUS data.*

The numbers refer to the distributions as follows : 1. E_t weighted η 2. E weighted η 3. $\sum E_i$ 4. $\sum E_{t_i}$ 5. E_t weighted $\Delta\phi$ 6. E weighted $\Delta\eta$

reproduce ZEUS data. These conclusions are not changed when corrected data is examined. Another study should follow and attempt to "tune" these models to give closer agreement with the more precise data from 1993 physics runs.

References

[1] E. Rutherford, *Phil. Mag* **21** (1911) 669.

[2] For reviews see *Adventures in Experimental Physics*, (World Sci. Education, Princeton, N.J.), ed. B. Maglich (1976). In particular, consult :
S.C.C. Ting **5** 115; G. Goldhaber **5** 131; B. Richter **5** 143.

[3] S.W. Herb et al., Phys. Rev. Lett. **39** (1977) 252.
W.R. Innes et al., ibid. **39** (1977) 1240.

[4] L. Galtieri, *Top Searches at Fermilab*, talk given at the European Physical Society meeting, Marseille, July 1993.

[5] TASSO Collaboration, R. Brandelik et al., Phys. Lett. B **86** (1979) 243. For an overview, see S.L. Wu, Phys. Rep., **107** (1984) 59.

[6] F. Eisele and G. Wolf, *Physikalische Blätter*, (October 1992) 786.

[7] M.R. Adams et al., *A Spectrometer for Muon Scattering at the Tevatron*, Nucl. Inst. Meth. **A291** (1990) 533.

[8] P. Waloschek, *Praxis der Naturwissenschaften Physik*, **7/38**, 15th October 1989, 11-19.

[9] B. Wiik, *Transparencies pertaining to Zeus Note* **91-134** *covering Plenary Sessions during ZEUS Meeting at DESY*, 9th-13th December 1991, 14.

[10] W. Schultz, *Kinematics of ep Scattering at HERA* from transparencies of a DESY Seminar on HERA Physics, 1st February 1990.

[11] U. Amaldi, *Study of an ep facility for Europe*, DESY **79/48** (1979) 391-4.

[12] S. Bentvelsen, J. Engeln, P. Kooijman, *Reconstruction of* (x, Q^2) *and extraction of structure functions in neutral current scattering at HERA*, Proc. of the Workshop on Physics at HERA **1** (April 1992) 26.

[13] J.D. Bjorken, Phys. Rev. **179** (1969) 1547; ibid. **163** (1967) 1767.

[14] J.I. Friedman and H.W. Kendall, *Deep Inelastic Electron Scattering*, Annual Review of Nuclear and Particle Science, **22** (1972) 227.

[15] C.G. Callan and D. Gross, *High-Energy Electroproduction and the Constitution of the Electric Current*, Phys. Rev. Lett **22** (1969) 156.

[16] ZEUS Collaboration, M. Derrick et al., *Observation of Hard Scattering in Photoproduction at HERA*, Phys. Lett. B **306** (1993) 158.

[17] B. Webber, *Monte Carlo Simulation of Hard Hadronic Processes*, Ann. Rev. Nucl. Part. Sci., **36** (1986) 253-86.

[18] A.T. Doyle, *QCD Generators at HERA*, Journ. Phys. G. **17** 10 (1991) 1596.

[19] G. Altarelli and G. Parisi, *Asymptotic Freedom in Parton Language*, Nucl. Phys. B **126** (1977) 298-318.

[20] G. Altarelli, R.K. Ellis and G. Martinelli, Nucl. Phys. B **143** (1978) 521, Erratum Nucl. Phys. B **146** (1978) 544.
G. Altarelli, R.K. Ellis and G. Martinelli, ibid. **157** (1979) 461.
A. Mendez, ibid. **145** (1978) 199.
A. Mendez, Phys. Lett. B **83** (1980) 221.
R.D. Peccei, R. Rückl, Nucl. Phys. B **162** (1980) 125.
Ch. Rumpf, G. Kramer, J. Willrodt, Z. Phys. C **7** (1981) 337.
J.G. Körner, E. Mirkes and G.A.Schuler, Int. J. Mod. Phys. A **4** (1989) 1781.

[21] T. Sjöstrand, *A Model for Initial State Parton Showers*, Phys. Lett. B **157** (1985) 321.

M. Bengtsson, T. Sjöstrand and M. van Zijl, *Initial State Radiation Effects on W and Jet Production*, Z. Phys. C. **32** (1986) 67-83.

M. Bengtsson, G. Ingelman and T. Sjöstrand, *QCD Effects on the Event Structure in Leptoproduction*, Nucl. Phys. B **301** (1988) 554.

M. Bengtsson and T. Sjöstrand, *Coherent Parton Showers versus Matrix Elements - Implications of PETRA/PEP Data*, Phys. Lett. B **185** (1987) 435-440.

M. Bengtsson and T. Sjöstrand, *Parton Showers in Leptoproduction Events*, Z. Phys. C **37** (1988) 465-476.

M. Bengtsson, *Improved Parton Showers in ep Interactions*, Phys. Lett. B. **214** (1988) 645-650.

[22] G. Altarelli and G. Martinelli, *Transverse Momentum of Jets in Electroproduction from Quantum Chromodynamics*, Phys. Lett. B. **76** (1978) 89.

[23] G. Ingelman, *LEPTO version 6.1 - The Lund Monte Carlo for Deep Inelastic Lepton-Nucleon Scattering*, Proc. of the Workshop on Physics at HERA **3** (April 1992) 1366.

[24] G. Gustafson and U. Pettersson, *Dipole Formulation of QCD Cascades*, Nucl. Phys. B **306** (1988) 746.

[25] L. Lönnblad, *Ariadne 4.01 program and manual*, DESY Preprint **92-046**, February 1992, to be published in Comp. Phys. Comm.

[26] See, for example, F. Halzen and A. Martin, *Quarks and Leptons*, P. 239 or I.J.R Aitchison and A.J.G. Hey, *Gauge Theories in Particle Physics*, 2nd edition, P. 314.

[27] G. Gustafson, Phys. Lett. B, *Dual Description of a Confined Colour Field*, **175** (1986) 453;

G. Gustafson et al., *Coherence Effects in Deep Inelastic Scattering*, Z. Phys. C **43** (1989) 625-632.

[28] G. Marchesini, B.R. Webber, G. Abbiendi, I.G. Knowles, M.H. Seymour and L. Stanco, *HERWIG - a Monte Carlo event generator for simulating Hadron Emission Reactions With Interfering Gluons*, DESY **91-048**, May 1991.

[29] G. Marchesini and B.R. Webber, *Monte Carlo Simulation of General Hard Processes with Coherent QCD Radiation*, Nucl. Phys. B **310** (1988) 461.

[30] J.C. Collins, *Spin Correlations in Monte Carlo Event Generators*, Nucl. Phys. B **304** (1988) 794.
I.G. Knowles, *Spin Correlations in Parton-Parton Scattering*, ibid. **310** (1988) 571.

[31] B.R. Webber, *A QCD Model for Jet Fragmentation including Soft Gluon Interference*, Nucl. Phys. B **238** (1984) 492.

[32] D. Amati and G. Veneziano, *Preconfinement as a Property of Perturbative QCD*, Phys. Lett. B **83** (1979) 87.

[33] Ya.I. Azimov, Yu.L. Dokshitzer, V.A. Khoze and S.I. Troyan, *The String Effect and QCD Coherence*, Phys. Lett B **165** (1985) 147.

[34] B. Andersson et al., *Parton Fragmentation and String Dynamics*, Phys. Rep. **97** (1983) 31-145.

[35] T. Sjöstrand, Computer Physics Commun. **39** (1986) 347;
T. Sjöstrand and M. Bengtsson, Computer Physics Commun. **43** (1987) 367.

[36] M. Böhm and H. Spiesberger, Nucl. Phys. B. **294** (1987) 1081.
M. Böhm and H. Spiesberger, ibid. **304** (1987) 749.
H. Spiesberger, ibid. **394** (1991) 109.
H. Spiesberger, Proc. of the Workshop on Physics at HERA, **2** (April 1992) 798.

[37] A. Kwiatkowski, H. Spiesberger, H.-J. Möhring, *Heracles 4.1 - An event generator for ep interactions at HERA*, Proc. of the Workshop on Physics at HERA, **3** (April 1992) 1294.

[38] N. Magnussen et al., *Generators for Deep Inelastic Scattering*, Proc. of the Workshop on Physics at HERA, **3** (April 1992) 1167.

[39] C.B. Brooks et al., Nucl. Inst. Meth. A283 (1989) 477.
N. Harnew et al., ibid., A279 (1989) 290.

[40] H. Brückman, B. Anders and U. Behrens, *Hadron Sampling Calorimetry : A Puzzle of Physics*, Nucl. Inst. Meth **A263** (1988) 136.

[41] The ZEUS Calorimeter Group, *Construction and Beam test of the ZEUS Forward and Rear Calorimeter*, DESY Preprint **91-026**, April 1991.

[42] The Zeus-BAC Group, *Intercalibration of the ZEUS High Resolution and Backing Calorimeters*, DESY Preprint **91-081**, July 1991

[43] H. Bethe and W. Heitler, Proc. Roy. Soc., **A 146** (1934) 815.

[44] I. Park, *ZEUS DAQ and Early Results*, Talk given at SCC Laboratory, 10th June 1992.

[45] U. Behrens, L. Hagge and W.O. Vogel, *The Eventbuilder of the ZEUS Experiment*, DESY Preprint **93-008**, February 1993.

[46] S.M. Fisher and P. Palazzi, *The ADAMO Data System*, Programmer's Manual - Version 3.2, June 1992.

[47] G. Hartner, ZEUS Note 88-049 (1988).

[48] R. Brun et al., *GEANT 3.15*, CERN Program Library, CERN **DD/EE/84-1**, 1987.

[49] A. Dake, *GAZE Installation and User Guide*, ZEUS-Note **92-06**, 17th January 1992.

[50] P. de Jong, Ph. D. Thesis, NIKHEF (1993).

[51] V.L. Ginzburg and I.M. Frank, Sov. Phys. JETP **16** (1946) 15.

[52] X. Artru, G.B. Yodh and G. Monessier, Phys. Rev. D, **12** (1975) 1289.

[53] G.M. Garibyan, Sov. Phys. JETP **10** (1960) 372.

[54] B. Dolgoshein, *Transition Radiation Detectors and Particle Identification*, Nucl. Inst. Meth. **A252** (1986) 137-144.

[55] W.W.M. Allison and D.H. Saxon, *Classical Electrodynamics of Particle Detectors*, Textbook in preparation.

[56] ZEUS Collaboration, *Minutes of the ZEUS Meeting 15-19 February*, 1993.

[57] ZEUS Collaboration, M. Derrick et al., *Hadronic energy distributions in deep-inelastic electron-proton scattering*, Z. Phys. C **59** (1993) 231-242.

[58] J. Feltesse, *Measurement of Inclusive Differential Cross Sections*, Proc. of the HERA Workshop **1** (1987) 35.

[59] ZEUS Collaboration, M. Derrick et al., *Measurement of the proton structure function $F_2(x, Q^2)$ in ep scattering at HERA*, DESY Preprint **93-110** (August 1993).

[60] H1 Collaboration, T. Ahmed et al., *Measurement of the Proton Structure Function $F_2(x, Q^2)$ in the Low x Region at HERA*, DESY Preprint **93-117** (August 1993).

[61] A.D. Martin, R.G. Roberts and W.J. Stirling, Durham/RAL preprint DTP **92-16** and RAL **92-021**.

[62] J. Morfin and W.K. Tung, Z. Phys. C **52** (1991) 13.

[63] Edited by G. Altarelli, R. Kleiss and C. Verzegnassi, *QCD Generators*, Z Physics at LEP 1 **3** CERN 89-08 (1989) 143.

[64] Private communication, N. Pavel and T. Haas, to be published in an internal ZEUS note.

Acknowledgements

I'd like to thank a whole bunch of people for helping make the last three years so enjoyable. I owe a debt of gratitude to David Saxon who brought me to Glasgow in the first place and provided encouragement and guidance whenever it was needed. Colin Raine and Bob O'Neill showed me the business of *real* particle physics during many hours spent in the depths of the crane hall assembling and testing the TRDs. My gratitude goes to Hugh Morrison, Louis Campbell and Nick Todd who got me into physics in the first place. The Department of Education in Northern Ireland generously funded this work and I am grateful for their support. The staff there were always unfailingly helpful, polite and professional and a pleasure to deal with. I'd also like to say thanks to Peter Nichols of SERC who made possible my LTA at DESY. I owe Derek Morrow of RAL a large number of beers for helping out when we hit gas leak problems at DESY and thanks go to John Dainton for encouragement and advice when I was up to my ears in non-functioning TRDs. Paul de Jong provided the information on the calorimeter and DST selection cuts for which I am also grateful.

Nick Brook and Tony Doyle taught me everything I know in this business and I cannot thank them enough for their patience over the years. They have put up with me sharing an office with them for two years and in return, I have managed to drive both of them out. Despite Nick's pleading request not be to mentioned in this thesis at all (such a modest man!), I have included him as a thank you for the many thought-provoking, nay, profound conversations we have had and because his bribe wasn't big enough.

Valerie Jamieson and Allan Wilson, partners in crime at Glasgow, have

contributed hugely with their sparkling conversation and witty repartee. Valerie will make Gareth a wonderful gameshow hostess. Allan drinks beer. I will miss them both.

There are many people back in Glasgow to whom I owe my thanks, amongst them Catherine McIntyre, Ken Smith, David Martin, Alan Flavell and Andy Halley, who's now at MPI and CERN. John Matheson provided many an "Ook" and just the odd amusing anecdote when we were working anti-social hours in front of anti-social machines. The Ogri Motorcycle Club[1] and the Scottish Motorcycle Marshals Association provided an escape when needed. The soundtrack for this tome is available from your local record store. Just pick up anything in the Blues section...

To Alison, who understands me, reads me like a book, knows me inside and out and still goes out with me, I hope I can be for you even a fraction of what you are for me. My e-mail will never be the same again for a start. Finally, my parents Ruth and Bob, and my bro' Peter are everything a family could be when it comes to encouragement and support. Having them there made this task infinitely easier and I dedicate this thesis to them.

[1]Don't tell my mother I'm a biker! She thinks I play the piano in a brothel.